CONTENTS

APPLICATION OF HPM TO FIND ANALYTICAL SOLUTION OF COETTE FLOW WITH VARIABLE VISCOSITY

Alireza AZIMI*, Mohammadreza AZIMI, Amirhossein JAVANFAR*****

*Department of Chemical Engineering, College of Chemical Engineering, Islamic Azad University, Mahshahr Branch, Mahshahr, Farhangsara Street, Iran
**Faculty of New Sciences and Technologies, Department of Aerospace, University of Tehran, Tehran, North Kargar, Amirabad, Iran
***Faculty of Mechanical Engineering, Babol University of Technology, Shariati Street, Babol, Iran

meysam.azimi@gmail.com, m_r_azimi1991@yahoo.com, javanfar@ut.ac.ir

Abstract: In this paper, the couette flow of fluid with variable viscosity is studied analytically by using Homotopy Pertubation Method (HPM). At first the basic idea of Homotopy Pertubation Method (HPM) is presented. The mathematical formulation and application of HPM to nonlinear problem are presented in section three. In order to check the validity of solution the analytical results are compared with exact ones for various numerical cases. The good agreement between exact method and Homotopy Pertubation Method has been assures us about the solution accuracy.

Key words: Analytical Solution, HPM, Coette Flow, Viscosity

1. INTRODUCTION

Modelling of natural phenomena such as coquette flow and other fluid problems mostly leads to solving nonlinear equations. Except a limited number of these problems, most of them do not have analytical solution. So, the study on the various methods used for solving the nonlinear differential equations is a significant topic for the analysis of engineering problems. In recent years many powerful methods have been presented to construct solutions of Nonlinear Differential Equations such as Variational Iteration Method (VIM) (He, 1999), Homotopy Analysis Method (HAM) (Abasbandy, 2006), Homotopy Perturbation Method (Ghotbi et al., 2011; Jalal et al., 2011; Moghimi et al., 2011; Rashidi et al., 2012; Sharma and Methi, 2010) and Adomian Decomposition Method (Alan and Alkhaled, 2006; Ghosh, 2007; Lesnic, 2005; Pamuk, 2005).

The purpose of this present work is to present approximate analytical solution to a couette flow problem (Aziz and Na, 1984) with variable viscosity by Homotopy perturbation method. In order to investigate the validity and accuracy of results, the obtained results are compared with the exact solution.

2. BASIC IDEA OF HPM

The homotopy perturbation method (HPM) was first proposed by He. The HPM does not depend upon a small parameter in the equation. By the homotopy technique in topology, a homotopy is constructed with an imbedding parameter $p \in [0,1]$, which is considered as a "small parameter".

The HPM was successfully applied to the nonlinear oscillators with discontinuities (He, 2004b) bifurcation of nonlinear problems (He, 2004a), nonlinear wave equations (He, 2005). In (He, 2004a) comparison of HPM and homotopy analysis method was made, revealing that the former is more powerful than the later.

To illustrate the basic ideas of this method, we consider the following nonlinear differential equation (He, 2004a):

$$A(u) - g(r) = 0, \ r \in \Omega \tag{1}$$

with boundary conditions:

$$B(u, \partial u/\partial n) = 0, \ r \in \Gamma \tag{2}$$

where: $A, B, g(r)$ and Γ are a general differential operator, a boundary operator, a known analytical function, and the boundary of domain Ω.

Generally speaking the operator Acan be divided into a linear part L and a nonlinear part $N(u)$. Equation (1), therefore, can be rewritten as follows:

$$L(u) + N(u) - g(r) = 0 \tag{3}$$

By the homotopy technique, we construct a homotopy $f(r,p)$: $\Omega \times [0,1] \to R$ which satisfies:

$$H(f,p) = (1-p)[L(f) - L(u_0)] + p[A(f) - g(r)] = 0, \ p \in [0,1], r \in \Omega \tag{4}$$

or

$$H(f,p) = L(f) - L(u_0) + pL(u_0) + p[N(f) - g(r)] = 0 \tag{5}$$

where $p \in [0,1]$ is an imbedding parameter, u_0 is an initial approximation of Equation (1), which satisfies the boundary conditions. Obviously, from Equations (4) and (5) we have:

$$H(v,0) = L(v) - L(u_0) = 0 \tag{6}$$

$$H(v,1) = A(u) - f(r) = 0 \tag{7}$$

DOI 10.1515/ama-2015-0001

the changing process of p from zero to unity is just that of $v(r,p)$from $u_0(r)$to $u(r)$. In topology, this is called deformation, and $L(v)-L(u_0)$and$A(u)-f(r)$ are called homotopy.

According to the HPM, we can first use the imbedding parameter p as a "small parameter", and assumed that the solution of Equations (4) and (5) can be written as a power series in p:

$$f = f_0 + pf_1 + p^2 f_2 + p^3 f_3 + \cdots \tag{8}$$

Setting $p = 1$ results in the approximate solution of Equation (3):

$$f = \lim_{p\to 1} f = f_0 + f_1 + f_2 + \cdots \tag{9}$$

The coupling of the perturbation method and the homotopy method is called the homotopy perturbation method (HPM), which has eliminated limitations of the traditional perturbation methods. In the other hand, this technique can take full advantage of the traditional perturbation techniques.

The series (8, 9) are convergent for most cases, however, the convergent rate depends upon the nonlinear operator $N(v)$. The following opinions are suggested by He (He, 2004a):

1. The second derivative of $N(v)$ with respect to v must be small, because the parameter $p$may be relatively large, i.e. $p \to 1$.
2. The norm of $L^{-1}(\partial N/\partial v)$ must be smaller than one, in order that the series converges.

3. SOLUTION PROCEDURE

Consider the steady flow of an incompressible Newtonian fluid between two infinite, parallel plates separated by a distance a as shown in Fig. 1. Each plate is maintained at temperature T_0. The lower plate is stationary while the upper plate moves with a uniform velocity V. The thermal conductivity of the fluid is assumed to be constant, but the viscosity is allowed to vary. The pertinent momentum and energy equations are(Aziz and Na, 1984):

$$\frac{d}{dy}\left(\mu\frac{du}{dy}\right) = 0 \tag{10}$$

$$\frac{d^2T}{dy^2} + \frac{\mu}{k}\left(\frac{du}{dy}\right)^2 = 0 \tag{11}$$

$$y = 0, \quad u = 0, \quad T = T_0 \tag{12}$$

$$y = a, \quad u = V, \quad T = T_0 \tag{13}$$

where: u – axial velocity, T – temperature, μ – viscosity and k – thermal conductivity.

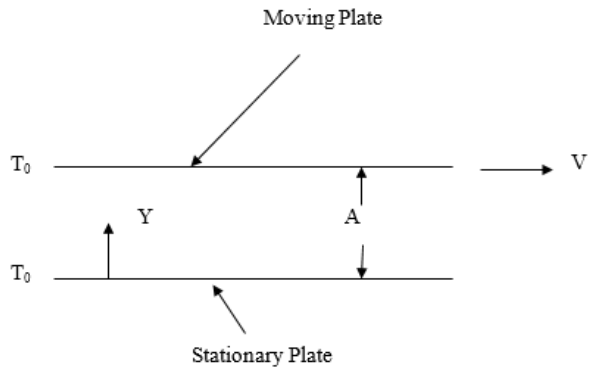

Fig. 1. Plane Coette Flow

Let the viscosity vary exponentially with temperature according to:

$$\mu = \mu_0 e^{-\alpha(T-T_0)} \tag{14}$$

where: μ_0 is the viscosity at T_0 and a is a constant.

Introduce Equation (14) and the following dimensionless quantities into Equations (10)-(13):

$$\theta = \frac{T-T_0}{T_0}, \quad Y = \frac{y}{a}, \quad U = \frac{u}{V}$$
$$\beta = \alpha T_0, \quad \varepsilon = \frac{\mu_0 V^2}{kT_0} \tag{15}$$

to give:

$$\begin{cases} \frac{d}{dY}\left(e^{-\beta\theta}\frac{dU}{dY}\right) = 0 \\ \frac{d^2\theta}{dx} + \varepsilon e^{-\beta\theta}\left(\frac{dU}{dY}\right)^2 = 0, \end{cases} \tag{16}$$

$$\begin{cases} Y = 0, \quad U = 0, \quad \theta = 0 \\ Y = 1, \quad U = 1, \quad \theta = 0 \end{cases} \tag{17}$$

In this case, the parameter $\mu_0 V^2/kT_0$ is identified as the perturbation quantity ε. In viscous flow terminology, it is called the Brinkman number, and represents the ratio of viscous heating due to conduction. Thus, if the effect of viscous heating is weak, one may treat ε as small and carry out a perturbation analysis. As shown by Turian and Bird (1963), such an analysis is applicable to flow in a cone-and-plate viscometer.

In order to solve this system with homotopy perturbation method (HPM), we consider:

$$\begin{aligned} U(Y) &= v_1(Y), \quad \theta(Y) = v_2(Y) \\ v_{1,0}(Y) &= U_0(Y), \quad v_{2,0}(Y) = \theta_0(Y) \end{aligned} \tag{18}$$

$$\begin{aligned} v_1(Y) &= v_{1,0}(Y) + pv_{1,1}(Y) + p^2 v_{1,2}(Y) \\ v_2(Y) &= v_{2,0}(Y) + pv_{2,1}(Y) + p^2 v_{2,2}(Y) \end{aligned} \tag{19}$$

the term $e^{-\beta\, i\, \theta(Y)}$ must be expanded as follows:

$$e^{-\beta\theta(Y)} = 1 - \beta\theta(Y) + \frac{1}{2}\beta^2\theta^2(Y) \tag{20}$$

The substitution of Equation (20) into Equation (16) yields:

$$\begin{cases} \left(1 - \beta\theta + \frac{1}{2}\beta^2\theta^2\right)\frac{d^2U}{dY^2} + \beta\left(\beta\theta - \frac{1}{2}\beta^2\theta^2 - 1\right)\frac{dU}{dY}\frac{d\theta}{dY} = 0 \\ \frac{d^2\theta}{dY^2} + \varepsilon\left(1 - \beta\theta + \frac{1}{2}\beta^2\theta^2\right)\left(\frac{dU}{dY}\right)^2 = 0 \end{cases} \tag{21}$$

According to the HPM, we must firstly determine the initial approximations for $v_1(Y)$and$v_2(Y)$. So we construct following system for linear parts:

$$\begin{cases} \frac{d^2U_0}{dY^2} = 0 \\ \frac{d^2\theta_0}{dY^2} = 0 \end{cases} \tag{22}$$

with following conditions:

$$\begin{cases} Y = 0, \quad U_0(Y) = 0, \quad \theta_0(Y) = 0 \\ Y = 1, \quad U_0(Y) = 1, \quad \theta_0(Y) = 0 \end{cases} \tag{23}$$

The solution of Equation (45) is as follows:

$$\begin{cases} U_0(Y) = v_{1,0}(Y) = Y \\ \theta_0(Y) = v_{2,0}(Y) = 0 \end{cases} \tag{24}$$

A homotopy for the system of Equation (21) can be constructed as follows:

$$\begin{cases}(1-p)\left(\frac{d^2v_1}{dY^2}-\frac{d^2v_{1,0}}{dY^2}\right)+\\ p\left(\left(1-\beta v_2+\frac{1}{2}\beta^2v_2^2\right)\frac{d^2v_1}{dY^2}\right)+\beta\left(\beta v_2-\frac{1}{2}\beta^2v_2^2-1\right)\frac{dv_1}{dY}\frac{dv_2}{dY}=0\\ (1-p)\left(\frac{d^2v_2}{dY^2}-\frac{d^2v_{2,0}}{dY^2}\right)+\\ p\left(\frac{d^2v_2}{dY^2}+\left(1-\beta v_2+\frac{1}{2}\beta^2v_2^2\right)\varepsilon\left(\frac{dv_1}{dY}\right)\right)=0\end{cases} \quad (25)$$

The substitution of Equation (24) into Equation (25) yields:

$$\begin{cases}(1-p)\left(\frac{d^2v_1}{dY^2}\right)+\\ p\left(\left(1-\beta v_2+\frac{1}{2}\beta^2v_2^2\right)\frac{d^2v_1}{dY^2}+\beta\left(\beta v_2-\frac{1}{2}\beta^2v_2^2-1\right)\frac{dv_1}{dY}\frac{dv_2}{dY}\right)=0\\ (1-p)\left(\frac{d^2v_2}{dY^2}\right)+\\ p\left(\frac{d^2v_2}{dY^2}+\left(1-\beta v_2+\frac{1}{2}\beta^2v_2^2\right)\varepsilon\left(\frac{dv_1}{dY}\right)\right)=0\end{cases} \quad (26)$$

The substitution of Equation (19) into Equation (26) and collect the result up to p^2 yields:

$$\begin{cases}\left(-\beta\frac{dv_{2,1}}{dY}+\frac{d^2v_{1,2}}{dY^2}\right)p^2+\frac{d^2v_{1,1}}{dY^2}p=0\\ \left(\frac{d^2v_{2,2}}{dY^2}-\varepsilon\beta v_{2,1}\right)p^2+\left(\frac{d^2v_{2,1}}{dY^2}+\varepsilon\right)p=0\end{cases} \quad (27)$$

then we must equalize the coefficients of p and p^2 in Equation (27) with zero:

$$\begin{cases}\frac{d^2v_{1,1}}{dY^2}=0\\ \frac{d^2v_{2,1}}{dY^2}+\varepsilon=0\\ -\beta\frac{dv_{2,1}}{dY}+\frac{d^2v_{1,2}}{dY^2}=0\\ \frac{d^2v_{2,2}}{dY^2}-\varepsilon\beta v_{2,1}=0\end{cases} \quad (28)$$

with following conditions:

$$v_{i,j}(0)=v_{i,j}(1)=0,\quad i,j=1,2 \quad (29)$$

therefore the results are as follows:

$$\begin{cases}v_{1,1}(Y)=0\\ v_{1,2}(Y)=-\frac{1}{6}\beta\varepsilon Y^3+\frac{1}{4}\beta\varepsilon Y^2-\frac{1}{12}\beta\varepsilon Y\\ v_{2,1}(Y)=-\frac{1}{2}\varepsilon Y^2+\frac{1}{2}\varepsilon Y\\ v_{2,2}(Y)=-\frac{1}{24}\beta\varepsilon^2Y^4+\frac{1}{12}\beta\varepsilon^2Y^3-\frac{1}{24}\beta\varepsilon^2Y\end{cases} \quad (30)$$

According to the HPM, we can conclude:

$$\begin{aligned}U(Y)&=\lim_{p\to 1}\left(v_{1,0}(Y)+pv_{1,1}(Y)+p^2v_{1,2}(Y)\right)\\ \theta(Y)&=\lim_{p\to 1}\left(v_{2,0}(Y)+pv_{2,1}(Y)+p^2v_{2,2}(Y)\right)\end{aligned} \quad (31)$$

The substitution of Equations (24) and (30) into Equation (31) yields:

$$U(Y)=Y-\frac{1}{2}\beta\varepsilon\left(\frac{1}{3}Y^3-\frac{1}{2}Y^2\right)-\frac{1}{12}\beta\varepsilon Y \quad (32)$$

$$\theta(Y)=-\frac{1}{2}\varepsilon Y^2+\frac{1}{2}\varepsilon Y-\frac{1}{2}\beta\varepsilon^2\left(\frac{1}{12}Y^4-\frac{1}{6}Y^3\right)-\frac{1}{24}\varepsilon^2\beta Y \quad (33)$$

We avoid listing the other components. The forgoing homotopy perturbation solution may be compared with the exact solution (Turian and Bird, 1963) which is given by:

$$e^{\beta\theta}=\left(1+\frac{\varepsilon\beta}{8}\right)\mathrm{sech}^2\left[(2Y-1)\sinh^{-1}\left(\frac{\varepsilon\beta}{8}\right)^{1/2}\right] \quad (34)$$

$$U=\frac{1}{2}\left\{\left(1+\frac{8}{\varepsilon\beta}\right)^{1/2}\tanh\left[(2Y-1)\sinh^{-1}\left(\frac{\varepsilon\beta}{8}\right)^{1/2}\right]+1\right\} \quad (35)$$

4. RESULTS AND DISCUSSIONS

In previous section, analytical investigation of plane couette flow with variable viscosity is presented. In this section, we will present the obtained results. As it can be illustrated in Fig. 2 the comparison is made between HPM solution and exact ones for $\beta=1$ and a range of values of ε. In Fig. 3.the deviations with the exact solutions have been plotted for $\beta=1$ and a range of values of ε.

According to Fig. 3 effect of the Brinkman number on temperature profile is considerable. The increasing of Brinkman number cause higher peak in temperature profile.

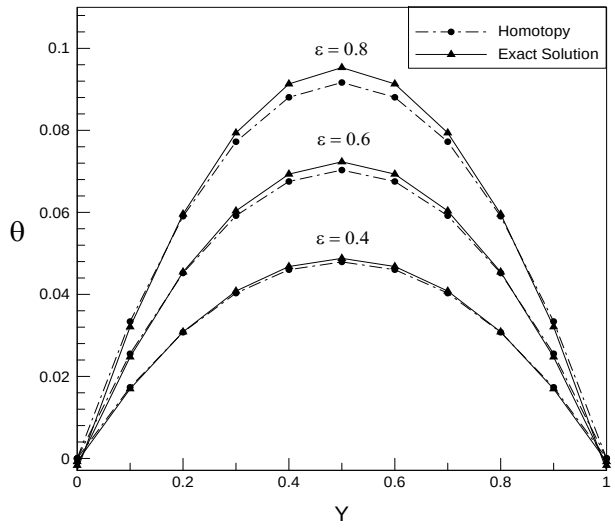

Fig. 2. Temperature distribution in plane couette flow, $\beta=1$

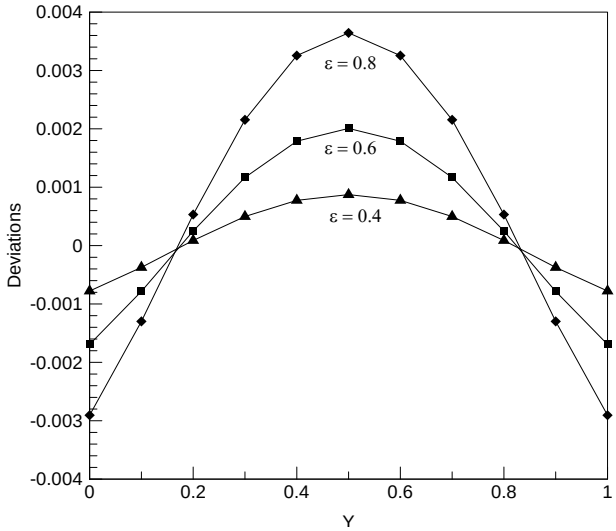

Fig. 3. Deviations of the HPM (2-term expansion) results with exact solution,with fixed value $\beta=1$

DOI 10.1515/ama-2015-0001

Tab. 1 shows the effect of increasing the number of HPM terms on obtained temperature values for a range of values of ε when $Y = 0.5, \beta = 1$.

Tab. 1. Comparison between Exact solutions and Analytical results for various term expansions of HPM and different value of ε in case $Y = 0.5, \beta = 1$

ε	HPM (3-term expansion)	HPM (4-term expansion)	Exact
0.05	0.0061514	0.0062104	0.0062305
0.5	0.0604317	0.0606101	0.0606246
1	0.1176017	0.117721	0.1177831
1.5	0.1717675	0.1718101	0.1718502
2	0.2210188	0.2230992	0.2231435

Good agreement between analytical approximate solution and numerical method assure us about validity and accuracy of solution.

5. CONCLUSIONS

In this paper, the homotopy perturbation method (HPM) has been successfully applied to finding the solutions of plane couette flow with variable viscosity. The HPM does not require small parameters in the equations, so that the limitations of the traditional perturbation methods can be eliminated and the calculations in HPM is simple and straightforward. In HPM, the approximations obtained are valid, not only for small parameters, but also for larger ones. The results show that the HPM is a powerful mathematical tool for solving differential system, it is also a promising method to solve other nonlinear ordinary and partial differential systems. The solutions obtained are shown graphically and compared with the exact solution.

REFERENCES

1. **Abbasbandy S.** (2006), The application of homotopy analysis method to nonlinear equations arising in heat transfer, *Physics Letter*, A 360, 109–113.
2. **Allan F., Al-Khaled K.** (2006), An approximation of the analytic solution of the shock wave equation, *Journal of Computational and Applied Mathematics*, 192, 301–309.
3. **Aziz A., Na T. Y.** (1984), *Perturbation methods in heat transfer*, Hemisphere Publishing Corp.
4. **Ghosh S., Roy A., Roy D.** (2007), An adaptation of Adomian decomposition for numeric-analytic integration of strongly nonlinear and chaotic oscillators, *Computer Methods in Applied Mechanics and Engineering*, 196, 1133–1153.
5. **Ghotbi A. R., Barari A. Ganji D. D.** (2011), Solving ratio-dependent predator-prey system with constant effort harvesting using homotopy perturbation method, *Mathematical Problems in Engineering*, ID 945420.
6. **He J. H.** (1999), Variational iteration method: A kind of nonlinear analytical technique: Some examples, *International Journal of Non-Linear Mechanics*, 344, 699–708.
7. **He J. H.** (2004a), Comparison of homotopy perturbation method and homotopy analysis method, *Appl. Math Comput.*, 156, 527–39.
8. **He J. H.** (2004b), The homotopy perturbation method for nonlinear oscillators with discontinuities, *Appl. Math Comput.*, 151, 287–92.
9. **He J. H.** (2005), Homotopy perturbation method forbifurcation of nonlinear problems, *Int. J. Nonlinear Sci. Numer. Simul.*, 6(2), 207-215.
10. **Jalaal M., Nejad M. G., Jalili P.** (2011), Homotopy perturbation method for motion of a spherical solid particle in plane couette fluid flow, *Computers and Mathematics with Applications*, 61, 2267–2270.
11. **Lesnic D.** (2005), Decomposition methods for non-linear, non-characteristic Cauchy heat problems, *Communications in Nonlinear Science and Numerical Simulation*, 10, 581–596.
12. **Moghimi S. M., Ganji D. D., Bararnia H., Hosseini M., Jalaal M.** (2011), Homotopy perturbation method for nonlinear MHD Jeffery-Hamel problem, *Computers and Mathematics with Applications*, 61, 2213–2216.
13. **Pamuk S.** (2005), Solution of the porous media equation by Adomian's decomposition method, *Physics Letters*, A 344, 184–188.
14. **Rashidi R. R., Beg O.A., Rastegari M.T., Mehmood A.** (2012), Homotopy study of buoyancy-induced flow of non-newtonian fluids over a non-isothermal surface in a porous medium, *International Journal of Applied Mathematics and Mechanics*, 8, 34-52.
15. **Sharma P. R., Methi G.** (2010), Solution of coupled nonlinear partial differential equations using homotopy perturbation method, *International Journal of Applied Mathematics and Mechanics*, 6, 33-49.
16. **Turian R. M., Bird R. B.** (1963), Viscous heating in the cone-and-plate viscometer II, *Chem. Eng. Sci.*, 18, 689-96.

THE INFLUENCE OF CLEARANCES IN A DRIVE SYSTEM ON DYNAMICS AND KINEMATICS OF A TELESCOPIC CRANE

Arkadiusz TRĄBKA*

*Faculty of Mechanical Engineering and Computer Science, Department of Engineering Fundamentals, University of Bielsko-Biala, ul. Willowa 2, 43-309 Bielsko-Biała, Poland

atrabka@ath.bielsko.pl

Abstract: The paper presents the results of numerical analyses that were carried out in order to evaluate how a change in a size of a clearance in a slewing motion drive system of a telescopic crane influences the movement of a load and the dynamic loads of a structure. A computational model was developed based on a real structure of an experimental crane by using the ADAMS software. The analyses showed that a circumferential clearance at the output of a reduction gear, which is less than 1º, does not adversely affect the precision of the load movement. An excessive clearance leads to losing fluidity of a body slewing motion and to changes in the trajectory of the load.

Key words: Clearances, Drive System, Experimental Telescopic Crane, Multibody Dynamic Systems

1. INTRODUCTION

Kinematic and dynamic analysis of systems with a complex kinematic structure is mostly done based on numerical models. Many phenomena that occur in real structures are usually neglected in these models. Clearance in joints of structural components is one of the most frequently neglected phenomenon. Omission of clearances simplifies analysis, but at the same time makes that the results may significantly differ from reality. Confirmation of this can be found in various works. Authors of this works have studied the influence of the clearance in kinematic pairs on the kinematic and/or dynamic properties of various kinds of mechanisms, e.g. a slider-crank (Flores, 2010; Flores and Ambrosio, 2004; Flores et al., 2010; Olivier and Jesus, 2002), a yoke (Olivier and Jesus, 2002), a four-bar linkage (Bai and Zhao, 2012; Tian et al., 2009; Ting et al., 2000), a parallel manipulator (Parenti-Castelli and Venanzi, 2005; Ting et al., 2000), an open manipulator with two link arms (Zhao and Bai, 2011), an open manipulator with four link arms (Harlecki, 1999) and an industrial robot manipulator (Erkaya, 2012; Pan et al., 1998).

Taking into account clearances in drive systems is very important for the proper mapping of real systems. Clearances in these systems may occur in various types of joints, for example parallel key, splined and coupling. However, due to design a sumptions the clearances are mainly present at the interface of gear wheels in toothed gears (Oberg et al., 2004). The influence of the clearance between the teeth of wheels on the dynamic properties of different types of gears (planetary, single-stage and two-stage) has been shown in Kuusisto (1999); Siyu et al., (2011); Sun and Hu (2003); Walha et al. (2009).

Cranes with telescopic booms are examples of real systems with complex kinematic structure (Trąbka, 2014a). Their computational models usually are considered as devoid of clearances, whereas they occur both in joints of structural components and in drive systems. Clearances in computational models of cranes were encountered only in two works among the reviewed papers. In Harlecki (1998) the clearance was taken into account in joints between supporting beams and guides of a crane frame, while in Trombski et al. (1995) the clearance between members of a telescopic boom was considered. None of the reviewed papers contains a model taking into account clearances in a crane drive system.

The drive systems are one of the most important systems of telescopic cranes that determine the precision of a load motion. Their structure should provide the possibility to execute the load motion in accordance with the planned trajectory. This trajectory can significantly change due to presence of excessive clearances between components of the drive system.

This paper presents the results of numerical analyses of a computational model of an experimental telescopic crane that were carried out in order to evaluate how a change in a size of a circumferential clearance, at the output of a reduction gear of a slewing motion drive, influences the movement of a load and the dynamic loads of a structure.

2. COMPUTATIONAL MODEL OF A CRANE

The crane model was developed in two stages. First, the Inventor program was used to build a geometric model. This model was developed based on the real structure of an experimental crane (Fig. 1a). In the second stage, the computational model was developed (Fig. 1b). It was made by using the ADAMS multibody system analysis software.

The computational model included the majority of the experimental crane structural components. Only some fasteners and wires of little significance for the dynamics of the structure were omitted. A reduction gear of the body slew drive was made as the system of three elements, i.e. a gear joint, a coupling with adjustable size of a circumferential clearance and a torsion spring with a vibration damper (see detail in Fig. 1b). Joints between structural components were selected to map accurately the real object

DOI 10.1515/ama-2015-0002

movement possibilities. Particular attention was paid to prevent the occurrence of so-called redundant constraints. The dimensions, masses and mass moments of inertia of the model parts were determined based on measurements of the real structure and the geometrical models of these parts, which had been developed by using the Inventor software (Tab. 1).

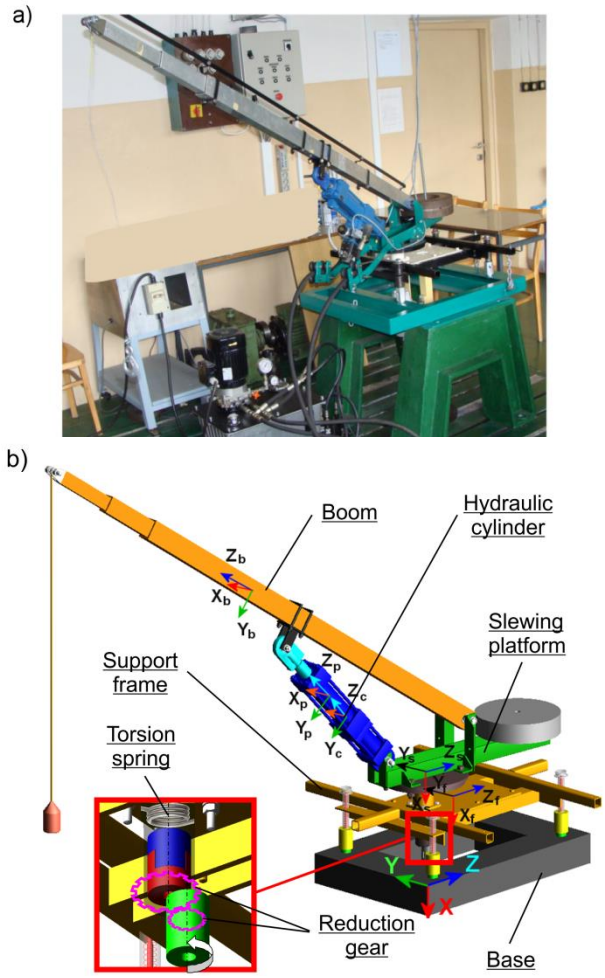

Fig. 1. a) Experimental telescopic crane (Trąbka, 2014b), b) Computational model

The possibility of deformations was taken into account in the model only in supports and in the body slew drive. A support system with the supports having bilateral constraints was used (Trąbka, 2014b). The stiffnesses of vertical springs that were used to model the supports (Fig. 2) were determined experimentally. The same stiffness was adopted for all springs. This stiffness was determined for a spring that was randomly selected from the set of springs based on a series of 10 measurements of the dependence of deformation on the load. For each dependence of deformation on the load, an average stiffness k_N was calculated based on equation (1) and then a substitute stiffness $k_x = 17.25 \times 10^3 \mathrm{N/m}$ was determined by using equation (2). Apart from axial stiffnesses also the stiffnesses of pairs of springs, perpendicular to their axes, were taken into account. Lateral stiffnesses of the pairs of springs ($k_y = k_z = 114 \times 10^3 \mathrm{N/m}$) were determined numerically. Both the computational model and the calculations were made using the Ansys v11 software and following a method described in Kłosiński and Trąbka (2010).

$$k_N = \frac{1}{m} \cdot \sum_{i=1}^{i=m} \frac{\Delta P_i}{\Delta l_i} \tag{1}$$

$$k_x = \frac{1}{s} \cdot \frac{1}{n} \cdot \sum_{N=1}^{N=n} k_N \tag{2}$$

where: N – measurement number, m – number of changes in a spring load, s = 2 – number of springs that are connected in parallel to each other in a crane support model, n – number of measurements, ΔP_i – i-th change in the load carried by a spring, Δl_i – i-th change in a spring length.

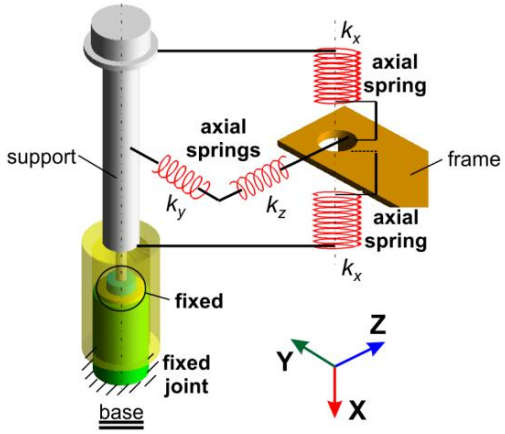

Fig. 2. Support model (Trąbka, 2014b)

Tab. 1. Masses and mass moments of inertia of the model parts

Name of a given part	Mass [kg]	Mass moments of inertia with respect to the centres of masses of the model parts [kg·m²]		
		J_{sx}	J_{sy}	J_{sz}
Support frame	17.3	0.792	0.567	0.235
Slewing platform	20.2	0.688	0.706	0.128
Counterweight	17	0.175	0.094	0.094
Boom	4.5	0.937	0.936	0.0025
Piston rod	3.7	0.068	0.067	0.0008
Cylinder	11	0.21	0.21	0.01
Reductor	10.5	0.003	0.003	0.0002

Damping coefficients c_u in the supports (systems of springs) were calculated, by using equation (3), for the directions of the X, Y and Z-axes of a reference frame. These calculations were based on the changes in position of the support frame with respect to the base (Giergiel, 1986).

$$c_u = \frac{2 \cdot M \cdot \delta}{T} \tag{3}$$

where: M – mass connected with the system of supports (which depends on the location of the sensor of displacements and the direction of movement), δ – average value of the logarithmic damping decrement (based on equation (4)), T – average value of a period of the damped vibration (based on equation (5)).

$$\delta = \frac{1}{2} \cdot \left[\ln\left(\frac{1}{k} \cdot \sum_{i=1}^{i=k} \frac{A_i}{A_{i+1}} \right) + \ln\left(\frac{1}{l} \cdot \sum_{j=1}^{j=l} \frac{A_j}{A_{j+1}} \right) \right] \tag{4}$$

where: k – number of amplitudes in the upper part of the characteristics (included in the calculations), l – number of amplitudes in the bottom part of the characteristics (included in the calculations),

A_i, A_j – amplitudes for the upper and the lower part of the characteristics, A_{i+1}, A_{j+1} – subsequent amplitudes for the upper and the lower part of the characteristics.

$$T = \frac{1}{2} \cdot \left[\frac{1}{p} \cdot \sum_{i=1}^{i=p} T_i + \frac{1}{r} \cdot \sum_{j=1}^{j=r} T_j \right] \quad (5)$$

where: p – number of periods in the upper part of the characteristics (included in the calculations), r – number of periods in the bottom part of the characteristics (included in the calculations), T_i – partial periods in the upper part of the characteristics, T_j – partial periods in the bottom part of the characteristics.

For every direction of movement, 10 measurements were carried out and the average damping coefficients c_s were calculated based on these measurements. Finally, the following values were adopted for calculations: $c_{sx} = 0.28 \times 10^3 \mathrm{N} \cdot \mathrm{s/m}$, $c_{sy} = 0.47 \times 10^3 \mathrm{N} \cdot \mathrm{s/m}$, $c_{sz} = 0.59 \times 10^3 \mathrm{N} \cdot \mathrm{s/m}$.

The stiffness of the body slew drive ($k_{\alpha r} = 7.386 \times 10^3 \mathrm{N} \cdot \mathrm{m/rad}$) was determined based on a separate model (Fig. 3). This model was developed in the ADAMS program based on the structure of the Befared 7-AP-RM-2-V6 two-stage reduction gear (with a gear ratio $i = 20$), which was used to drive the experimental crane. Deformations of shafts, parallel key connections and gears were included in the above model using torsion springs. These springs were inserted between rigid solid elements. Torsional stiffnesses were calculated for the particular components based on the formulas shown in Table 4.1 in Marchelek (1991).

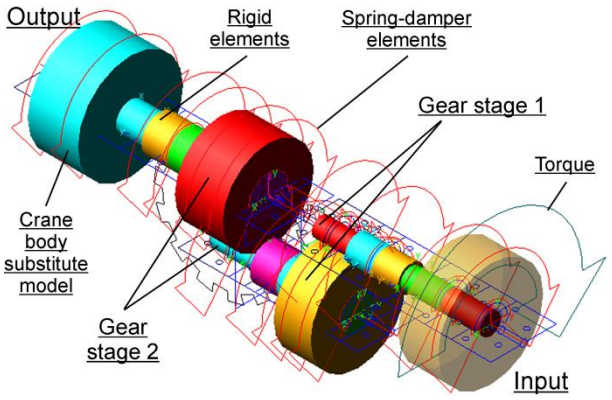

Fig. 3. Model of the body slew drive

The model shown in Fig. 3 was also used to determine a substitute damping coefficient of the slew drive ($c_{\alpha r} = 9.16 \mathrm{N} \cdot \mathrm{m} \cdot \mathrm{s/rad}$). Based on equation (6) the damping coefficients $c_{\alpha i}$ of the power transmission components were determined (Marchelek, 1991):

$$c_{\alpha i} = k_i \cdot T_i \quad (6)$$

where: k_i – stiffness coefficient of i-th component, T_i – time constant of i-th component (taken from Table 4.4 in Marchelek (1991)).

The calculated coefficients were assigned to the individual torsion springs and then the analysis of damped free vibrations of the substitution model of the body was performed (the substitution model parameters were obtained by the reduction of the body mass as well as its mass moments of inertia to the drive output).

The substitute damping coefficient of the slew drive was calculated from equation (7) (Żółtowski, 2002).

$$c_{\alpha r} = \frac{\delta}{\pi} \cdot \sqrt{J_z \cdot k_{\alpha r}} \quad (7)$$

where: δ – average value of the logarithmic damping decrement (based on equation (4)), J_z – mass moment of inertia of the body substitution model, calculated with respect to its axis of rotation, $k_{\alpha r}$ – stiffness of the slew drive of the body.

Spring-damper properties of the drive were introduced into the model as the parameters of the torsion spring. This spring was inserted between the coupling (modelling a clearance zone at the output of the reduction gear) and the axis of rotation of a slewing platform (see the torsion spring in Fig. 1b).

3. RESULTS AND DISCUSSION

This paper presents an evaluation of the influence of the clearance size, in the slewing motion drive system of the telescopic crane body, on the load trajectory, the speed of rotation of the body and the support loads.

The calculations were carried out for a crane radius of 1.43 m, a rope length of 1 m and a load mass of 1 kg. It was assumed that the initial position of the computational model corresponds to a crane being in a state of static equilibrium; the initial tension of springs, used to model the supports, was taken into account (their values were taken as consistent with registered during the tests of the experimental crane). The rotation of the body relative to a chassis by an angle of 90º was analysed. The kinematic input function (Fig. 4) and a constant step of integration (Δt = 0.001 s) were used.

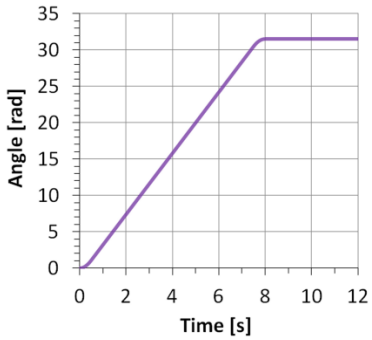

Fig. 4. Slewing motion input function

The model without circumferential clearance at the reduction gear output as well as with clearances of the values 0.5º, 1.0º, 1.5º, 2.0º, 2.5º, 3.0º, 3.5º, 4.0º, 4.5º and 5.0º was analysed. The clearance was introduced both on an active side (designation CA) as well as on a passive side (designation CB); wherein on the passive side its value was always 0.5° (Fig. 5).

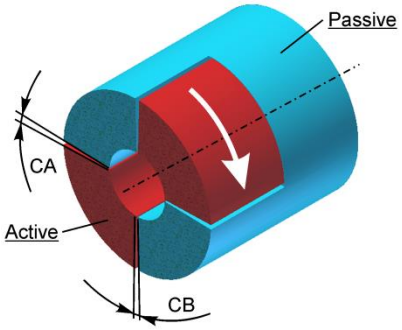

Fig. 5. Clearance model

DOI 10.1515/ama-2015-0002

The computational model was verified experimentally. This verification was conducted by comparing the calculated support loads with the loads that were recorded during the tests of the experimental crane with 3º clearance at the output of the reduction gear. The comparison result is shown in Fig. 6a. It was found that the model properly map the real object, and the visible differences between characteristics are due to the omission of the flexibilities of particular parts (especially the boom), the flexibilities of joints, the friction in joints, and most of all due to the omission of clearances at the supports.

The calculation results for the model without clearance and with clearances of 1.0º, 3.0º and 5.0º are presented in Figs. 6b-d. Fig. 6b presents the trajectory of the mass centre of the load while Fig. 6c shows the changes in the speed of rotation of the body relative to the chassis. The distribution of the support loads is shown in Fig. 6d.

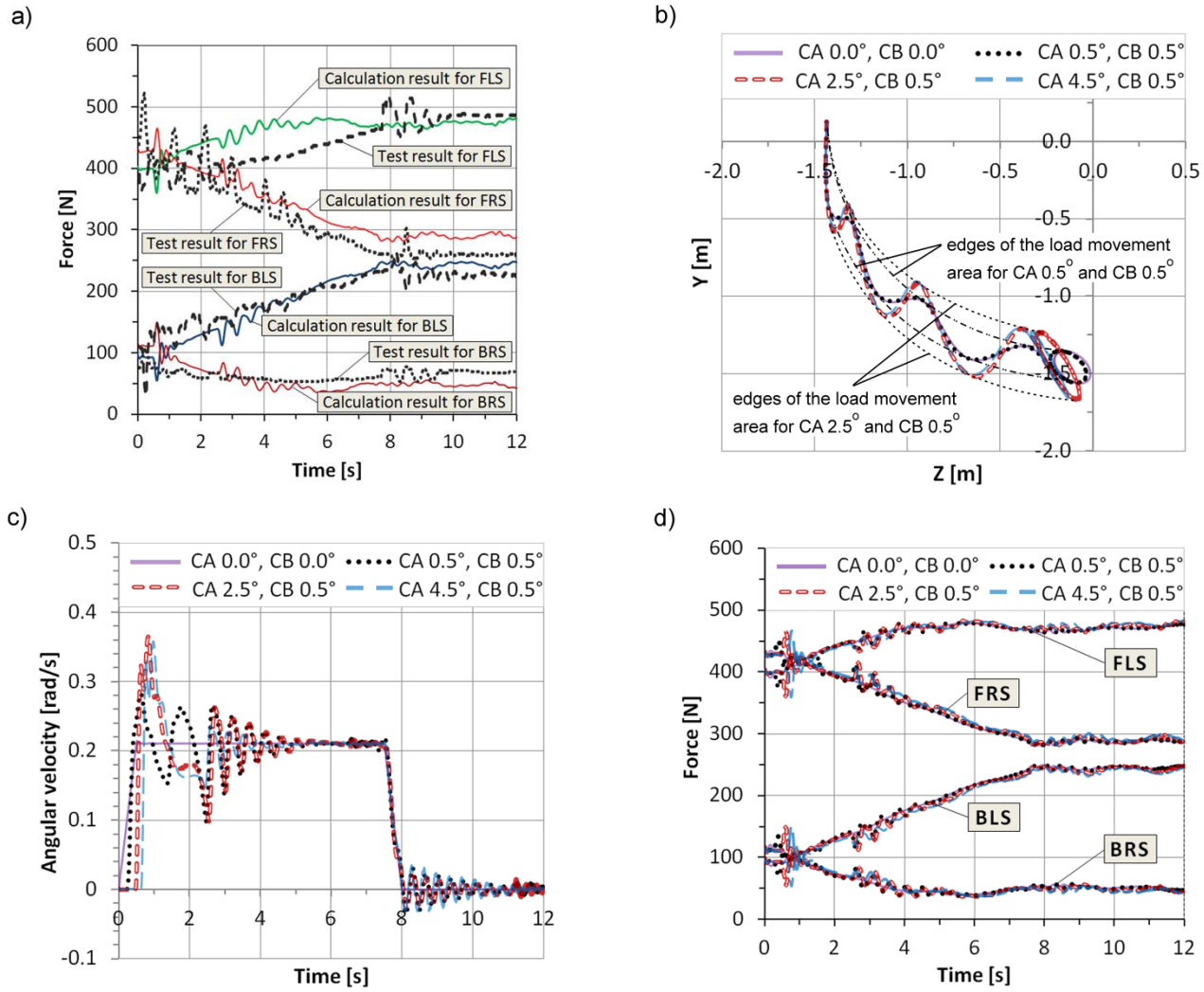

Fig. 6. Calculation results: a) comparison of the support loads - calculated with the one that were recorded during the tests (for 3º clearance), b) trajectory of the mass centre of the load, c) speed of rotation of the body relative to the chassis, d) distribution of the support loads (FLS – front left support, FRS – front right support, BLS – back left support, BRS – back right support)

Based on the calculation results (Figs. 6b-d) it was found that:

- The trajectory of the load is not subject to significant changes if the circumferential clearance at the output of the reduction gear does not exceed 1º. When the clearance increases in the range of 1º to 3º the load swings are increasing in the direction of radial and tangential components. As a result, the trajectory of the load is changing both during the rotation and after stopping of them. Further increase of the clearance (in the range of 3º to 5º) contributes to a slight reduction in the load swings.
- The load swings after stopping of the slewing motion, due to an excessive clearance at the output of the reduction gear, can be up to 73.7% higher than in the model without the clearance (for the clearance equal 4º).
- Even a small clearance at the output of the reduction gear causes that the speed of rotation of the body undergoes constant changes. The changes in the speed of rotation are closely related to the vibrations of the body whose amplitude and frequency depends on the size of the clearance, the stiffness and the damping in the drive system. The largest change of the speed in relation to the value obtained for the model without clearance was 73% when the clearance was 3º.
- The maximum changes in the load of supports occur during the start-up. They are greater the larger is the clearance, and at the same time, the higher value achieves acceleration when

the clearance is deleted. The largest change of the load in relation to the value obtained for the model without clearance was 53% when the clearance was 4º.

4. CONCLUSIONS

This paper presents the results of numerical analyses of a computational model of an experimental crane that were carried out in order to evaluate how a change in a size of a circumferential clearance, at the output of a reduction gear of a slewing motion drive, influences the movement of a load and the dynamic loads of a structure. Based on the numerical analyses, it has been found that:

- The circumferential clearance, which is less than 1º, does not adversely affect the precision of a load movement. The maximum excess of the support loads for 1º amount of the clearance does not exceed 14.7% of the value obtained for the model without the clearance.
- When the clearance increases in the range of 1º to 3º both the load swings and the vibration amplitudes of a body are increasing too. As a result, the area in which a load moves becomes wider (Fig. 6b). Pulsed changes in the load of supports increase, wherein the largest values of the dynamic excess with respect to the value determined for the model without clearance (ΔQ = 43.5% for the clearance equal 3º) are obtained during the start-up. They are greater the higher value achieves acceleration during the start-up.
- Increasing of the clearance in the range of 3º to 5º means a further (but much less than in the range of 1º to 3º) increase of the dynamic excess of the support loads. However, the load swings are slightly smaller, especially those that occur after stopping the slewing motion.

The above observations show that clearances should be controlled in drive systems of telescopic cranes, as even slight increasing of them above values established by the designers leads to a significant worsening of their kinematic and dynamic properties.

REFERENCES

1. **Bai Z.F., Zhao Y.** (2012), Dynamics modeling and quantitative analysis of multibody systems including revolute clearance joint, *Precision Engineering*, 36, 554– 567.
2. **Erkaya S.** (2012), Investigation of joint clearance effects on welding robot manipulators, *Robotics and Computer-Integrated Manufacturing*, 28, 449–457.
3. **Flores P.** (2010), A parametric study on the dynamic response of planar multibody systems with multiple clearance joint, *Nonlinear Dynamics*, 61, 633–653.
4. **Flores P., Ambrosio J.** (2004), Revolute joints with clearance in multibody systems, *Computers and Structures*, 82, 1359–1369.
5. **Flores P., Leine R., Glocker R.** (2010), Modeling and analysis of rigid multi-body systems with translational clearance joints based on the nonsmooth dynamics approach, *Multibody System Dynamics*, 23 (2), 165–190.
6. **Giergiel J.** (1986), *Damping of mechanical vibrations* (in Polish), Wyd. AGH, Kraków.
7. **Harlecki A.** (1998), Dynamic analysis of telescopic truck crane using the rigid finite element method, *Zeszyty Naukowe Politechniki Łódzkiej Filii w Bielsku-Białej, Budowa i Eksploatacja Maszyn*, 32 (51), 11-39.
8. **Harlecki A.** (1999), „Stick-Slip" motion of open manipulators with flexible drives and dry friction in joint, *Journal of Theoretical and Applied Mechanics*, 4 (37), 873-892.
9. **Kłosiński J., Trąbka A.** (2010), Frequency analysis of vibratory device model (in Polish). *Pneumatyka*, 1, 46-49.
10. **Kuusisto S.** (1999), Transient nonlinear dynamics of camshafts, *Proceedings of the IMAC 17th international modal analysis conference*, 1093-1099.
11. **Marchelek K.** (1991), *Machine tools dynamics* (in Polish), WNT, Warszawa.
12. **Oberg E., Jones F.D., Horton H.L., Ryffel H.H.** (2004), *27th Edition Machinery's Handbook*, Industrial Press, Inc., New York.
13. **Olivier B.B.A., Jesus R.** (2002), Modeling of joints with clearance in flexible multi-body system, *International Journal of Solids and Structures*, 39, 41–63.
14. **Pan M., Van Brussel H., Sas P.** (1998), Intelligent joint fault diagnosis of industrial robots, *Mechanical Systems and Signal Processing*, 12 (4), 571-588.
15. **Parenti-Castelli V., Venanzi S.** (2005), Clearance influence analysis on mechanisms, *Mechanism and Machine Theory*, 40, 1316–1329.
16. **Siyu C., Jinyuan T., Caiwang L., Qibo W.** (2011), Nonlinear dynamic characteristics of geared rotor bearing systems with dynamic backlash and friction, *Mechanism and Machine Theory*, 46, 466–478.
17. **Sun T., Hu H.Y.** (2003), Nonlinear dynamics of a planetary gear system with multiple clearances, *Mechanism and Machine Theory*, 38, 1371–1390.
18. **Tian Q., Zhang Y., Chen L., Flores P.** (2009), Dynamics of spatial flexible multibody systems with clearance and lubricated spherical joint, *Computers and Structures*, 87 (13-14), 913–929.
19. **Ting K.L., Zhu J., Watkins D.** (2000), The effects of joint clearance on position and orientation deviation of linkages and manipulators, *Mechanism and Machine Theory*, 35, 391-401.
20. **Trąbka A.** (2014a), Dynamics of telescopic cranes with flexible structural components, *International Journal of Mechanical Sciences*, 88, 162–174.
21. **Trąbka A.** (2014b), The impact of the support system's kinematic structure on selected kinematic and dynamic quantities of an experimental crane, Acta Mechanica et Automatica, vol.8, no.4, 189-193.
22. **Trombski M., Kłosiński J., Majewski L., Suwaj S.** (1995), Dynamic analysis of a crane model when the clearances in kinematic pairs of the crane jib are taken into account (in Polish), *Materiały VIII Konferencji „Problemy Rozwoju Maszyn Roboczych", Część I*, Zakopane, 191-198.
23. **Walha L., Fakhfakh T., Haddar M.** (2009), Nonlinear dynamics of a two-stage gear system with mesh stiffness fluctuation, bearing flexibility and backlash, *Mechanism and Machine Theory*, 44, 1058–1069.
24. **Zhao Y., Bai Z.F.** (2011), Dynamics analysis of space robot manipulator with joint clearance, *Acta Astronautica*, 68, 1147–1155.
25. **Żółtowski B.** (2002), *Research of machine dynamics* (in Polish), Wyd. MARKAR, Bydgoszcz.

THE DIESEL AND THE VEGETABLE OIL PROPERTIES ASSESSMENT IN TERMS OF PUMPING CAPABILITY AND COOPERATION WITH INTERNAL COMBUSTION ENGINE FUELLING SYSTEM

Dariusz SZPICA[*] ,Jarosław CZABAN[*], Piotr BANASZUK[**], Emil WERESA[*]

[*]Faculty of Mechanical Engineering, Department of Mechanical Engineering,
Bialystok University of Technology, ul. Wiejska 45C, 15-351 Bialystok, Poland
[**]Faculty of Civil and Environmental Engineering, Department of Environmental Protection and Management,
Bialystok University of Technology, ul. Wiejska 45E, 15-351 Bialystok, Poland

d.szpica@pb.edu.pl, j.czaban@pb.edu.pl, p.banaszuk@pb.edu.pl, e.weresa@pb.edu.pl

Abstract: In the paper, the results of preliminary diesel and vegetable oil research were shown, the subject of which were directly intended to be the fuel for powering compression ignition engines. In the times of climate protection and more strict standards concerning combustion gas emissions, the fuel production and transportation process became an important aspect. Decentralization of this process and enabling fuel obtaining directly from cultivation (oleaginous plants) let limit the global CO_2 emission. This is why the preliminary assessment of two fuel sorts properties was attempted, on one side, the basic one, which is the diesel, on the other side - vegetable oil. Prior to subjecting the compression ignition engine to the process of adaptation to vegetable fuelling, the properties of the fuel responsible for pumping should be assessed (mainly viscosity) and friction nodes cooperation (lubricity). The first of researched parameters is the base to elaborating the system of engine controlling algorithm or the range of changes in construction of powering system. The second one is the wear issue - object fitness and repairing overhauls.

Key words: Internal Combustion Engine, Alternative Fuels, Rheological Properties

1. INTRODUCTION

The realization of ambitious European Union plans for climate protection will be demanding the resetting the energy production system in Europe to nearly non-emission one, stable in terms of supply and not weakening the European economy competitiveness. Lowering the emission in transport section must reach the level of 60 % before 2050 comparing to 1990 and around 20 % before 2030 comparing to 2008. Last years, the emission of GHG (greenhouse gases) significantly decreases, due to the growing oil prices, bigger engines efficiency and slower society's mobility increase. Such tendency will probably maintain till 2020, but in following years, there will be a quick resetting of exisisting transport system required. The significant element of activities will be a research in new technology in driving systems and alternative fuels, including biofuels (A policy…, 2014).

It is known, that the bio-fuels production on the rural areas would not cover the global need and that is why they could not replace fossil fuels (HLPE, 2013). Applying them as components to the transport fuels is a transient solution, potentially loaded with undesirable side effects for environment. The bio-fuels application is advised in such mobility sections, where nowadays the realistic and promising alternative solutions cannot be obtained: including agricultural activity, forestry and flight transport (Opinion…, 2013).

The agro-fuels' research concerns two main issues: fuel production, especially the ways of lowering undesirable components containment and adaptation of the engines to qualitative new fuel usage, including improving fuel serving and combustion optimization, so that the maintaining the engine power and gas and dust pollution limiting were possible, according to valid standards (Commission Directive 2010/26/UE, Embeger et al., 2012).

Powering the compression ignition engine with FAME (Fatty Acid Methyl Esters) and raw oil from various seeds, which have lower energetic value than diesel oil, is connected to increase of time specific fuel consumption, at almost unchanged general efficiency value, but nitrous oxides (NOx) and solid particles emission is bigger (Cisek and Mruk, 2012; Dzieniszewski and Piekarski, 2006; Pasyniuk and Golimowski, 2011; Wasilewski, 2006; Tesfa, 2014; Durbin, 2000; Kaplan et al., 2006; Karavalakis et al., 2009; Nabi et al., 2006; Cranacki, 2007; Lin et al., 2009; Raheman and Phadatare, 2004; Xue et al., 2011; Amaranath et al., 2012).

The combustion course comparison implies, that rapeseed oil ester combustion is energetically comparable with diesel, in spite of lower heating value (35 - 37) MJ/kg in lieu of 42 MJ/kg, within constant combustion chamber volume and common-rail dual-phase injection (Bocheński et al., 2005). The problem is with large value of bio-fuel viscosity (Tab. 1).

Tab. 1. The viscosity values of the most popular vegetable oils used as diesel engine fuels

Autors	Fuel				
	rapeseed	soybean	sunflower	corn	diesel
dynamic viscosity, mPa·s					
(Wcisło,2008)	42(-10°C) 13(20°C)	36(-10°C) 13(20°C)			10.3(-10°C) 8.4(20°C)
kinematic viscosity, $mm^2 \cdot s^{-1}$					
(Bocheński, Bocheńska,2005)	4.72(40°C)				1.8(40°C)
(Łaska et al.,2013)	36.46(15°C)		41.08(15°C)	33.81(15°C)	

The 15 % rapeseed oil ester addition to diesel fuel causes insignificant, by 1.9 $mm^2 \cdot s^{-1}$ in 40 °C temperature fuel viscosity increase, while 30 % addition increases the viscosity by 2.8 $mm^2 \cdot s^{-1}$. Such viscosity increase insignificantly worsens the

fuel spray, but does not influence the wear properties in essential way, however 30 % of rapeseed oil esther increases filter blocking temperature from -34 °C to -17 °C (Bocheński and Bocheńska, 2005).

Tests conducted on agricultural tractors showed, that without big obstacles, the engine can wark on pure vegetable oil during period with temperatures over 0°C, in lower temperatures, either the engine heating or diesel oil addition is required (2ndWegOil, Money et al., 2001, Pasyniuk and Golimowski, 2011). As a fuel, besides the fresh vegetable oil, also the cooking oil (exploited) is used. The supplement of 20 and 50 % of the filtered cooking oil, is optimal, in order to exhaust gas emission (Lin et al., 2007). Powering the Fiat Doblo 1.9 DS with used cooking oil caused very low loss of the tractive force on wheels (3.35 %), and as well, the the lower power (2.03 %) relative to the vehicle powered with diesel fuel. In acceleration tests from 40 to 100 km/h and from 60 to 100 km/h the times lengthened consequently by 7.32 % and 8.78 %.

There were not any measureable friction wear effects stated in the case of the friction couple of injection pump, in the form of reduction of a piston diameter of pumping section, in spite of usage of very accurate measuring methods with accuracy of 0.0002 mm. During the research the systematic decrease of the tightness of the section was observed, due to the micro-cutting and fissuring with fuel pollution grains (Gil et al., 2010).

The problem can be occuring due to the microorganisms development in the fuelling systems, which can cause the row of processes influencing adversably on powering systems and the quality of the contained fuel. They include the filter clogging and fuel lines, injectors plugging, the corrosion of the tank or fuel lines, decomposition of hydrocarbons and refining additions, water and sulfur content increase in fuel, forming the sediments and solid particles suspension in fuel, and creating surface-active substances causing fuel emulsification (Lasocki and Karwowska, 2010). Thevegetable oil properties can be improved in the cold climate conditions via addition of ethanol, kerosene and commercial refiners (Bhale, 2009).

The research of the bio-fuel-powered engine emission gases points to the decrease of CO, HC and solid particles emission and inrease of NO_x emission (Ulusoy et all, 2004). Positive effects were also obtained in the case of pure rapeseed oil powering the VW Golf 1.6D engine (Dzieniszewski and Piekarski, 2006).

Modern diesel engines solutions, besides the Common-Rail (C-R) fuel system, are equipped with many applications related to exhaust gas emmission cleaning. Beyond oxidating catalytic converter, there can often solid particle filters or SCR (Selective Catalytic Reduction) catalytic converters be met. Additionally, the EGR (exhaust gas recirculation) can work in system. By connecting bio-diesel and EGR it was tried to lower the NO_x and PM emission of the commercial truck working on low load. The combination of bio-diesel and EGR replaces the volatile state O_2 from air with the oxygen in the fuel, what implies the 40 % decrease of PM and NO_x emmission comparing to using ultra-low diesel oil quantity with ultra-low sulfur content without recirculation. The PM decrease and proper NO_x / PM ratio increase has a positive impact on DPF DPF (diesel particulate filter) operation, due to the more beneficial oxidation stoichiometry. Another advantage of this system is the possibility of NO_x reduction optimization via increasing the EGR quantity, during work in required DPF beneficial operation boundaries (Muncrief et al., 2008).

It is indicated that the more beneficial for the climate protection and more energy effective is the usage of natural vegetable oil rather than FAME bio-diesel esters (Directive 2009/28/WE). Decentralized production and use of pure vegetable oil (PVO) as an independent fuel or bio-component can favor the rural areas development. In spite of that, most of the bio-fuel researche conducted in Europe and in Poland concerned the quality and utility parameters of FAME, what causes very one-sided and insufficient knowledge on the subject of organizational and technical possibilities of biofuel usage. Therefore, the urgent need of undertaking research of PVO fuelling and operating properties exists.

This paper is the first of the publication cycle related to the complex process, what is the production and using the vegetable oil in engine applications. As a beginning, the aim was stated to assess the viscosity and lubricity properties of the vegetable oil.

2. FUELS AND RESEARCH PROCEDURES

For the research, the refined rapeseed oil was used, compliant with PN-A-86908:2000 standard, and diesel oil, compliant with PN-EN 590:2006 standard, with fatty acid methyl esters containment not exceeding the 7 % of fuel volume.

The viscosity and lubricity of pure diesel oil and pure vegetable oil was researched, as well as their mixtures with different proportions.

The viscosity is the fluid feature, which gives the information about the internal friction size, and mainly depends on temperature and pressure. The viscosity measure is so called viscosity indicator.

Researched liquid, in the amount of 50 ml, fills the space between spindle 2 and the measuring vessel 1 (Fig. 1). The viscometer operates on a method of measuring the friction force, with which the researched oil acts on the spinning spindle immersed in it. Basing on that force value and spindle with oil contact area, the tangent stresses are assessed. To enable viscosity research in different temperatures, the system was supplemented with temperature stablility system 3 with the thermal regulator. The technical data of the viscometer was showed in Tab. 2.

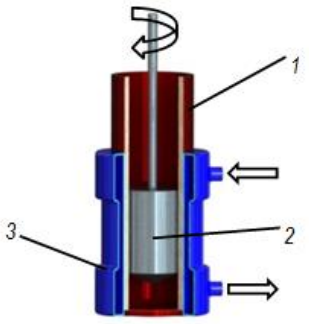

Fig. 1. The scheme showing the operation of viscometer DV-II+ Brookfield

Tab. 2. Technical data of the rotational viscometer DV-II+ Brookfield

Parameter	Value
- measurement range	(1 - 6 million) mPa·s
- spindle rotational speed	(0.01 - 200) rpm
- numbers of speeds	54
- temperature range	(0 - 99) °C
- measured values	viscosity, shear stress, torque

The lubircity is the property, which states the capability of boundary layer creation on the solid mass surface. The value of the lubricity is the boundary layer durability, i.e. durability of connection between the lubricant with base. It can be, for example, assessed basing on the work amount, which must be applied to break the layer, or, what was used in research on the four-ball apparatus, basing on the phenomena related to the lubricity, i.e. wear processes, scuffing tendency.

The researching elements in four-ball apparatus are four bearing balls 1 made in 0th accuracy class and selection group tolerance of 0.8 μm and Rockwell hardness of 60 HRC (Fig. 2). The ball fixing in lower clamp 2 filled with researched lubricant with temperature of 20±5 °C is realized by means of threaded shield with coned-shape hole 3. Fixed balls (3 pieces) are tightened with variable force to the upper ball, which is rotated by electric motor, transmission and dedicated clamp. The technical data of the four-ball apparatus is showed in Tab. 3.

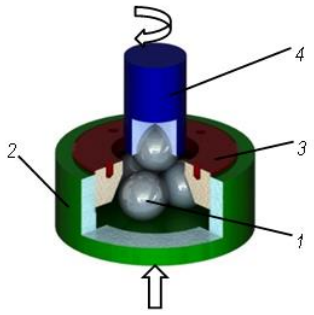

Fig. 2. The scheme illustrating the four-ball apparatus operation T-02

Tab. 3. Technical data of T-02 apparatus

Parameter	Value
- sort of movement	turning
- contact geometry	concentrated (3-point)
- nominal ball diameter	12.7 mm (0.5 in)
- rotational speed	up to 1800 rpm
- load	up to 8000 N

The oil and lubricant boundary layer durability research consists of the measurement of the wear traces diameters, formed on the surfaces of three researched fixed balls for specific load values (tightening). The T-02 device enables the run of the research in order to the method described in PN-76/C-04147 standard.

The dynamic viscosity and lubricity research was realized by stage. Every time the research was repeated three times, and the results were averaged.

3. RESEARCH RESULTS AND ANALYSIS

The dynamic viscosity of the pure vegetable oil was increasing in low temperature (Fig. 3). In 5°C the vegetable oil is characterized with ca. 30 times difference related to the diesel oil. The 20 % diesel oil addition decreases the differences by a half. Further diesel oil adding does not change the viscosity so significantly, as the first portion of 20. None of the mixtures closens significantly to the diesel oil, in the boundary researched case (80°C) the mixtures stay in the middle of the difference between vegetable and diesel oil.

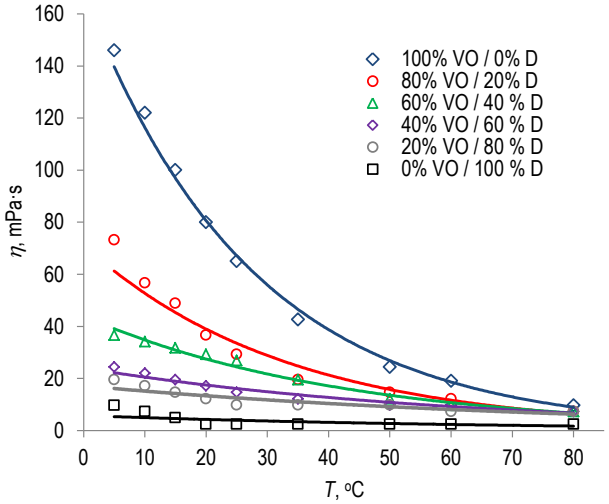

Fig. 3. Assessed values of dynamic viscosity: vegetable oil (VO), diesel (D)

The viscosity values of specific fuel mixture variants versus the temperature was approximated with expotential function, with using the non-linear regression, the method of least squares (Tab. 4).

Tab. 4. The approximation results of dynamic viscosity changes versus temperature

No	ratio	matching function	coefficient of determination
1	100% VO / 0% D	$y = 167.84e^{-0.037x}$	$R^2 = 0.9956$
2	80% VO / 20% D	$y = 71.263e^{-0.03x}$	$R^2 = 0.9691$
3	60% VO / 40% D	$y = 44.004e^{-0.024x}$	$R^2 = 0.9835$
4	40% VO / 60% D	$y = 24.043e^{-0.016x}$	$R^2 = 0.9556$
5	20% VO / 80% D	$y = 17.162e^{-0.013x}$	$R^2 = 0.8215$
6	0% VO / 100% D	$y = 5.7581e^{-0.015x}$	$R^2 = 0.4753$

The assessed viscosity values can be applicable in engine control systems. In the cases of temperature changes or the vegetable oil / diesel oil proportion change it can be selected via program method the redirection of the control module to the corresponding point on the map (Fig. 4).

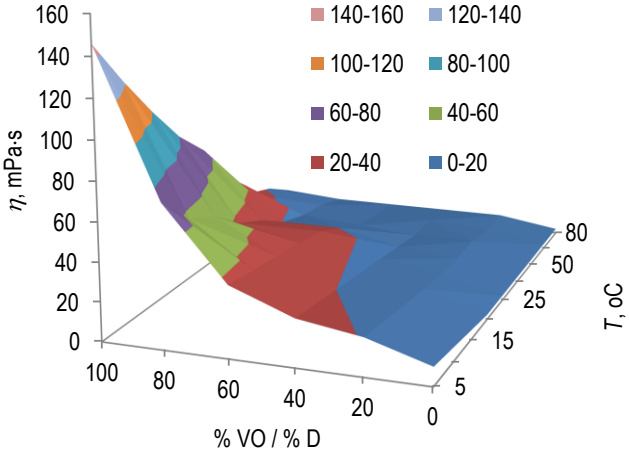

Fig. 4. Dynamic viscosity map: vegetable oil (VO), diesel (D)

It was tried to approximate with the hypersurface the results showed in Fig. 4 by using the multiple regression. Unfortunately, the function elaborated in such way is not capable of describing the whole, the boundary values do not match. Thus proposed the triangulation from result matrix to the calculation algorithms, where designated triangle suspended in space would let approximately designate the dynamic viscosity value and as an effect, application of coefficient value correcting powering system parameters.

The research showed, that dynamic viscosity values of pure vegetable oil and researched mixture with various percentage of diesel oil exceed the standard of the pure diesel oil stated by calculating relatively to the density (3.4 - 3.7) mPa·s in 40°C (Baczewki and Kałdoński, 2004). Thus the necessity of fuelling system modification occurs: bigger flow sections and fuel heating. The authors are during the elaboration of original correction of the engine control system offsetting the viscosity differences, what they are planning to show in following papers.

High viscosity values in the case of pure vegetable oil show the necessity of fuel heating in the preliminary phase of pumping in the fuelling system. Modified to power with pure vegetable oil engine control systems of presented agricultural tractors (2ndWegOil, Pasyniuk and Golimowski, 2011) besides the fuel heating system, were equipped with engine cooling system heating systems for the quickest possible nominal temperature reaching. Increased viscosity also causes problems with fuel pumping in the high pressure pump (in the case of Common-Rail), or in the injecting pump, not mentioning the injectors themselves. The vegetable oil, during flowing through the injector, especially of a new power unit with C-R system with outlet nozzles of 0.012 mm of diameter, can cause irregular dosage, what is also a research topic for authors.

The very significant feature is a lubricity of researched fuels and their mixtures in various mixing rates. As previously mentioned, injecting pump measurement operated on the vegetable oil did not show the significant wear traces (Gil et al., 2010), besides the tightness loss. Therefore attempted to check the lubricity parameter, in conditions significantly exceeding loads resulting from friction couples cooperation in fuelling system.

The flaws formed on the measuring balls were averaged. The flaws of the size up to 1.5 mm were measured with Olimpus BX 51 microscope with a magnification of (25 - 1000)x, over that value - with a magnifying Brinell glass with a magnification of 20x, with the accuracy of 0.01 mm. In Fig. 5 the sample visualization of the flaw was showed, designated with Olimpus BX 51 microscope.

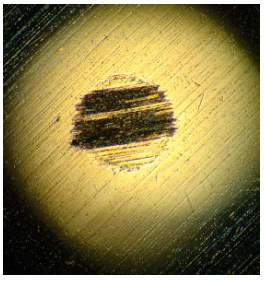

Fig. 5. Sample visualization of the flaw designated with Olimpus BX 51 microscope

As a result of lubricity attempts on four-ball apparatus, noted that the lubricant in the form of pure diesel oil causes seizure of balls with lower load, than it is in the case of mixtures and pure vegetable oil. (Fig. 6, Tab. 5).

Whereas in the case of the viscosity even insignificant diesel oil amounts caused significant decrease of mixture viscosity, in the case of lubricity - even small addition of vegetable oil to the diesel oil significantly improves the lubricity of the mixture.

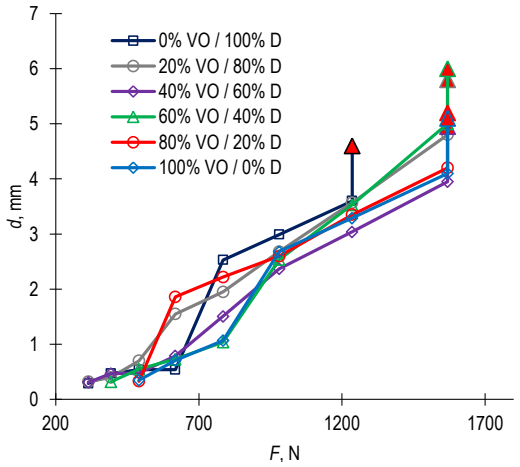

Fig. 6. Lubricity research results– flaws diameters versus load

Tab. 5. Lubricity research resutls

No	ratio	max. load N	scar diameters mm
1	100% VO / 0% D	1569	5.1
2	80% VO / 20% D	1569	5.2
3	60% VO /40% D	1569	6.0
4	40% VO / 60% D	1569	4.9
5	20% VO / 80% D	1569	5.8
6	0% VO / 100% D	1236	4.6

Marking the lubricity via measurement of the flaws diameter indicates that the engine powered with pure vegetable oil should not wear more excessively in time in the friction nodes, than the engine powered with the diesel engine. The dominant question is obviously vegetable oil pureness (Gil et al., 2010).

4. SUMMARY

Basing on the conducted research it can be stated that:

1. Pure vegetable (rapeseed) oil in the lowest of researched tempereatures showed 30 times more dynamic viscosity than the diesel oil.
2. Even small addition of the diesel oil (20 %) to the vegetable oil lowered the dynamic viscosity by 20 %.
3. For engine applications, it is necessary to heat the vegetable oil in the pumping process in the fuelling system for reaching the required viscosity. In replacement, flow sections can be increased, as far as possible, in constriction places (injector nozzles).
4. The researched vegetable oil lubricity exceeds the diesel oil lubricity, thus it should not be the cause of extensive wear or tightening loss of the fuel pumping systems.
5. Mixing the vegetable oil with the diesel oil does not change the lubricity in significant way.

REFERENCES

1. **2ndWegOil project 7**, The Framework Programme No TREN/FP7/ 219004.
2. **A policy framework for climate and energy in the period from 2020 to 2030**, Communication from the Commission to the European Parliament, The Council, The European Economic and Social Committee and the Committee of the Regions, 2014.
3. **Abschlussbericht** (2005), Praxiseinsatz von serienmäßigen neuen rapsöltauglichen Traktoren", Universität Rostock, Aktenzeichen, 00 NR 200.
4. **Amarnath H. K., Prabhakaran P., Sachin A., Bhat A., Paatil R.** (2012), A comparative experimental study between the biodiesel of karanja, jatropha and palm oils based on their performance and emsission in a four storke diesel engine, *ARPN Journal of Engineering and Applied Sciences*, 7, 407–414.
5. **Baczewski K., Kałdoński T.** (2004), *Fuel for diesel engines*, WKiL, Warsaw.
6. **Bhale P. V., Deshpande N. V.** (2009), Thombre, S.B. Improving the low temperature properties of biodiesel fuel, *Renew. Energy* **2009**, 34, 794–800.
7. **Bocheński C. I., Bocheńska A. M.** (2005), Testing properties of engine oil mix with rape oil methyl esters, *MOTROL - Motorization and Power Industry in Agriculture,* Vol. 7, 24-34.
8. **Bocheński C. I., Warsicki K., Bocheńska A. M.** (2005), Comparison of process of stream creation and diesel oil and rape oil esters combustion in the research combustion chamber at single – and diphause fuel injection, *Journal of KONES Internal Combustion Engines*, Vol. 12(3-4), 33-42.
9. **Canakci M.** (2007), Combustion characteristics of a turbocharged DI compression ignition engine fueled with petroleum diesel fuels and biodiesel, *Bioresour. Technol.*, 98, 1167–1175.
10. **Cisek J., Mruk A.** (2012), Characteristics of a diesel engine fuelled by natural rape oil, *Proceedings of the Institute of Vehicle, Faculty of Automotive and Constuction Machinery Engineering, Warsaw University of Technology*, Vol. 1(87), 5-16.
11. **Commission Directive** 2010/26 / EU of 31 March 2010. Amending Directive 97/68 / EC of the European Parliament and of the Council on the approximation of the laws of Member States relating to measures against the emission of gaseous and particulate pollutants from internal combustion engines to be installed in non-mobile machinery on the road.
12. **Directive of the European Parliament and of the Council** 2009/28 / EC of 23 April 2009. In the promotion of energy from renewable sources and amending and subsequently repealing Directives 2001/77 / EC and 2003/30 / EC.
13. **Durbin T. D., Collins J. R., Norbeck J. M., Smith, M. R.** (200), Effects of biodiesel, biodiesel blends, and a synthetic diesel on emissions from light heavy-duty diesel vehicles,*Environ. Sci. Technol.*, 34, 349–355.
14. **Dzieniszewski G., Piekarski W.** (2006), The select problems of feeding diesel engines with low-processed rape oil, *Eksploatacja I Niezawodność*, Vol. 3, 58-65.
15. **Emberger P., Thuneke K., Remmele E. (2012),** *The pure vegetable oil suitable tractors of the stage IIIA. Results of test runs and field operation conducted on premises of the Bavarian State Research Center for Agriculture*, (in German). Berichte aus dem TFZ, 32, Straubing.
16. **Gil L., Ignaciuk P., Niewczas A.** (2010), Investigation of wear of injection system components in diesel engine fueled with vegetable fuels, *Journal of Science of the Gen. Tadeusz Kosciuszko Military Academy of Land Forces*, Vol. 4(158), 100-108.
17. **HLPE** (2013), Biofuels and food security. A report by the High Level Panel of Experts on Food Security and Nutrition of the Committee on World Food Security, Rome.
18. **Kaplan C., Arslan R., Surmen A.** (2006), Performance characteristics of sunflower methyl esters as biodiesel, *Energy Sources Part A Recovery Util. Environ. Eff.*, 28, 751–755.
19. **Karavalakis G., Stournas S., Bakeas E.** (2009), Light vehicle regulated and unregulated emissions from different biodiesels, *Sci. Total Environ.*, 407, 3338–3346.
20. **Łaska B., Wawrzyniak A., Szulc R., Golimowski W., Pasyniuk P.** (2013), Comparsion of physical and chemical properties of crude coldpressed vegetable oils used to drive agricultural tractors, *Journal of Research and Applications in Agricultural Engineering*, Vol. 58(2), 116-118.
21. **Lasocki J., Karwowska E.** (2010), The influence of microorganisms present in diesel and biodiesel on the fuel systems of vehicles equipped with diesel engines, *The Archives of Automotive Engineering - Archiwum Motoryzacji*, Vol. 3, 167-183.
22. **Lin B. F., Huang J. H., Huang D. Y.** (2009), Experimental study of the effects of vegetable oil methyl ester on DI diesel engine performance characteristics and pollutant emissions, *Fuel*, 88, 1779–1785.
23. **Lin Y., Wu Y. G., Chang C.** (2007), Combustion characteristics of waste-oil produced biodiesel/diesel fuel blends, *Fuel*, 86, 2810–2816.
24. **Monyem A., Van Gerpen J. H.** (2001), The effect of biodiesel oxidation on engine performance and emissions, *Biomass Bioenergy*, 20, 317–325.
25. **Muncrief R. L., Rooks C. W., Cruz M., Michael P. H.** (2008) Combining biodiesel and exhaust gas recirculation for reduction in NOx and particulate emissions, *Energy Fuels*, 22, 1285–1296.
26. **Nabi M. N., Akhter M. S., Zaglul Shahadat M. M.** (2006), Improvement of engine emissions with conventional diesel fuel and diesel-biodiesel blends, *Bioresour. Technol.*, 97, 372–378.
27. **Opinion of the European Economic and Social Committee on the Proposal for a Directive of the European Parliament and of the Council amending Directive 98/70** / EC relating to the quality of petrol and diesel fuels and amending Directive 2009/28 / EC on the promotion of energy from renewable sources COM (2012) 595 final - 2012/0288 (COD).
28. **Pasyniuk P., Golimowski W.** (2011), Effect of rapeseed oil on the parameters of a diesel engine of John Deere tractor, model 6830, *Journal of Research and Applications in Agricultural Engineering*, Vol. 56(2), 118-121.
29. **Raheman H., Phadatare A. G.** (2004), Diesel engine emissions and performance from blends of karanja methyl ester and diesel, *Biomass Bioenergy*, 27, 393–397.
30. **Szlachta Z., Dudek S.** (2003), The biofueling agricultural vehicle engines, *MOTROL - Motorization and Power Industry in Agriculture,* vol. 5, 192-200.
31. **Tesfa B., Gu F., Mishra R., Ball A.** (2014), Emission Characteristics of a CI Engine Running with a Range of Biodiesel Feedstocks, *Energies*, 7, 334-350.
32. **Ulusoy Y., Tekin Y., Cetinkaya M., Karaosmanoglu F.** (2004), The engine tests of biodiesel from used frying oil, *Energy Sources*, 26, 927–932.
33. **Wasilewski J.** (2006), Comparative assessment of fuel consumption by tractor engine fed with rapeseed biofuel and diesel fuel, *Inżynieria Rolnicza*, Vol. 6, 349-355.
34. **Wcisło G.** (2008), Determination of temperature impact on dynamic viscosity of plant biofuels, *Inżynieria Rolnicza*, Vol. 10(108), 277-282.

The investigations described in this paper are a part of the research project WND-RPPD.01.01.00-20-015/12 Fri. *Examination of the effectiveness of active and passive methods to improve energy efficiency infrastructure using renewable energy sources* Priority Axis I. Increased innovation and supporting entrepreneurship in the region, Measure 1.1. Creating conditions for the development of innovation, co-financed by the European Regional Development Fund and the state budget under the Regional Operational Programme 2007-2013 Podlaski "TO-120362/106/14 realized at Bialystok University of Technology.

DOI 10.1515/ama-2015-0004

DIAGNOSTICS OF GEARS AND COMPRESSORS BY MEANS OF ADVANCED AUTOMATIC SYSTEM

Jerzy TOMASZEWSKI*, Jacek RYSINSKI*

*Faculty of Mechanical Engineering and Computer Science, Department Of Mechanical Engineering Fundamentals, University of Bielsko-Biala, ul. Willowa 2, 43-300 Bielsko-Biala, Poland

jtomaszewski@ath.bielsko.pl, jrysinski@ath.bielsko.pl

Abstract: In the present paper, the diagnostics problems of gears and air-compressors are discussed. The diagnostics has been performed by means of wireless system WiViD. This system is a unique design solution, in which several functions are divided and performer by two separate devices. The mentioned device functions are as follows: data handling, processing, their analysis and presentation. In the paper, own measurement procedures were created, checked and presented. The evaluation of technical conditions of some devices was done based upon the registered diagnostic symptoms, which were compared with the allowable limits.

Key words: Gears, Air-Compressor, Diagnostic

1. INTRODUCTION

Nowadays, diagnostics is a common practice aiming for an evaluation of technical state of devices and elements of the drive systems working in the industrial technological lines. Rapid development of this method was possible due to the fact that wide range of modern devices is available on the market. By means of these devices, the diagnostics activities – which allow for adequate evaluation of machine state - can be performed in real time. Among the devices which are currently available, the machine diagnostic system named WiViD, produced by Polish firm Alitec from Łódź, could be easily and effectively used.

System WiViD™ is a unique design solution, in which several functions is divided and performer by two separate devices. The mentioned device functions are as follows: data handling, processing, their analysis and presentation.

The basic executive element of the system is: wire-less, multicanal measurement board mounted inside the shock-proof, ergonomic housing. The measurement head allows for measurements of vibrations in three directions, within the very broad frequency band (0.4Hz -20kHz). The potential range of application is even extended via a possibility of connection of an external gauge CLPS type (i.e. vibration and forces gauge as well as microphone), additional there is the connection of signal of phase indicator. All measurements are synchronically performed. The device could be utilized as a mini infra-red (thermo-vision) camera, displaying a thermal image of point resolution 16x4, within the temperature range -50°C do 300°C.

Second element of the system could be: a smartphone or a tablet – working under control of the operational system Android (version 4.x). The specialized software gathers measurement information in the mobile data base. After conversion, they are presented in a clearly way on the screen. The software integrates the set tools for an evaluation of technical state of such machine parts like e.g. bearings, elements of drive systems and transmissions.

In the paper, the examples of an application of the afore-mentioned device for diagnostics of compressors and gears are described.

The methodology of evaluation of technical state of a gear within its working time was prepared. In consequence, it was prepared several measurement rules e.g.: the procedure of determination of thresholds for point estimates of vibration signal measured on the gear bearing housings as well as the procedure of evaluation of technical state based upon the earlier determined thresholds.

2. DIAGNOSTICS OF SCREW COMPRESSORS

Screw compressors (Fig. 1.) are devices dedicated for compression of gases. The processof compression of gas (in our case i.e. air) consists in diminishing of the space between rotating screws - from the suction (intake) connector holes up to exhaust holes (outlet).

Fig. 1. Screw compressor

The value of compression, in these compressors, depends on their design (construction), moreover the efficiency of the compression element itself depends (mainly) upon the tightness level achieved between both screws as well as between screws and housing. The basic parts of the screw element are rotors – in Polish so called – male and female ones, rotating in opposite directions when simultaneously the space between them and the housing consequently diminishes.

DOI 10.1515/ama-2015-0004

2.1. Diagnostics of compressors: approval and run

In case of approval diagnostics, evaluation of quality can be performed in accordance with the standard VDI 3836 (2012), which is subsidiary to the standard ISO 10816-3 (2009). According to the standard VDI 3836, the compressors can be divided into 4 groups:

- Group no 1. Screw compressors with a sliding bearing, with gears. The compressors belonging to this group are utilized for compression of ordinary process gases (P≥55kW).
- Group no 2. Screw compressors, equipped with rolling and sliding bearing as well as gears. Air, oil-less compressors are usually classified as belonging to this group (P≥37 kW).
- Group no 3. Screw compressors, without gears. The compressors filled by oil usually belong to this group (P≥55 kW).
- Group no 4. Roots's blowers, with rolling bearing and gears (P≥22 kW).

Assessment/Evaluation of manufacturing quality, according to this standard, consists in analysis of three zones:

- *Zone no I.* Compressors, which vibrations are within this zone, are considered as suitable for continuous exploitation without any restrictions.
- *Zone no II.* Compressors, which vibrations are within this zone, have high values of vibration. In each individual case, it should be checked weather the measurements of vibrations allows for continuous exploitation taking into account designed and real work conditions for a particular device. In general, these compressors can be used by a particular time under the current conditions, until the inspection or repair procedure.
- *Zone no III.* Compressors, which vibrations are within this zone, are designated for repair, because their vibrations values are recognized as so high that can cause damage of a particular machine.

The numerical values assigned to the limits of zones do not be considered as the values guaranteed by the producer. These values have to be agreed between a producer and a client exploiting a compressor. However, these values give information which allows for excluding serious errors as well as unrealistic demands. In some cases, especially for untypical compressor (having special properties), other zone limit values (greater or lower) can be demanded. In such cases, it is necessary to obtain producer confirmation that the compressor can be safely exploited under higher vibrations' values. The exemplary limits of zones for an evaluation of the housing - for the approval measurements for the I-st group of compressors are shown in Tab. 1.

Choice of measurement bands for evaluation of compressors is different in comparison to the recommendations given in the standard PN- ISO-10816-1 (1995). The values - which is used for evaluation of a compressor - are the effective amplitude of vibration velocity for two bands - are:

- for the band A – lower limit of the filter is equal to 0.5 Hz, whereas the upper limit is determined based on third characteristic harmonics for compressor elements and variables - like e.g.:
  - frequencies of main gear, synchronous:
    $$f_z = f_0 \cdot z \quad (1)$$
    where: z – number of teeth of pinion,
  - frequencies of belt gear:
    $$f_k = k \cdot (\pi \cdot f_0 \cdot D_s)/l_k \quad (2)$$
    where: k – number of belts, D_s – pitch diameter of belt wheel (pulley), l_k – belt length,
  - frequency of co-operation screw rotors:
    $$f_H = f_0 \cdot z_H \quad (3)$$
    where: z_H – number of coils of the screw.

Tab. 1. Zones' limits for evaluation of compressors of the I-st group. Effective value of velocity [mm/s]

Group	Support type	Zone type	Measurement band A	Measurement band B
Group I	Stiff	I/II	8.0	3.5
		II/III	12	4.5
	Flexible	I/II	10.0	4.5
		II/III	15.0	7.0

The calculated third harmonic is rounded up according to the method given in the cited standard.

- for the B band, the lower limit of filter is equal to 0.5 Hz, whereas the upper maximal value of this band is determined by means of the formula: $f_g = 2.2 \cdot f_0$ which is rounded to 10 Hz. (Example: if we calculate $f_g = 56.7$ Hz , then we finally consider value 60 Hz).

In case of diagnostics of technical state of exploited compressors, we have to consider the values of zone I/II multiplied by 1.25 for the warning limit, whereas for the alarm limit, one have to multiply the value of zone II/III by 1.25.

In case of diagnostics of oil compressors, the value of pick acceleration amplitude (0-Peak), within the band 0.5Hz – 5 kHz, should not exceed the limit 15g.

2.2. Example of evaluation of technical state of screw compressor

Screw compressor shown in Fig. 2, of parameters given in Tab. 2, worked by one year from the date of its mounting in a particular factory.

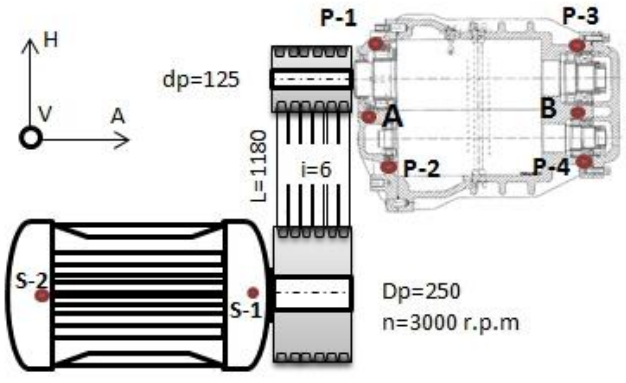

Fig. 2. Scheme of screw compressor which technical state was evaluated: rated power 55 kW, rated rotations: 2995 rev/min, maximal work pressure – 10 bar, number of coils of male screw: 4

Firstly, measurement bands A and B for a particular compressor have to be established. The rotational frequency of the input shaft is equal to $f_0 = 49.9$ Hz, for which the characteristic frequency of the compressor - calculated by means of formula (3) –

is equal to $f_H = 199.6$ Hz. The measurement band A, calculated based on third harmonics is equal $3 \cdot f_H = 599$ Hz, which is round up to the value 500 Hz. The band is equal to 1000 Hz.

The measurement band B, for which the characteristic frequency is equal to $2{,}2 \cdot f_o = 109.8$ Hz, but after rounding by 10 Hz – it is equal to 110 Hz. The measurements of effective amplitudes of velocities, within the measurement bands A and B, are listed in Tab. 2.

Tab. 2. Results of measurements of effective velocity amplitudes for the compressor

Point no	Band A (0.5Hz – 1000 Hz)			Band B (0.5Hz – 110 Hz)		
	A	V	H	A	V	H
1	2.3	2.2	2.3	0.4	0.2	0.3
2	1.5	2.3	1.7	0.3	0.3	0.3
3	10.3	2.6	4.8	0.7	0.8	0.5
4	3.3	4.4	2.6	0.3	0.5	0.7

The compressor could be qualified to group no II, for which - for band A, the zone I/II has value 10 mm/s, whereas the zone II/III has value 15 mm/s. For band B, the zone I/II has value 3 mm/s, whereas the zone II/III 7 mm/s, respectively.

The level of vibrations of the compressor – for band A – is qualified as belonging to the zone II. Based upon the analyses, the cause of occurrence of the essentially high values of vibration amplitudes – has to be checked (explained). The problem is connected with point no 3 in A direction. The procedure has to be performer in accordance with the demands of the standard. The decision should be taken: approval of the compressor for further exploitation (without any restrictions) or the exploitation should be restricted (terminated), until the moment when the prevention/repair actions will be performed.

3. DIAGNOSTICS OF CHOSEN DAMAGES OF GEARS

Sample test-stand with WiWiD system is presented in Fig. 3.

Fig. 3. Test stand: 1. investigated gear, 2. measurement device WiViD, 3. register-analytical device (smartphone)

Among versatile known diagnostics methods dedicated for detection of damages, in practice only the following methods are commonly applied: analysis of vibration spectrum and envelope spectrum. These methods were utilized for diagnostics of technical state of some strategic devices (installations) in the cement plant Dyckerhoff within a period of 10 years. The basics for determination of methodology of diagnostics of gear damages was the methodology described in book: Barkov and Barkowa, 1996; Choy et al., 1996; Feng and Ming, 2012; Feng and Zuo, 2013; Mirota et al., 2009; as well as an experience of the author achieved during diagnostics routines aiming for evaluation of technical state of devices in cement plants.

For each kind of damage, three types of symptoms were distinguished which indicate the particular kind of damage. These symptoms are as follows:

- band of frequency – in which an increase of the pick amplitude can be observed. We can recognize three band ranges for analysis – for the gears of general purpose of usage [9]: band of low frequency 0 – 300 Hz, band of medium frequency 300 – 3000 Hz and band of high frequency > 3000Hz,
- existence of particular order (sequence) of components in the spectrum of vibrations' accelerations,
- existence of particular order (sequence) of components in the envelope spectrum of vibrations.

In this method, it was assumed that the highest priority is assigned for a phenomenon of existence of a particular configuration of compounds in the envelope of vibrations' accelerations. The determination of this envelope is performed based on the adequate rules. Before determination of an envelope, the signal of vibrations should be subjected to the filtration procedure using upper-passing filter. Moreover, the cut frequency should be established in such a way – that for values of frequency above f_f dominant compound should not be present. In practice, the value of cut band for a utilized filter is chosen from the interval $f_f = 5\ kHz \div 12\ kHz$.

An analysis of methods of diagnostics for particular kinds of damages of a gear shows that one symptom can diagnose several different damages. This phenomenon causes in consequence a necessity of eye inspections of meshing's (mating gear elements) aiming for determination of damage kind.

3.1. Examples of application of the method

During the periodical diagnostics inspections of drive gears, which functional scheme is presented in Fig. 4, it was observed that the alarm limits were crossed over - especially the alarm limits of estimates of pick amplitude of acceleration within the band 300 Hz – 3000 Hz.

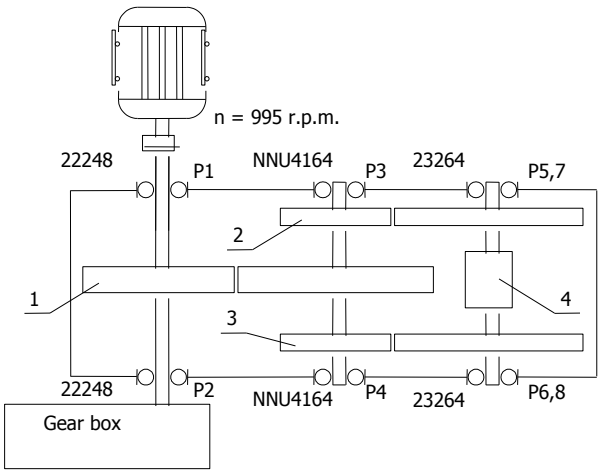

Fig. 4. Kinematical scheme of drive gear where displacement of measurement point is shown

In Fig. 5, trend of variations of pick amplitude of accelerations within the band 300 Hz – 3000 Hz is shown.

Analysis of measurement results of pick amplitude within the band above 3 kHz does not show any crossing over of the warning threshold (lack of increase of high frequency spectrum i.e. above

DOI 10.1515/ama-2015-0004

3 kHz). Spectrum of vibrations' accelerations – determinate in point 1V – is shown, in Fig. 6.

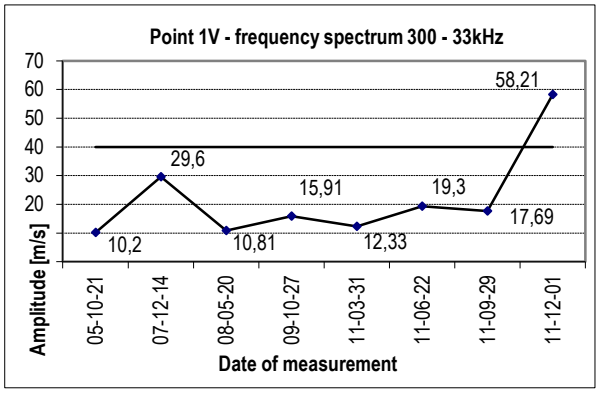

Fig. 5. Trend of changes of the pick amplitude of acceleration – determined in measurement point no 1 in a vertical direction

In the discussed vibration spectrum, one can observed the components adequate for the meshing of the gear input stage. Moreover, there are side ribbons in the distance of the rotational frequency of the gear input shafts. In the envelope spectrum, show in Fig. 7, determined in point 1V, one can observed the dominant components connected with the rotational frequency of the gear second shaft.

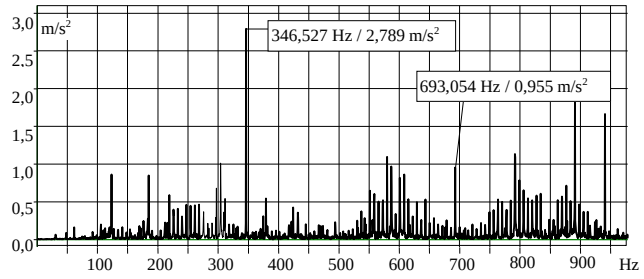

Fig. 6. Spectrum of accelerations - determine in point 1V of gear

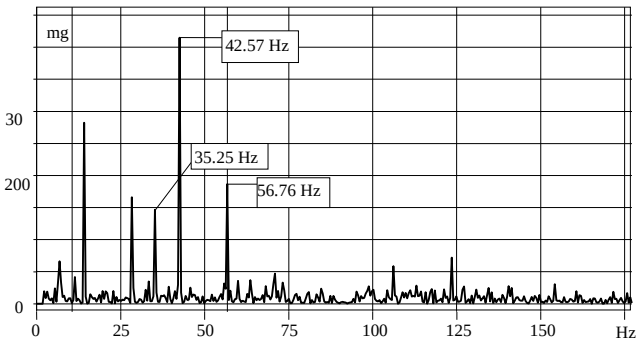

Fig. 7. Envelope spectrum determined in point 1V determined within the band above 8 kHz

Harmonics (above 4 (k > 4)) of rotational velocity of the second shaft in the envelope spectrum can be spotted. It means the defect of the gear wheel of the drive first stage.

The presented example show effectiveness of the diagnostics methods, based on an analysis of spectrum and envelope spectrum of the signal measured on the bearing housing – in which works the damaged element of gear. Based upon the long-year practice, it can be stated that the measurements of vibration signal on both bearing housings are needed for an effective diagnostics. In the described example, the phenomenon of crossing over of the warning pick amplitude within the band 300-3000Hz – exists only on the bearing housings 1 and 2. In other measurement point of the gear – this phenomenon was not observed.

4. CONCLUSIONS

In the present paper, two methods of diagnostics of the chosen machine types are discussed. The descriptions of their usage show complexity of the diagnostics process – where diagnosis of technical state of a device is done based upon the analysis of vibration signal (Farrahi et al., 20122; Rama and Dutta, 2012). Diagnostics methods dedicated to screw compressors are different than the common methods of evaluation of technical state of machine/device based on the standard ISO 10816 (1-7) as well as on its Polish equivalent PN-ISO 10816-1. Compressors belong to the group of simple machines, which are subjected to the mentioned standards, on contrary - gear belongs to the group of compound machines.

Compound machines cannot be evaluated upon the standard ISO 10816(1-7), due to the facts that versatile attempts of performance an evaluation of technical state utilizing these standards have not issued reliable information about their technical state. Therefore, diagnostics of compound machines have to be performed using other methods, e.g. via determination of individual diagnostics limit values, applying several different signal estimates.

The experimental investigations were carried out by means of the wireless measurement system WiViD. All the registered measurements were analyzed by means of own software routines.

REFERENCES

1. **Barkov A. V., Barkova N. A.** (1996), Diagnostics of gearings and geared couplings using envelope spectra methods, *Proceedings of the 20th Annual Meeting of the Vibration Institute. Saint Louis, Missouri USA,* 75-83.
2. **Choy F. K., Polyshchuk V., Zakrajsek J. J., Handschuh R. F., Townsend D. P.** (1996), Analysis of the effects of surface pitting and wear on the vibration of a gear transmission system, *Tribology International*, Vol. 29, No. 1, 77-83.
3. **Farrahi G. H., Tirehdast M., Masoumi K. A. E., Parsa S., Motakefpoor M.** (2011), Failure analysis of a gas turbine compressor, *Engineering Failure Analysis,* Vol. 18, No. 1, 474-484.
4. **Feng Z., Zuo M.J .** (2013), Fault diagnosis of planetary gearboxes via torsional vibration signal analysis, *Mechanical Systems and Signal Processing,* Vol. 36, No. 2, 401-421.
5. **Feng Z. Z., Ming J.** (2012), Vibration signal models for fault diagnosis of planetary gearboxes, *Journal of Sound and Vibration*, Vol. 331, No. 22, 4919-4939.
6. **ISO 10816-1** (1995), Mechanical vibration – Evaluation of machine vibration by measurements on non-rotating parts – Part 1: General guidelines.
7. **ISO 10816-3** (2009), Mechanical vibration – Evaluation of machine vibration by measurements on non-rotating parts – Part 3: Industrial machines with nominal power above 15 kW and nominal speeds between 120 r/min and 15 000 r/min when measured in situ.
8. **Mirota K., Tomaszewski J., Rysiński J.** (2009), Diagnostics of scoring in gears, *Solid State Phenomena*, 144, 118-123.
9. **Rama R. A., Dutta B. K.** (2012), Vibration analysis for detecting failure of compressor blade, *Engineering Failure Analysis*, Vol. 25, 211-218.
10. **VDI 3836** (2012), Measurement and evaluation of mechanical vibration of screw-type compressors and roots blowers, Addition to DIN ISO 10816-3.

THE SEARCH OF SPATIAL FUNCTIONS OF PRESSURE IN ADJUSTABLE HYDROSTATICRADIAL BEARING

Dmytro FEDORYNENKO*, Sergiy BOYKO*, Serhii SAPON*

*Mechanical Engineering Department, Chernihiv National University of Technology,
95 Shevchenka Str., 14027 Chernihiv, Ukraine

fdy@mail.ru, svboyko.cstu@gmail.com, s.sapon@gmail.com

Abstract: The analysis of spatial functions of pressure considering the geometrical deviations and the elastic deformation of conjugate surface have been considered. The analysis of spatial functions of pressure is performed by the finite element method. The difference of the size of pressure in a tangential direction of a pocket of a support under various service conditions has been investigated. A recommendation for improving of operational characteristics in regulated hydrostatic radial bearing has been developed.

Key words: Hydrostatic Bearing, Lubricating Film, Spatial Functions, Hydromechanics, Reynold's Equation

1. INTRODUCTION

The main characteristics to calculate the hydrostatic bearing (HB), as well as other types of sliding bearings is a function of the pressure distribution. From its solution depends on the accuracy of calculations. Therefore, the calculation of the pressure distribution in the lubricating film HB has been given much attention.

The basis of calculation of the pressure distribution in the lubricating film is the basic equation of Hydromechanics (Michael, 2012):

– Navier-Stoke's

$$\frac{\partial \vec{V}}{\partial t} + \left(\vec{V}\nabla\right)\vec{V} = F - \frac{1}{\rho} grad(p) + \nu\nabla^2\vec{V} \qquad (1)$$

– indissolubility of flow

$$div\rho\vec{V} = 0 \qquad (2)$$

where: $\vec{V}$– particle fluid velocity vector in the point of space with the coordinates x, y, zat a certain time t; ∇– Hamiltonian operator; F – volume forces acting on a fluid particle; ρ, ν – density and coefficient of kinematic viscosity of the fluid; ∇^2 – Laplace operator.

For isothermal ($\nu = \text{const.}$) laminar, steady motion of a viscous and uncompressed fluid ($\text{div}\rho\vec{V} = 0, \rho = \text{const}$) considering order of magnitude in the previous equations, we can write in the Cartesian coordinate system:

$$\frac{\partial p}{\partial x} = \mu\frac{\partial^2 u}{\partial y^2}; \frac{\partial p}{\partial y} = 0; \frac{\partial p}{\partial z} = \mu\frac{\partial^2 w}{\partial z^2}; \quad \frac{\partial u}{\partial x} + \frac{\partial v}{\partial y} + \frac{\partial w}{\partial z} = 0 \qquad (3)$$

where:μ – coefficient of the fluid dynamic viscosity; u, v, w– projection of fluid particle velocity vector on the axes ox, oy, oz respectively.

By integrating the continuity equation (the last equation in system (3)) to $\boldsymbol{y}$ within the limits the clearance in the HB considering boundary conditions (Kiogora et al., 2014) we get the equation for the Reynold's pressure in the radial HB.

Analyzing the research conducted in Kiogora et al. (2014), it can be concluded that the final Reynold's equation in a cylindrical coordinate system is a linear non homogeneous differential equation in partial derivatives of second order elliptic type with two independent variables φ, $\bar{z}$(angle of working chamber in HB and working length, respectively). In general case this equation has no analytical solution. Therefore, for the approximate decision of Hydromechanics tasks and study of the static characteristics of HB in practice various methods are used: finite differences, variation methods for differential equations in partial derivatives, finite element method and finite volumes (McDonald, 1971). The most common - finite volume method, which is described in Strutynsky and Fedorynenko (2011).

2. ANALYSIS OF RECENT RESEARCHES AND PUBLICATIONS

The most convenient for the numerical solution of Reynold's equations is the method of finite differences, with which you can get a set of discrete values of the approximate solution of differential equations in the investigated area, which is covered by mesh. According to this method the differential task is replaced by finite differences and difference solution is defined on the mesh.

In Strutynski and Fedorynenko (2011) this method is used for the numerical solution of Reynold's equation and static characteristics of HB. In this paper the reamer of the working chamber bearing on the plane has been investigated. Using the method of finite differences differential Reynold's equation has been approximated and the second order partial derivatives have been replaced by their difference analogous. To solve received systems of equations were used iterative methods which compared with direct, have a number of advantages, first of all, these methods require fewer arithmetic operations to achieve a solution and quite easily are programmed on a computer.

The result of the calculation is the spatial pressure diagram $\bar{p}(\varphi, \bar{z})$ on Fig. 1 built for the domain of the function, which is limited by the working chamber. φ – Is the angle of the bearing working chamber, $\bar{z}$ – the geometric dimensions of the working chamber.

DOI 10.1515/ama-2015-0005

The method of finite differences considered in Strutynski and Fedorynenko (2011) for the numerical solution of Reynold's equation and static characteristics of HB requires the development of complex mathematical models and complex calculations.

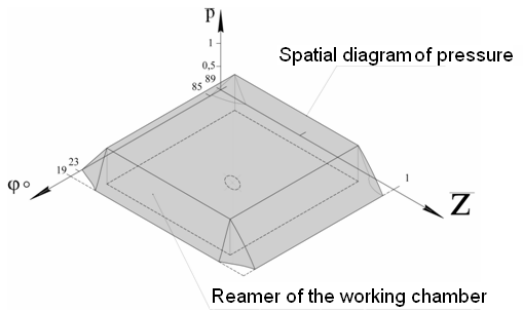

Fig. 1. Spatial diagram of the pressure which is obtained by the method of finite differences

The purpose of the paper is the analysis of spatial functions of pressure considering the geometrical deviations and the elastic deformation of conjugate surface by the finite element method and development of recommendations for improving of operational characteristics in regulated hydrostatic radial bearing.

3. METHODS

The most common approaches to the numerical solution of differential Reynold's equations, besides, considered method of finite differences – is the finite elements method and finite volumes. These methods are based on discretization liquid medium finite element, which is the solution of the problem by the set of interpolation functions. Finite volume method is a particular, quick case of the finite element method (McDonald, 1971).

To solve this problem effectively has been proposed the usage of modern CFD software packages in particular CosmosFloWorks. In this software the fluid motion is modeled by using Navier-Stoke's equations which describe the laws of momentum conservation, mass, energy, fluid environment. To search a solution of this problem is used discretization of Navier-Stoke's equations on the surface of finite volume of a computational grid. More detailed foundations of the method of finite volumes and algorithms for finding solutions on discrete meshes have been covered in the monographs Reddy and Gartling, (2010).

Let us consider the approaches to finding spatial functions of pressure in adjustable radial HB by means of CFDCosmosFloWorks.

The object of analysis is an adjustable radial HB, basic design of which is shown in Fig. 2.

The design of the adjustable radial HB consists of the following elements: 1 – case, 2 – conical bushing, 3 – hydrostatic bushing, 4 – working chamber, 5 – cover, 6 – nut, 7 – choke, 8 – spindle, 9, 10 – bulkheads.

Assumptions as for the model of hydrodynamic analysis are as following (Fedorynenko, 2012):

- The movement of fluid in the flow area of HB can be attributed to "slow" flow of liquid. Therefore, the forces of inertia and mass forces are negligible compared with the pressure forces and forces caused by the viscosity of the liquid.
- For medium and high speed HB with $V_\varphi < 70$ m/s (V_φ - linear speed of a spindle bearing surface in the tangential direction) and $\delta_0 > 10$ microns (δ_0 – backlash) it is possible to use the problem in the isothermal formulation with the averaged values of the temperature in the flow holes of the bearing.

Lubricant – Newtonian fluid, the pressure of lubricant layer is constant, sliding on the boundaries of a backlash and the gap in the liquid layer are absent (accepted Sommerfeld hypothesis), the thickness of the lubricant layer is small compared with the radius of the bearing, lubricant viscosity is accepted with some averaged temperature, the gradient of pressure in working chamber is zero.

a)

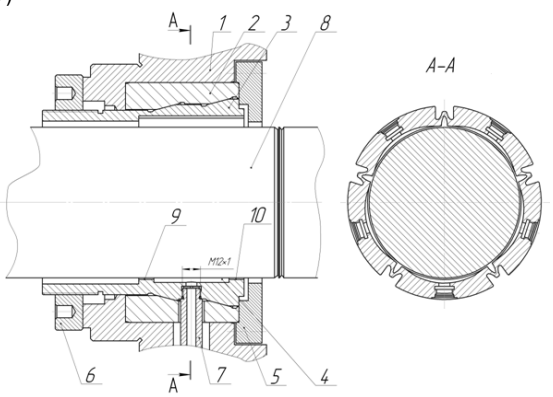

b)

Fig. 2. Drawing of adjustable radial HB a) and appearance b)

For calculations were used solid-state 3D model of the hydrostatic bearing. To solve the problem were taken into account geometric deviation of bearing surfaces in the tangential direction of HB by identifying the cross section of shapes of the spindle bearing surface, which corresponds to the function of the radial backlash with deviations geometry of conjugate surface (Strutynski and Fedorynenko, 2011).

To determine the calculated domain (the domain of function definition) it was necessary to specify its boundary in space. The boundary of the calculation is the bearing surface of HB. In order to simulate the fluid flow through the holes in the solid model were used special covers (Sahno et al., 2009), which are shown in Fig. 3. The surface of these covers is interpreted in CosmosFloWorks as a hole on the inner surface (on Fig. 3 are shown by arrows) that define the boundary conditions.

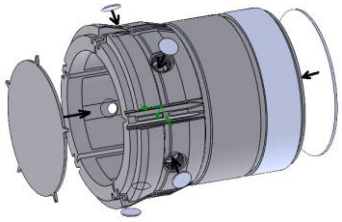

Fig. 3. Entering of boundary conditions on the 3D model (the spindle is not shown)

On the input covers (corresponding to apertures for supplying the liquid in the chamber of HB) was specified the static value of fluid pressurep_{k_i}. The output covers are analogues of holes on the end surfaces of the bearing, on the inner surfaces of which was set the drain pressure p_d The boundary condition on the supporting surface of the spindle is the rotational speed, which is $n_s = 2000\ \mathrm{min}^{-1}$.

As a result of the calculation was obtained the spatial diagram of the pressure on the supporting surface of the HB, which is presented in Fig. 4.

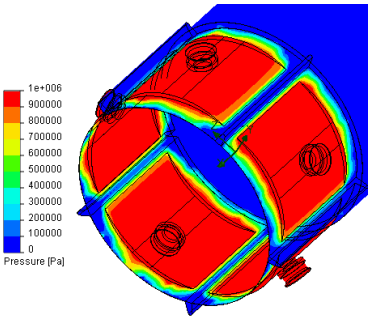

Fig. 4. The spatial diagram of the pressure on the supporting surface of adjustable radial HB

The format of the data in Fig. 4 provides only a qualitative picture of the pressure distribution in the bearing. Quantitative evaluation of the scalar field of the pressure at some points of liquid medium using spatial diagrams is more complicated. To determine the fluid pressure in the specific sections of HB was proposed the age of spatial grid of sketches (Fig. 5), covering the study area of the bearing surface in the axial and tangential directions.

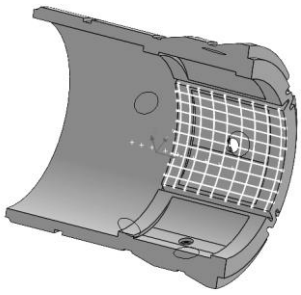

Fig. 5. The grid of sketches for analysis functions $p(\phi, z)$ on the area limited by a separate chamber of bearing

By the means of CosmosFloWorks for each sketch was determined fluid pressure dependence from the length of the line sketch. In Fig. 6 are shown dependences of fluid pressure, as defined by the length of the sketches in the axial (Fig. 6a) and tangential (Fig. 6b) directions of HB.

By the means of a grid of sketches (see Fig. 5) were constructed the spatial diagrams of pressure, which is shown in Fig. 7.

Let us compare the results of calculations of differential Navier-Stoke's equations by the method of finite differences and finite volumes.

The function of the pressure $p(\varphi, z)$ along the length of the tangential bulkheads in the axial direction of the bearing (see Fig. 1 and Fig. 6, 7) is qualitatively and quantitatively similar for both methods of numerical calculation.

There are also differences in the obtained solutions. On the end of the bearing surfaces of HB and the edges of drainage grooves in modeling functions of pressure by means of CosmosFloWorks were received non-zero values of fluid pressure (Fig. 6)as opposed to problem solution by finite differences, where the fluid pressure was equal to zero. Along the length of chambers in the tangential direction of the bearing the pressure difference is observed (see Fig. 6 and 7), which is caused by the rotation of the spindle, which does not meet the boundary conditions with the constant pressure value p_{k_i} if finding problem solution by finite differences (see Fig. 1). It was proved that the increase of fluid pressure in tangential length of the bearing chambers takes place in the direction of rotation of the spindle (Sakhno et al., 2009; Fedorynenko et al., 2013).

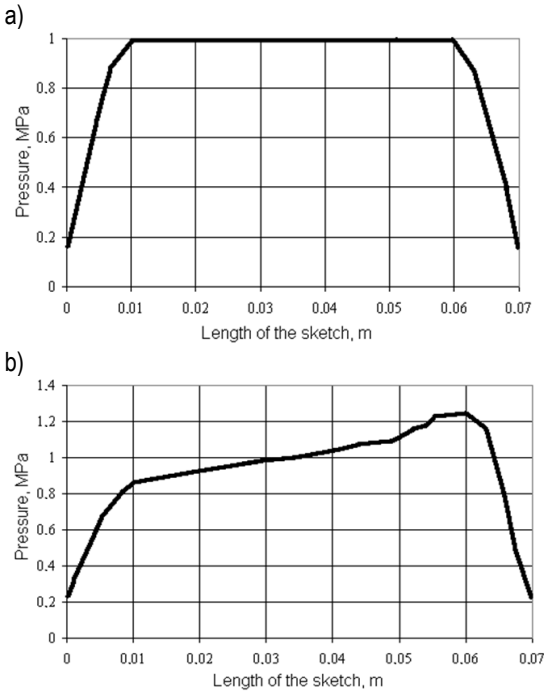

Fig. 6. Typical characteristics of fluid pressure distribution in the axial a) and tangential b) directions of HB

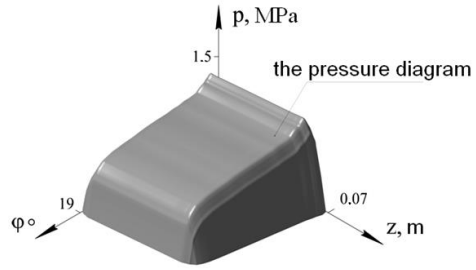

Fig. 7. The function of fluid pressure $p(\phi, z)$ in the chamber of HB

The pressure difference in the i – th chamber caused by the rotation of the spindle can be characterized by a dimensionless quantity $\Delta\overline{p}_i$that is defined as:

$$\Delta\overline{p}_i = \frac{|p(\varphi_{\tau k_1}, z_c) - p(\varphi_{\tau k_2}, z_c)|}{p_{k_i}} \qquad (4)$$

As a result of calculation by formula (4) were built the graphs of the pressure difference in the chamber of adjustable HB, which are shown in Fig. 9.

DOI 10.1515/ama-2015-0005

As shown in Fig. 9, increasing of fluid pressure supplied to the working chamber, leads to a decrease of pressure difference during spindle rotation in the bearing. It was found that with increasing frequency of spindle rotation n_s the pressure difference in the chamber of the bearing increases and at lower values p_{k_i} those facts are more intense.

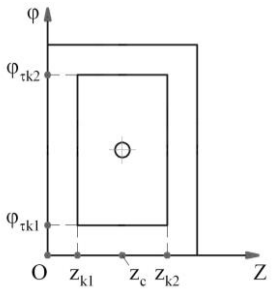

Fig. 8. Definition of a pressure difference in the i −th chamber

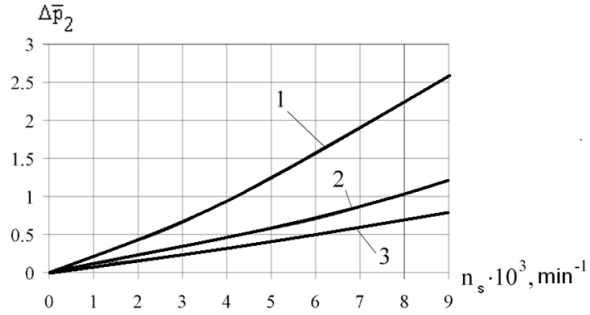

Fig. 9. Pressure difference on tangential length of the second working chamber: $1 - p_{k_2} = 1$ MPa; $2 - p_{k_2} = 2$ MPa; $3 - p_{k_2} = 3$ MPa

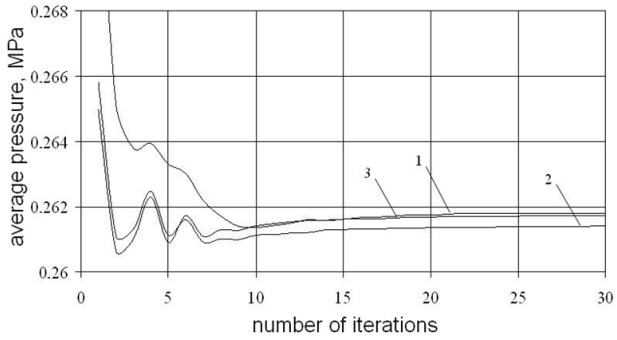

Fig. 10. Assessment of the accuracy of the calculation of the pressure function by means of CFD CosmosFloWorks: $1 - N_K = 2383$; $2 - N_K = 13192$; $3 - N_K = 20443$

The estimation of the accuracy of the calculation of the pressure function by the finite volumes can be performed by comparing the calculation results with different grids, which differ in a size and a number of cells.Solution of stationary problems inCosmos FloWorks are based on the iterative algorithms with averaging of the results of calculation time. The criterion for completion of the iterative process is the convergence of the calculation to some stable decision in time. For determination of this point, certain criteria are used: physical parameters of the system that can characterize the condition of the calculation in time. If during calculating the value of the criterion has behavior close to the stationary, a decision on the completion of the search process iterative solution of the problem is made (Fedorynenko, 2009).

In this paper, a criterion for the completion of the iterative process of the calculation is the value of the average pressure in a predetermined liquid volume. The graphs that characterize mesh convergence calculation in different sizes and quantities N_K cells are shown in Fig. 10.

The graph shows that the value of the average pressure in the calculation field matches some constant value of pressure after 20 iterations. The maximum relative difference of calculating data values of average pressure when using grids with different numbers of cells does not exceed 0.11%, indicating a satisfactory accuracy of the calculation.

4. RESULTS

As a result of simulation of output characteristics of the controlled radial HB, it has been discovered that the greatest influence on these characteristics was caused by geometric deviation bearing surfaces in the tangential direction of the bearing and bias of the spindle axis in HB.

In order to improve the bearing capacity of HB during machining processing it is necessary to raise the pressure in the chamber p_k and reduce the radial backlash in the bearing δ_0.

Changing the pressure in the chamber of HB is limited by the preservation of optimal pressure differential Δp ($\Delta p = p_H - p_k$) for maximum rigidity layer lubrication and maximum pressure of pumping unit.

So the most convenient way to increase the bearing capacity is to regulate the size of the static radial backlash δ_0, which can be used for variety of supply systems of supply in the modes as a constant flow rate ($Q = \text{const}$), and constant fluid pressure ($p = \text{const}$).

REFERENCES

1. **Alyamovskyy A.** (2005), *SolidWorks. Computer modeling in engineering practice*, BHV-Petersburg, St. Petersburg.
2. **Fedorynenko D.** (2009), Modeling Working Processes in the Controlled Hydrostatic Bearings with Means of CAD/CAE Systems, *Journal of Chernihiv State Technological University, Series "Technical science"*, 37, 91 – 98.
3. **Fedorynenko D.** (2012), The spatial function of pressure in adjustable hydrostatic bearing, *Journal of ChernihivStateTechnological University*, Chernihiv, 2 (57), 63- 70.
4. **Fedorynenko D., Sapon S., Boyko S.** (2013), Precision Spindles with Adjustable Hydrostatic Bearings, *Journal of National Technical University of Ukraine "Kyiv Polytechnic Institute"*, 3(69), 155-149.
5. **Kiogora P. R., Kinyanjui M. N., Theuri D. M.** (2014), A Conservative Scheme Model of an Inclined Pad Thrust Bearing, *International Journal of Engineering Science and Innovative Technology*, 3(01), 32-41.
6. **McDonald P. W.** (1971),*The computation of transonic flow through two-dimensional gas turbine cascades*, ASME, 71-GT-89, 12- 21.
7. **Michael F.** (2012), *Towards a Navier Stokes Exact Solution*,http://dx.doi.org/10.2139/ssrn.2193095.
8. **Reddy J. N., Gartling D. K.** (2010),*The Finite Element Method in Heat Transfer and Fluid Dynamics*, CRC Press.
9. **Sakhno Y., Fedorynenko D., Boyko S., Volyk V.** (2009), *Adjustable Hydrostatic Bearings for Spindles*, Publishing house "Aspect-polygraph", Nizhyn.
10. **Strutynsky V., Fedorynenko D.** (2011), *Statistical dynamics of spindle units for hydrostatic bearings*, LLC "Publishing" Aspect-Polygraph", Nizhin.

ON THE CONVERGENCE OF DOMAIN DECOMPOSITION ALGORITHM FOR THE BODY WITH THIN INCLUSION

Andriy STYAHAR*, Yarema SAVULA*

*Faculty of Applied Mathematics and Informatics, Department of Applied Mathematics,
Ivan Franko Lviv National University, Universytetska,1, 79000, Lviv, Ukraine

astyahar@gmail.com, savula@franko.lviv.ua

Abstract: We consider a coupled 3D model that involves computation of the stress-strain state for the body with thin inclusion. For the description of the stress-strain state of the main part, the linear elasticity theory is used. The inclusion is modelled using Timoshenko theory for shells. Therefore, the dimension of the problem inside the inclusion is decreased by one. For the numerical solution of this problem we propose an iterative domain decomposition algorithm (Dirichlet-Neumann scheme). This approach allows us to decouple problems in both parts and preserve the structure of the corresponding matrices. We investigate the convergence of the aforementioned algorithm and prove that the problem is well-posed.

Key words: Elasticity Theory, Timoshenko Shell Theory, Steklov-Poincare Operator, Domain Decomposition

1. INTRODUCTION

A lot of structures, that occur in engineering, are inhomogeneous and contain thin parts and massive parts. Therefore, it is important to develop both analytical methods and numerical algorithms for the analysis of the stress-strain state of such structures.

Different aspects of such problems were discussed in Dyyak et al. (2012); Niemi et al. (2010); Savula et al. (2000); Vynnytska and Savula (2008); Nazarov (2005) (in Vynnytska and Savula (2008) the case of the bodies with thin inclusions is considered; in Dyyak et al. (2012) the bodies with thin covers are considered; in Nazarov (2005) asymptotic methods are used for the analysis of the elastic bodies with thin rods). Papers Niemi et al. (2010) and Savula et al. (2000) are devoted to the numerical solution of the Girkmann problem. The discussion on the problems of thermoelasticity the reader may find in Sulym (2007).

In this article, we consider a model for the description of the stress-strain state for the 3D body with thin inclusion. The main part of the body is modelled using the linear elasticity theory. The thin part is modelled using the Timoshenko theory for shells. In order to numerically solve this problem, we propose an iterative domain decomposition algorithm which connects solutions in both parts using coupling conditions. We prove the convergence of the proposed algorithm and the existence and uniqueness of the solution of the corresponding Steklov-Poincare interface equation.

The application of domain decomposition method allows us to decouple problems in both parts and solve the problems independently in each part. As a result, it is possible to compute the stress-strain state accurately even for small shell thicknesses without having problems with stability issues of the coupled problem.

2. PROBLEM STATEMENT

Let us consider a problem of a stress-strain state of an elastic body Ω_1 with the inclusion in Ω_2 (Fig. 1).

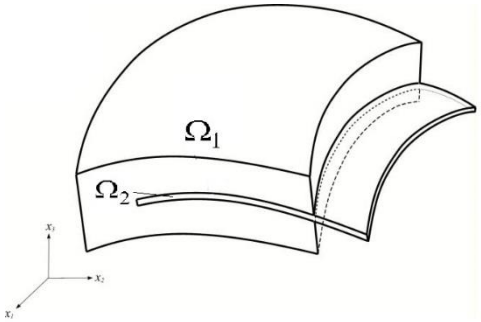

Fig. 1. Body with inclusion

Let us describe the stress-strain state of the body in Ω_1 in rectangular coordinate system x_1, x_2, x_3 using the theory of linear elasticity. Let us denote by $\Sigma = \left(\sigma_{ij}\right)_{i,j=1}^{3}$ the Cauchy stress tensor. The components of Σ are found from the relationships

$$\sigma_{ij} = \frac{1}{2}E_1\left(\frac{\partial u_i}{\partial x_j} + \frac{\partial u_j}{\partial x_i}\right),\ i,j = 1,2,3,$$

where: E_1 is the Young's modulus of the body in Ω_1; $\mathrm{u(x)} = \left(u_1(x), u_2(x), u_3(x)\right)$ is the displacement vector with u_i being the displacements along the directions of x_i, $i = 1,2,3$.

Equilibrium equations for the body in Ω_1 have the form:

$$\begin{aligned}
&\frac{\partial \sigma_{11}}{\partial x_1} + \frac{\partial \sigma_{12}}{\partial x_2} + \frac{\partial \sigma_{13}}{\partial x_3} = f_1,\\
&\frac{\partial \sigma_{21}}{\partial x_1} + \frac{\partial \sigma_{22}}{\partial x_2} + \frac{\partial \sigma_{23}}{\partial x_3} = f_2,\\
&\frac{\partial \sigma_{31}}{\partial x_1} + \frac{\partial \sigma_{32}}{\partial x_2} + \frac{\partial \sigma_{33}}{\partial x_3} = f_3,
\end{aligned} \tag{1}$$

where: $\mathrm{x} \in \Omega_1$, $\mathrm{f} = (f_1, f_2, f_3)$ is the vector of volume forces.

In the following we assume that no volume forces act on the body in Ω_1.

Let us denote by $\mathrm{n} = (n^1,\ n^2,\ n^3)$ outer normal vector and by $\tau_1 = (\tau_1^1,\ \tau_1^2,\ \tau_1^3)$, $\tau_2 = (\tau_2^1,\ \tau_2^2,\ \tau_2^3)$ corresponding tangent vectors.

DOI 10.1515/ama-2015-0006

Equations (1) are supplemented by the boundary conditions of one of the following types.

Kinematic (Dirichlet) boundary conditions are of the form:

$$u_n = u_n^0, u_{\tau_1} = u_{\tau_1}^0, u_{\tau_2} = u_{\tau_2}^0, \mathrm{x} \in \Gamma_1, \quad (2)$$

where: Γ_1 is the outer boundary of Ω_1; u_n, u_{τ_1} and u_{τ_2} are the components of the displacement vector in the coordinate system $\mathrm{n}, \tau_1, \tau_2$; u_n^0, $u_{\tau_1}^0$ and $u_{\tau_2}^0$ are the prescribed displacements on Γ_1.

Static (Neumann) boundary conditions have the form:

$$\sigma_{nn} = \sigma_{nn}^0, \sigma_{n\tau_1} = \sigma_{n\tau_1}^0, \sigma_{n\tau_2} = \sigma_{n\tau_2}^0, \mathrm{x} \in \Gamma_1, \quad (3)$$

where: σ_{nn}, $\sigma_{n\tau_1}$ and $\sigma_{n\tau_2}$ are the components of the stress tensor in the coordinate system; $\mathrm{n}, \tau_1, \tau_2$; σ_{nn}^0, $\sigma_{n\tau_1}^0$ and $\sigma_{n\tau_2}^0$ are the prescribed stresses on Γ_1.

It is possible to consider other types of boundary conditions, for example mixed boundary conditions, that combine boundary conditions (2) and (3).

For the description of the stress-strain state of the inclusion Ω_2 we use the equations of Timoshenko shell theory in the curvilinear coordinate system (ξ_1, ξ_2, ξ_3) that hold on the median surface Ω_2^*, where: $\Omega_2 = \left\{(\xi_1, \xi_2, \xi_3): \xi_1^b \le \xi_1 \le \xi_1^e, \xi_2^b \le \xi_2 \le \xi_2^e, -\frac{h}{2} \le \xi_3 \le \frac{h}{2}\right\}$, h is the thickness of the inclusion in Ω_2.

By Ω_2^* we denote the median surface of Ω_2 (the projection of Ω_2 on the surface for which $\xi_3 = 0$).

The equations of Timoshenko shell theory are of the form (Pelekh, 1978):

$$\frac{1}{A_1A_2}\frac{\partial(A_2T_{11})}{\partial\xi_1} - \frac{1}{A_1A_2}\frac{\partial A_2}{\partial\xi_1}T_{22} + \frac{1}{A_1^2A_2}\frac{\partial(A_1^2T_{12})}{\partial\xi_2} +$$
$$+k_1T_{13} + \frac{1}{A_1A_2}\frac{\partial\left(\frac{A_1}{r_1}M_{11}\right)}{\partial\xi_2} + \frac{k_2}{A_1A_2}\frac{\partial A_1}{\partial\xi_2}M_{12} =$$
$$= -(p_1^+ + p_1^-),$$
$$-\frac{1}{A_1A_2}\frac{\partial A_1}{\partial\xi_2}T_{11} + \frac{1}{A_1A_2}\frac{\partial(A_1T_{22})}{\partial\xi_2} + \frac{1}{A_1A_2^2}\frac{\partial(A_2^2T_{12})}{\partial\xi_1} +$$
$$+k_2T_{23} + \frac{1}{A_1A_2}\frac{\partial\left(\frac{A_2}{r_2}M_{22}\right)}{\partial\xi_2} + \frac{k_1}{A_1A_2}\frac{\partial A_2}{\partial\xi_1}M_{12} =$$
$$= -(p_2^+ + p_2^-),$$
$$-k_1T_{11} - k_2T_{22} + \frac{1}{A_1A_2}\frac{\partial(A_2T_{13})}{\partial\xi_1} + \frac{1}{A_1A_2}\frac{\partial(A_1T_{23})}{\partial\xi_2} =$$
$$= -(p_3^+ - p_3^-),$$
$$-T_{13} + \frac{1}{A_1A_2}\frac{\partial(A_2M_{11})}{\partial\xi_1} - \frac{1}{A_1A_2}\frac{\partial A_2}{\partial\xi_1}M_{22} +$$
$$+\frac{1}{A_1^2A_2}\frac{\partial(A_1^2M_{12})}{\partial\xi_2} = -\frac{h}{2}(p_1^+ - p_1^-),$$
$$-T_{23} - \frac{1}{A_1A_2}\frac{\partial A_1}{\partial\xi_2}M_{11} + \frac{1}{A_1A_2}\frac{\partial(A_1M_{22})}{\partial\xi_2} +$$
$$+\frac{1}{A_1A_2^2}\frac{\partial(A_2^2M_{12})}{\partial\xi_1} = -\frac{h}{2}(p_2^+ - p_2^-),$$

where: $T_{11}, T_{12}, T_{22}, T_{13}, T_{23}, M_{11}, M_{12}, M_{22}$ are the forces and momenta in the shell; $A_1 = A_1(\xi_1, \xi_2)$, $A_2 = A_2(\xi_1, \xi_2)$, $k_1 = k_1(\xi_1, \xi_2)$, $k_2 = k_2(\xi_1, \xi_2)$ correspond to Lame parameters and median surface curvature parameters; $r_1 = \frac{1}{k_1}$, $r_2 = \frac{1}{k_2}$; $(\xi_1, \xi_2) \in \Omega_2^*$; p_1^+, p_1^-, p_2^+, p_2^-, p_3^+, p_3^- are given functions; it holds:

$$T_{\alpha\alpha} = \frac{E_2h}{(1-\vartheta_2^2)}\left(\varepsilon_{\alpha\alpha} + \vartheta_2\varepsilon_{\beta\beta}\right);\ T_{12} = \frac{E_2h}{2(1+\vartheta_2)}\varepsilon_{12}$$
$$T_{\alpha3} = k'G'h\varepsilon_{\alpha3};$$
$$M_{\alpha\alpha} = \frac{E_2h^3}{12(1-\vartheta_2^2)}\left(\chi_{\alpha\alpha} + \vartheta_2\chi_{\beta\beta}\right);\ M_{12} = \frac{E_2h^3}{12(1+\vartheta_2)}\chi_{12}$$

where: $\alpha, \beta = 1,2$, $\alpha \ne \beta$; k', G' are constants that characterize transversely isotropic material; E_2 is the Young's modulus of the shell, ϑ_2 is the Poisson's ratio.

The strains ε_{11}, ε_{22}, ε_{12}, ε_{13}, ε_{23}, χ_{11}, χ_{22}, χ_{12} are obtained from the relationships:

$$\varepsilon_{\alpha\alpha} = \frac{1}{A_\alpha}\frac{\partial \mathrm{v}_\alpha}{\partial\xi_\alpha} + \frac{1}{A_\alpha A_\beta}\mathrm{v}_\beta\frac{\partial \mathrm{A}_\alpha}{\partial\xi_\beta} + k_\alpha w,$$
$$2\varepsilon_{\alpha\beta} = \frac{A_\alpha}{A_\beta}\frac{\partial\frac{\mathrm{v}_\alpha}{A_\alpha}}{\partial\xi_\beta} + \frac{A_\beta}{A_\alpha}\frac{\partial\frac{\mathrm{v}_\beta}{A_\beta}}{\partial\xi_\alpha};\ \varepsilon_{\alpha3} = -k_\alpha\mathrm{v}_\alpha + \frac{1}{A_\alpha}\frac{\partial w}{\partial\xi_\alpha} + \gamma_\alpha$$
$$\chi_{\alpha\alpha} = \frac{1}{A_\alpha}\frac{\partial\gamma_\alpha}{\partial\xi_\alpha} + \frac{1}{A_\alpha A_\beta}\gamma_\beta\frac{\partial \mathrm{A}_\alpha}{\partial\xi_\beta}$$
$$2\chi_{\alpha\beta} = \frac{k_\alpha}{A_\beta}\frac{\partial \mathrm{v}_\alpha}{\partial\xi_\beta} - \frac{k_\beta}{A_\alpha A_\beta}\mathrm{v}_\alpha\frac{\partial A_\alpha}{\partial\xi_\beta} + \frac{k_\beta}{A_\alpha}\frac{\partial \mathrm{v}_\beta}{\partial\xi_\alpha} -$$
$$-\frac{k_\alpha}{A_\alpha A_\beta}\mathrm{v}_\beta\frac{\partial A_\beta}{\partial\xi_\alpha} + \frac{A_\alpha}{A_\beta}\frac{\partial\frac{\gamma_\alpha}{A_\alpha}}{\partial\xi_\beta} + \frac{A_\beta}{A_\alpha}\frac{\partial\frac{\gamma_\beta}{A_\beta}}{\partial\xi_\alpha}$$

where: $\alpha, \beta = 1,2$, $\alpha \ne \beta$; $\mathrm{v}_1 = \mathrm{v}_1(\xi_1, \xi_2)$, $\mathrm{v}_2 = \mathrm{v}_2(\xi_1, \xi_2)$, $w = w(\xi_1, \xi_2)$, $\gamma_1 = \gamma_1(\xi_1, \xi_2)$, $\gamma_2 = \gamma_2(\xi_1, \xi_2)$ are the displacements and angles of revolution in the shell;

$$p_i^+ = \left(1 + k_1\frac{h}{2}\right)\left(1 + k_2\frac{h}{2}\right)\sigma_{i3}^+,$$
$$p_i^- = \left(1 - k_1\frac{h}{2}\right)\left(1 - k_2\frac{h}{2}\right)\sigma_{i3}^-, i = 1,2,3.$$

Here σ_{i3}^+, σ_{i3}^-, $i = 1,2,3$ are the components of the stress tensor on the top ($\xi_3 = \frac{h}{2}$) and bottom ($\xi_3 = -\frac{h}{2}$) surfaces of the shell. It is known that in the case of isotropic bodies we have $k' = \frac{5}{6}$, $G' = \frac{E_2}{2(1+\vartheta_2)}$.

On the outer edge of the thin part we impose boundary conditions either on the displacements v_1, v_2, w and angles γ_1, γ_2 or on the forces $T_{11}, T_{22}, T_{13}, T_{23}$ and momenta M_{11}, M_{22} in the shell (depending if the corresponding parts of the boundary are subjected to load or free). At the outer surface of the shell we prescribe to σ_{i3}^+ and σ_{i3}^-, $i = 1,2,3$ some given stresses.

The operator form of the equations of Timoshenko shell theory is:

$$\mathrm{Ly} = \mathrm{g}, \quad (4)$$

with:

$$\mathrm{g} = A_1A_2(g_1, g_2, g_3, g_4, g_5)^T$$
$$g_1 = p_1^+ + p_1^-;\ g_2 = p_2^+ + p_2^-;\ g_3 = p_3^+ - p_3^-;$$
$$g_4 = \frac{h}{2}(p_1^+ - p_1^-);\ g_5 = \frac{h}{2}(p_2^+ - p_2^-)$$
$$\mathrm{y} = (\mathrm{v}_1, \mathrm{v}_2, w, \gamma_1, \gamma_2)^T, \mathrm{Ly} = (l_1, l_2, l_3, l_4, l_5)^T$$
$$l_1 = -\frac{\partial(A_2T_{11})}{\partial\xi_1} + \frac{\partial A_2}{\partial\xi_1}T_{22} - \frac{1}{A_1}\frac{\partial(A_1^2T_{12})}{\partial\xi_2} -$$
$$-A_1A_2k_1T_{13} - \frac{\partial\left(\frac{A_1}{r_1}M_{11}\right)}{\partial\xi_2} - k_2\frac{\partial A_1}{\partial\xi_2}M_{12}$$

$$l_2 = \frac{\partial A_1}{\partial \xi_2} T_{11} - \frac{\partial (A_1 T_{22})}{\partial \xi_2} - \frac{1}{A_2} \frac{\partial (A_2^2 T_{12})}{\partial \xi_1} -$$

$$- A_1 A_2 k_2 T_{23} - \frac{\partial \left(\frac{A_2}{r_2} M_{22} \right)}{\partial \xi_2} - k_1 \frac{\partial A_2}{\partial \xi_1} M_{12}$$

$$l_3 = A_1 A_2 k_1 T_{11} + A_1 A_2 k_2 T_{22} - \frac{\partial (A_2 T_{13})}{\partial \xi_1} - \frac{\partial (A_1 T_{23})}{\partial \xi_2}$$

$$l_4 = A_1 A_2 T_{13} - \frac{\partial (A_2 M_{11})}{\partial \xi_1} + \frac{\partial A_2}{\partial \xi_1} M_{22} - \frac{1}{A_1} \frac{\partial (A_1^2 M_{12})}{\partial \xi_2}$$

$$l_5 = A_1 A_2 T_{23} + \frac{\partial A_1}{\partial \xi_2} M_{11} - \frac{\partial (A_1 M_{22})}{\partial \xi_2} - \frac{1}{A_2} \frac{\partial (A_2^2 M_{12})}{\partial \xi_1}$$

Let us write down the weak formulation of the Timoshenko shell theory problem. Without loss of generality we assume homogeneous boundary conditions. Let us define the following function spaces: $V = \{v \in H^1(\Omega_2^*): v = 0,\ \xi = (\xi_1, \xi_2, \xi_3) \in \Gamma_{2D}\}$, $V_1 = V^5$, where Γ_{2D} is the part of the outer boundary of Ω_2 on which the kinematic boundary condition is prescribed.

The weak formulation of the problem (4) has the form:
find $\mathrm{y} \in V_1$, such that:

$$a(\mathrm{y}, \mathrm{v}) = g(\mathrm{v}),\ \forall \mathrm{v} \in V_1, \tag{5}$$

where: $a(\mathrm{y}, \mathrm{v}) = (\mathrm{Ly}, \mathrm{v})$, $g(\mathrm{v}) = (\mathrm{g}, \mathrm{v})$.

Lemma. Assume that for the problem (4) there exist positive constants $r_{10}, r_{20}, A_{10}, A_{20}$ such that:
1. $|r_1| \geq r_{10} > 0; |r_2| \geq r_{20} > 0;$
2. $|A_1| \geq A_{10} > 0; |A_2| \geq A_{20} > 0$

almost everywhere in Ω_2^*.

Then the bilinear form $a(\mathrm{y}, \mathrm{v})$ for the problem (5) of Timoshenko shell theory is continuous.

Proof. Firstly, we remark that from the assumption 1) it follows that $|k_1| \leq k_{10} < \infty$, $|k_2| \leq k_{20} < \infty$. Moreover, the assumptions of the lemma do not restrict the class of the problems or the algorithm that can be used for the numerical solution of this problem. Indeed, for the points, for which the assumptions do not hold, the system becomes singular and can no longer be used for the adequate description of the physical process that is being modeled.

The continuity of the bilinear form follows from the fact, that all the coefficients in the system (4) are bounded by modulus almost everywhere, and that the system (4) itself is linear.

The proof also uses the obvious inequality:

$ab \leq \frac{a^2+b^2}{2}$ for $a, b \in R$.

In order to couple the models in both parts, adequate boundary conditions need to be specified. Let us denote by Ω_{2in} part of the inclusion that lies inside the body Ω_1 and by Ω_{2in}^* part of the median surface Ω_2^* which is the projection of Ω_{2in} on the surface $\xi_3 = 0$.

Let Γ_I be a boundary, common to both Ω_1 and Ω_2. Let us divide Γ_I into the following parts:

$$\Gamma_{I_1} = \left\{ \xi = (\xi_1, \xi_2, \xi_3): (\xi_1, \xi_2) \in \Omega_{2in}^*;\ \xi_3 = -\frac{h}{2} \right\}$$

$$\Gamma_{I_2} = \begin{Bmatrix} \xi = (\xi_1, \xi_2, \xi_3): (\xi_1, \xi_2) \in \Omega_{2in}^*; \\ \xi_1 = \xi_1^b;\ -\frac{h}{2} \leq \xi_3 \leq \frac{h}{2} \end{Bmatrix}$$

$$\Gamma_{I_3} = \begin{Bmatrix} \xi = (\xi_1, \xi_2, \xi_3): (\xi_1, \xi_2) \in \Omega_{2in}^*; \\ \xi_2 = \xi_2^b;\ -\frac{h}{2} \leq \xi_3 \leq \frac{h}{2} \end{Bmatrix}$$

$$\Gamma_{I_4} = \left\{ \xi = (\xi_1, \xi_2, \xi_3): (\xi_1, \xi_2) \in \Omega_{2in}^*;\ \xi_3 = \frac{h}{2} \right\}$$

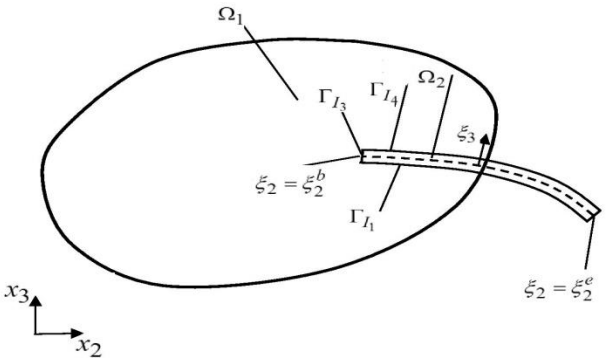

Fig. 2. Cross-section of the body in Ω by the plane $x_1 = \mathrm{const}$.

Fig. 2 shows the cross-section of the body in Ω by the plane $x_1 = \mathrm{const}$ and the connection between rectangular x_1, x_2, x_3 and curvilinear ξ_1, ξ_2, ξ_3 coordinate systems.

On each part of Γ_I the following coupling conditions are prescribed (Pelekh, 1978):

– on Γ_{I_1} (inner part of bottom surface of Ω_2):

$$u_n = w, u_{\tau_1} = -\mathrm{v}_1 + \frac{h}{2}\gamma_1, u_{\tau_2} = -\mathrm{v}_2 + \frac{h}{2}\gamma_2,$$

$$\sigma_{nn} = -\sigma_{33}^-, \sigma_{n\tau_1} = -\sigma_{13}^-, \sigma_{n\tau_2} = -\sigma_{23}^-; \tag{6}$$

– on Γ_{I_2} (inner edge of Ω_2):

$$u_{\tau_1} = w, u_{\tau_2} = -\mathrm{v}_2 - \xi_3\gamma_2, u_n = \mathrm{v}_1 + \xi_3\gamma_1,$$

$$\int_{-\frac{h}{2}}^{\frac{h}{2}} \sigma_{nn} d\xi_3 = T_{11},\ \int_{-\frac{h}{2}}^{\frac{h}{2}} \sigma_{n\tau_1} d\xi_3 = T_{13},\ \int_{-\frac{h}{2}}^{\frac{h}{2}} \sigma_{n\tau_2} d\xi_3 = T_{12},$$

$$\int_{-\frac{h}{2}}^{\frac{h}{2}} \sigma_{nn} \xi_3 d\xi_3 = M_{11},\ \int_{-\frac{h}{2}}^{\frac{h}{2}} \sigma_{n\tau_2} \xi_3 d\xi_3 = M_{12}; \tag{7}$$

– on Γ_{I_3} (inner edge of Ω_2):

$$u_{\tau_2} = w, u_{\tau_1} = -\mathrm{v}_1 - \xi_3\gamma_1, u_n = \mathrm{v}_2 + \xi_3\gamma_2,$$

$$\int_{-\frac{h}{2}}^{\frac{h}{2}} \sigma_{nn} d\xi_3 = T_{22},\ \int_{-\frac{h}{2}}^{\frac{h}{2}} \sigma_{n\tau_2} d\xi_3 = T_{23},\ \int_{-\frac{h}{2}}^{\frac{h}{2}} \sigma_{n\tau_1} d\xi_3 = T_{12},$$

$$\int_{-\frac{h}{2}}^{\frac{h}{2}} \sigma_{nn} \xi_3 d\xi_3 = M_{22},\ \int_{-\frac{h}{2}}^{\frac{h}{2}} \sigma_{n\tau_1} \xi_3 d\xi_3 = M_{12}; \tag{8}$$

– on Γ_{I_4} (inner part of top surface surface of Ω_2):

$$u_n = -w, u_{\tau_1} = \mathrm{v}_1 + \frac{h}{2}\gamma_1, u_{\tau_2} = \mathrm{v}_2 + \frac{h}{2}\gamma_2,$$

$$\sigma_{nn} = -\sigma_{33}^+, \sigma_{n\tau_1} = \sigma_{13}^+, \sigma_{n\tau_2} = \sigma_{23}^+. \tag{9}$$

3. DOMAIN DECOMPOSITION ALGORITHM

For the numerical solution of the model domain decomposition algorithm can be used.

The approximate solutions in both domains are connected using Dirichlet-Neumann scheme (Quarteroni and Valli, 1999). Do-

DOI 10.1515/ama-2015-0006

main decomposition algorithm has the following form:

1. set an initial guess λ^0 for the unknown displacements on the interface Γ_I, set $\varepsilon > 0$;
2. for $k = 0,1,\ldots$ solve the boundary value problem in Ω_1 with the displacements equal to λ^k to obtain the approximation for the forces and momenta in Ω_2 using (6)-(9);
3. solve the corresponding problem in Ω_2 to find the displacements $u_n^k, u_{\tau_1}^k, u_{\tau_2}^k$ on Γ_I;
4. update the displacements λ^k on Γ_I:
   – on Γ_{I_1}:

$$\lambda_{11}^{k+1} = (1-\theta)\lambda_{11}^k + \theta u_n^k, \qquad \lambda_{12}^{k+1} = (1-\theta)\lambda_{12}^k + \theta u_{\tau_1}^k,$$
$$\lambda_{13}^{k+1} = (1-\theta)\lambda_{13}^k + \theta u_{\tau_2}^k;$$

   – on Γ_{I_2}:

$$\lambda_{21}^{k+1} = (1-\theta)\lambda_{21}^k + \theta \mathrm{v}_1^k, \qquad \lambda_{22}^{k+1} = (1-\theta)\lambda_{22}^k + \theta \mathrm{v}_2^k,$$
$$\lambda_{23}^{k+1} = (1-\theta)\lambda_{23}^k + \theta w^k, \qquad \lambda_{24}^{k+1} = (1-\theta)\lambda_{24}^k + \theta \gamma_1^k,$$
$$\lambda_{25}^{k+1} = (1-\theta)\lambda_{25}^k + \theta \gamma_2^k;$$

   – on Γ_{I_3}:

$$\lambda_{31}^{k+1} = (1-\theta)\lambda_{31}^k + \theta \mathrm{v}_2^k, \qquad \lambda_{32}^{k+1} = (1-\theta)\lambda_{32}^k + \theta \mathrm{v}_1^k,$$
$$\lambda_{33}^{k+1} = (1-\theta)\lambda_{33}^k + \theta w^k, \qquad \lambda_{34}^{k+1} = (1-\theta)\lambda_{34}^k + \theta \gamma_2^k,$$
$$\lambda_{35}^{k+1} = (1-\theta)\lambda_{35}^k + \theta \gamma_1^k;$$

   – on Γ_{I_4}:

$$\lambda_{41}^{k+1} = (1-\theta)\lambda_{41}^k + \theta u_n^k,$$
$$\lambda_{42}^{k+1} = (1-\theta)\lambda_{42}^k + \theta u_{\tau_1}^k,$$
$$\lambda_{43}^{k+1} = (1-\theta)\lambda_{43}^k + \theta u_{\tau_2}^k,$$

   where $\theta > 0$ is a relaxation parameter;
5. if $\left\|\lambda^{k+1} - \lambda^k\right\| \geq \varepsilon$, then go to step 2, otherwise the algorithm ends.

In the following we assume that the variational problems corresponding to the domains Ω_1, Ω_2 and Ω have unique solutions (Hsiao and Wendland, 2008; Vynnytska and Savula, 2012; Dyyak and Savula, 1997).

Let us prove the convergence of the domain decomposition algorithm and the existence and uniqueness of the solution of the corresponding Steklov-Poincare equation.

For this purpose let us introduce on the common boundary of both domains the function $\varphi \in \Lambda$, with:

$$\Lambda = \{\varphi = (\varphi_1, \varphi_2, \varphi_3, \varphi_4)\},$$
$$\varphi_1 = (\varphi_{11}, \varphi_{12}, \varphi_{13}), \varphi_{1i} \in H^1(\Gamma_{I_1}), i = 1,2,3;$$
$$\varphi_2 = (\varphi_{21}, \varphi_{22}, \varphi_{23}, \varphi_{24}, \varphi_{25}),$$
$$\varphi_{2i} = \varphi_{2i}(\xi_2) \in H^{\frac{1}{2}}(\Gamma_{I_2}), \qquad i = 1,2,3,4,5;$$
$$\varphi_3 = (\varphi_{31}, \varphi_{32}, \varphi_{33}, \varphi_{34}, \varphi_{35}),$$
$$\varphi_{3i} = \varphi_{3i}(\xi_1) \in H^{\frac{1}{2}}(\Gamma_{I_3}), \qquad i = 1,2,3,4,5;$$
$$\varphi_4 = (\varphi_{41}, \varphi_{42}, \varphi_{43}), \varphi_{4i} \in H^1(\Gamma_{I_4}), i = 1,2,3.$$

We remark, that the choice of the space Λ is motivated by the specifics of the model and is based on the regularity of the corresponding functions on each part of the interface Γ_I.

The connection between the functions φ_{ij} and the displacements on the interface is the following:

   – on Γ_{I_1}:

$$\varphi_{11} = u_n, \varphi_{12} = u_{\tau_1}, \varphi_{13} = u_{\tau_2};$$

   – on Γ_{I_2}:

$$\varphi_{21} = \mathrm{v}_1, \varphi_{22} = \mathrm{v}_2, \varphi_{23} = w, \varphi_{24} = \gamma_1, \varphi_{25} = \gamma_2;$$

   – on Γ_{I_3}:

$$\varphi_{31} = \mathrm{v}_2, \varphi_{32} = \mathrm{v}_1, \varphi_{33} = w, \varphi_{34} = \gamma_2, \varphi_{35} = \gamma_1;$$

   – on Γ_{I_4}:

$$\varphi_{41} = u_n, \varphi_{42} = u_{\tau_1}, \varphi_{43} = u_{\tau_2}.$$

Let S be a Steklov-Poincare operator for our problem and $S_i, i = 1,2$ be local Steklov-Poincare operators corresponding to the domains Ω_i. Steklov-Poincare operator for the boundary-value problem is an operator that transforms boundary conditions of one type into boundary conditions of another type. In our case, Steklov-Poincare operator transforms the displacements on the boundary into loads on the boundary.

Let us multiply interface conditions (6) by $A_1A_2\left(1 - -k_1\frac{h}{2}\right)\left(1 - k_2\frac{h}{2}\right)$; (7) and (8) – by $\frac{1}{h}$; (9) – by $A_1A_2\left(1 + +k_1\frac{h}{2}\right)\left(1 + k_2\frac{h}{2}\right)$.

The Steklov-Poincare operator can be written in the form:

$\{S\varphi, \psi\}_{\Gamma_I} = \{S_1\varphi, \psi\}_{\Gamma_I} + \{S_2\varphi, \psi\}_{\Gamma_I}$, where:

$$\begin{aligned}
&\{S_1\varphi, \psi\}_{\Gamma_I} = \\
&= \langle -A_1A_2\left(1 - k_1\tfrac{h}{2}\right)\left(1 - k_2\tfrac{h}{2}\right)\sigma_{nn}(\varphi), \psi_{11}\rangle_{\Gamma_{I_1}} + \\
&+ \langle -A_1A_2\left(1 - k_1\tfrac{h}{2}\right)\left(1 - k_2\tfrac{h}{2}\right)\sigma_{n\tau_1}(\varphi), \psi_{12}\rangle_{\Gamma_{I_1}} + \\
&+ \langle -A_1A_2\left(1 - k_1\tfrac{h}{2}\right)\left(1 - k_2\tfrac{h}{2}\right)\sigma_{n\tau_2}(\varphi), \psi_{13}\rangle_{\Gamma_{I_1}} + \\
&+ \langle -A_1A_2\left(1 + k_1\tfrac{h}{2}\right)\left(1 + k_2\tfrac{h}{2}\right)\sigma_{nn}(\varphi), \psi_{41}\rangle_{\Gamma_{I_4}} + \\
&+ \langle -A_1A_2\left(1 + k_1\tfrac{h}{2}\right)\left(1 + k_2\tfrac{h}{2}\right)\sigma_{n\tau_1}(\varphi), \psi_{42}\rangle_{\Gamma_{I_4}} + \\
&+ \langle -A_1A_2\left(1 + k_1\tfrac{h}{2}\right)\left(1 + k_2\tfrac{h}{2}\right)\sigma_{n\tau_2}(\varphi), \psi_{43}\rangle_{\Gamma_{I_4}} + \\
&+ \langle -\tfrac{1}{h}\int_{-\frac{h}{2}}^{\frac{h}{2}}\sigma_{nn}(\varphi)d\xi_3, \psi_{21}\rangle_{\Gamma_{I_2}} + \\
&+ \langle -\tfrac{1}{h}\int_{-\frac{h}{2}}^{\frac{h}{2}}\sigma_{n\tau_2}(\varphi)d\xi_3, \psi_{22}\rangle_{\Gamma_{I_2}} + \\
&+ \langle -\tfrac{1}{h}\int_{-\frac{h}{2}}^{\frac{h}{2}}\sigma_{n\tau_1}(\varphi)d\xi_3, \psi_{23}\rangle_{\Gamma_{I_2}} + \\
&+ \langle -\tfrac{1}{h}\int_{-\frac{h}{2}}^{\frac{h}{2}}\sigma_{nn}(\varphi)\xi_3 d\xi_3, \psi_{24}\rangle_{\Gamma_{I_2}} + \\
&+ \langle -\tfrac{1}{h}\int_{-\frac{h}{2}}^{\frac{h}{2}}\sigma_{n\tau_2}(\varphi)\xi_3 d\xi_3, \psi_{25}\rangle_{\Gamma_{I_2}} + \\
&+ \langle -\tfrac{1}{h}\int_{-\frac{h}{2}}^{\frac{h}{2}}\sigma_{nn}(\varphi)d\xi_3, \psi_{31}\rangle_{\Gamma_{I_3}} + \\
&+ \langle -\tfrac{1}{h}\int_{-\frac{h}{2}}^{\frac{h}{2}}\sigma_{n\tau_1}(\varphi)d\xi_3, \psi_{32}\rangle_{\Gamma_{I_3}} + \\
&+ \langle -\tfrac{1}{h}\int_{-\frac{h}{2}}^{\frac{h}{2}}\sigma_{n\tau_2}(\varphi)d\xi_3, \psi_{33}\rangle_{\Gamma_{I_3}} + \\
&+ \langle -\tfrac{1}{h}\int_{-\frac{h}{2}}^{\frac{h}{2}}\sigma_{nn}(\varphi)\xi_3 d\xi_3, \psi_{34}\rangle_{\Gamma_{I_3}} + \\
&+ \langle -\tfrac{1}{h}\int_{-\frac{h}{2}}^{\frac{h}{2}}\sigma_{n\tau_1}(\varphi)\xi_3 d\xi_3, \psi_{35}\rangle_{\Gamma_{I_3}},
\end{aligned}$$

$$\{S_2\varphi,\psi\}_{\Gamma_I} =$$

$$= \langle -A_1A_2\left(1-k_1\frac{h}{2}\right)\left(1-k_2\frac{h}{2}\right)\sigma_{33}^-,\psi_{11}\rangle_{\Gamma_{I_1}} +$$
$$+\langle -A_1A_2\left(1-k_1\frac{h}{2}\right)\left(1-k_2\frac{h}{2}\right)\sigma_{13}^-,\psi_{12}\rangle_{\Gamma_{I_1}} +$$
$$+\langle -A_1A_2\left(1-k_1\frac{h}{2}\right)\left(1-k_2\frac{h}{2}\right)\sigma_{23}^-,\psi_{13}\rangle_{\Gamma_{I_1}} +$$
$$+\langle -A_1A_2\left(1+k_1\frac{h}{2}\right)\left(1+k_2\frac{h}{2}\right)\sigma_{33}^+,\psi_{41}\rangle_{\Gamma_{I_4}} +$$
$$+\langle A_1A_2\left(1+k_1\frac{h}{2}\right)\left(1+k_2\frac{h}{2}\right)\sigma_{13}^+,\psi_{42}\rangle_{\Gamma_{I_4}} + \langle A_1A_2\left(1+\right.$$
$$\left.+k_1\frac{h}{2}\right)\left(1+k_2\frac{h}{2}\right)\sigma_{23}^+,\psi_{43}\rangle_{\Gamma_{I_4}} + \langle\frac{1}{h}T_{11},\psi_{21}\rangle_{\Gamma_{I_2}} +$$
$$+\langle\frac{1}{h}T_{12},\psi_{22}\rangle_{\Gamma_{I_2}} + \langle\frac{1}{h}T_{13},\psi_{23}\rangle_{\Gamma_{I_2}} + \langle\frac{1}{h}M_{11},\psi_{24}\rangle_{\Gamma_{I_2}} +$$
$$+\langle\frac{1}{h}M_{12},\psi_{25}\rangle_{\Gamma_{I_2}} + \langle\frac{1}{h}T_{22},\psi_{31}\rangle_{\Gamma_{I_3}} + \langle\frac{1}{h}T_{12},\psi_{32}\rangle_{\Gamma_{I_3}} +$$
$$+\langle\frac{1}{h}T_{23},\psi_{33}\rangle_{\Gamma_{I_3}} + \langle\frac{1}{h}M_{22},\psi_{34}\rangle_{\Gamma_{I_3}} + \langle\frac{1}{h}M_{12},\psi_{35}\rangle_{\Gamma_{I_3}}$$

with $\langle u,v\rangle_{\Gamma_I}$ being a bilinear form:

$$\langle u,v\rangle_{\Gamma_I} = \int_{\Gamma_I} uvd\Gamma_I,\ \forall v\in H^{1/2}(\Gamma_I),\ \forall u\in\left(H^{\frac{1}{2}}(\Gamma_I)\right)^*.$$

Let Q, Q_1, Q_2 be preconditioners of the domain decomposition algorithm for the Dirichlet-Neumann scheme (Quarteroni and Valli, 1999), where: $Q = Q_1 + Q_2$, $\{Q_1\varphi,\psi\}_{\Gamma_I} = \{S_1\varphi,\psi\}_{\Gamma_I}$, $\{Q_2\varphi,\psi\}_{\Gamma_I} = \{S_2\varphi,\psi\}_{\Gamma_I}$.

In the case of Dirichlet-Neumann scheme the preconditioners Q, Q_1 and Q_2 coincide with Stelkov-Poincare operators S, S_1 and S_2 respectively.

Let us investigate the properties of the Steklov-Poincare operators S, S_1, S_2.

The linearity and symmetry of S_2 follows directly from the linearity of the corresponding operator in Ω_2^*, median surface of Ω_2.

Theorem. Operator S_2 is continuous and positive–definite on Λ.

Proof. Let us rewrite operator S_2 in the form:

$$\{S_2\varphi,\psi\}_{\Gamma_I} =$$

$$= \int_{\Omega_2^*} A_1A_2\left(\left(1+k_1\frac{h}{2}\right)\left(1+k_2\frac{h}{2}\right)\sigma_{33}^+ - \left(1-k_1\frac{h}{2}\right)\left(1-\right.\right.$$
$$\left.\left.-k_2\frac{h}{2}\right)\sigma_{33}^-\right)\widetilde{w}d\Omega_2^* + \int_{\Omega_2^*} A_1A_2\left(\left(1+k_1\frac{h}{2}\right)\left(1+\right.\right.$$
$$\left.\left.+k_2\frac{h}{2}\right)\sigma_{13}^+ + \left(1-k_1\frac{h}{2}\right)\left(1-k_2\frac{h}{2}\right)\sigma_{13}^-\right)\tilde{v}_1d\Omega_2^* +$$
$$+\int_{\Omega_2^*} A_1A_2\frac{h}{2}\left(\left(1+k_1\frac{h}{2}\right)\left(1+k_2\frac{h}{2}\right)\sigma_{13}^+ - \left(1-k_1\frac{h}{2}\right)\left(1-\right.\right.$$
$$\left.\left.-k_2\frac{h}{2}\right)\sigma_{13}^-\right)\tilde{\gamma}_1d\Omega_2^* + \int_{\Omega_2^*} A_1A_2\left(\left(1+k_1\frac{h}{2}\right)\left(1+\right.\right.$$
$$\left.\left.+k_2\frac{h}{2}\right)\sigma_{23}^+ + \left(1-k_1\frac{h}{2}\right)\left(1-k_2\frac{h}{2}\right)\sigma_{23}^-\right)\tilde{v}_2d\Omega_2^* +$$
$$+\int_{\Omega_2^*} A_1A_2\frac{h}{2}\left(\left(1+k_1\frac{h}{2}\right)\left(1+k_2\frac{h}{2}\right)\sigma_{23}^+ - \left(1-k_1\frac{h}{2}\right)\left(1-\right.\right.$$
$$\left.\left.-k_2\frac{h}{2}\right)\sigma_{23}^-\right)\tilde{\gamma}_2d\Omega_2^* + \langle\frac{1}{h}T_{11},\tilde{v}_1\rangle_{\Gamma_{I_2}} + \langle\frac{1}{h}T_{12},\tilde{v}_2\rangle_{\Gamma_{I_2}} +$$
$$+\langle\frac{1}{h}T_{13},\widetilde{w}\rangle_{\Gamma_{I_2}} + \langle\frac{1}{h}M_{11},\tilde{\gamma}_1\rangle_{\Gamma_{I_2}} + \langle\frac{1}{h}M_{12},\tilde{\gamma}_2\rangle_{\Gamma_{I_2}} +$$
$$+\langle\frac{1}{h}T_{22},\tilde{v}_2\rangle_{\Gamma_{I_3}} + \langle\frac{1}{h}T_{12},\tilde{v}_1\rangle_{\Gamma_{I_3}} + \langle\frac{1}{h}T_{23},\widetilde{w}\rangle_{\Gamma_{I_3}} +$$
$$+\langle\frac{1}{h}M_{22},\tilde{\gamma}_2\rangle_{\Gamma_{I_3}} + \langle\frac{1}{h}M_{12},\tilde{\gamma}_1\rangle_{\Gamma_{I_3}}.$$

Let us substitute the corresponding left-hand sides from the Timoshenko shell theory model equations (4). As a result, we can prove the continuity and coercitivity of the local Steklov-Poincare operator S_2 taking into account properties of the operator (4). It is known, that the operator (4) is coercive (Vynnytska and Savula, 2008).

Therefore, we obtain:

$$\{S_2\varphi,\varphi\}_{\Gamma_I} \geq c^2\int_{\Omega_2^*}\left(\left(\frac{\partial v_1}{\partial\xi_1}\right)^2 + \left(\frac{\partial v_2}{\partial\xi_1}\right)^2 + \left(\frac{\partial w}{\partial\xi_1}\right)^2 + \left(\frac{\partial\gamma_1}{\partial\xi_1}\right)^2 +\right.$$
$$+\left(\frac{\partial\gamma_2}{\partial\xi_1}\right)^2 + \left(\frac{\partial v_1}{\partial\xi_2}\right)^2 + \left(\frac{\partial v_2}{\partial\xi_2}\right)^2 + \left(\frac{\partial w}{\partial\xi_2}\right)^2 + \left(\frac{\partial\gamma_1}{\partial\xi_2}\right)^2 + \left(\frac{\partial\gamma_2}{\partial\xi_2}\right)^2 +$$
$$\left.+v_1^2 + v_2^2 + w^2 + \gamma_1^2 + \gamma_2^2\right)d\Omega_2^*,\ c\neq 0. \qquad (10)$$

From (10) it follows that:

$$\{S_2\varphi,\varphi\}_{\Gamma_I} \geq c_1^2\int_{\Omega_2^*}\left(\left(-\frac{\partial v_1}{\partial\xi_1}+\frac{h}{2}\frac{\partial\gamma_1}{\partial\xi_1}\right)^2 + \left(-\frac{\partial v_2}{\partial\xi_1}+\right.\right.$$
$$+\frac{h}{2}\frac{\partial\gamma_2}{\partial\xi_1}\Big)^2 + \left(-\frac{\partial v_1}{\partial\xi_2}+\frac{h}{2}\frac{\partial\gamma_1}{\partial\xi_2}\right)^2 + \left(-\frac{\partial v_2}{\partial\xi_2}+\frac{h}{2}\frac{\partial\gamma_2}{\partial\xi_2}\right)^2 +$$
$$+\left(\frac{\partial w}{\partial\xi_1}\right)^2 + \left(\frac{\partial w}{\partial\xi_2}\right)^2 + \left(-v_1+\frac{h}{2}\gamma_1\right)^2 + \left(-v_2+\frac{h}{2}\gamma_2\right)^2 +$$
$$\left.+w^2\right)d\Omega_2^* + c_2^2\|\varphi_2\|^2_{H^{\frac{1}{2}}(\Gamma_{I_2})} + c_3^2\|\varphi_3\|^2_{H^{\frac{1}{2}}(\Gamma_{I_3})} +$$
$$+c_4^2\int_{\Omega_2^*}\left(\left(\frac{\partial v_1}{\partial\xi_1}+\frac{h}{2}\frac{\partial\gamma_1}{\partial\xi_1}\right)^2 + \left(\frac{\partial v_2}{\partial\xi_1}+\frac{h}{2}\frac{\partial\gamma_2}{\partial\xi_1}\right)^2 + \left(\frac{\partial v_1}{\partial\xi_2}+\right.\right.$$
$$+\frac{h}{2}\frac{\partial\gamma_1}{\partial\xi_2}\Big)^2 + \left(\frac{\partial v_2}{\partial\xi_2}+\frac{h}{2}\frac{\partial\gamma_2}{\partial\xi_2}\right)^2 + \left(\frac{\partial w}{\partial\xi_1}\right)^2 + \left(\frac{\partial w}{\partial\xi_2}\right)^2 +$$
$$+\left(v_1+\frac{h}{2}\gamma_1\right)^2 + \left(v_2+\frac{h}{2}\gamma_2\right)^2 + w^2\Big)d\Omega_2^*,$$

$c_i > 0,\ i = 1,2,3,4.$

Therefore, the operator S_2 is coercive on Λ.

Let us prove the continuity of S_2. The continuity of S_2 follows from the continuity of the operator for the problem (4) in Ω_2^*.

Using the continuity of the operator for the problem (4), we get:

$$\{S_2\varphi,\psi\}_{\Gamma_I} \leq C^2\left(\int_{\Omega_2^*}\left(\left(\frac{\partial v_1}{\partial\xi_1}\right)^2 + \left(\frac{\partial v_2}{\partial\xi_1}\right)^2 + \left(\frac{\partial w}{\partial\xi_1}\right)^2 +\right.\right.$$
$$+\left(\frac{\partial\gamma_1}{\partial\xi_1}\right)^2 + \left(\frac{\partial\gamma_2}{\partial\xi_1}\right)^2 + \left(\frac{\partial v_1}{\partial\xi_2}\right)^2 + \left(\frac{\partial v_2}{\partial\xi_2}\right)^2 + \left(\frac{\partial w}{\partial\xi_2}\right)^2 + \left(\frac{\partial\gamma_1}{\partial\xi_2}\right)^2 +$$
$$\left.\left.+\left(\frac{\partial\gamma_2}{\partial\xi_2}\right)^2 + v_1^2 + v_2^2 + w^2 + \gamma_1^2 + \gamma_2^2\right)d\Omega_2^*\right)^{1/2} \times$$
$$\times\left(\int_{\Omega_2^*}\left(\left(\frac{\partial\tilde{v}_1}{\partial\xi_1}\right)^2 + \left(\frac{\partial\tilde{v}_2}{\partial\xi_1}\right)^2 + \left(\frac{\partial\tilde{w}}{\partial\xi_1}\right)^2 + \left(\frac{\partial\tilde{\gamma}_1}{\partial\xi_1}\right)^2 + \left(\frac{\partial\tilde{\gamma}_2}{\partial\xi_1}\right)^2 +\right.\right.$$
$$+\left(\frac{\partial\tilde{v}_1}{\partial\xi_2}\right)^2 + \left(\frac{\partial\tilde{v}_2}{\partial\xi_2}\right)^2 + \left(\frac{\partial\tilde{w}}{\partial\xi_2}\right)^2 + \left(\frac{\partial\tilde{\gamma}_1}{\partial\xi_2}\right)^2 + \left(\frac{\partial\tilde{\gamma}_2}{\partial\xi_2}\right)^2 + \tilde{v}_1^2 +$$
$$\left.\left.+\tilde{v}_2^2 + \tilde{w}^2 + \tilde{\gamma}_1^2 + \tilde{\gamma}_2^2\right)d\Omega_2^*\right)^{1/2},\ C>0.$$

As a result, S_2 is continuous.

Let us consider now the local Steklov-Poincare operator S_1 and rewrite it in the form:

$$\{S_1\varphi,\psi\}_{\Gamma_I} =$$

$$= \langle -A_1A_2\left(1-k_1\frac{h}{2}\right)\left(1-k_2\frac{h}{2}\right)\sigma_{nn}(\varphi),u_n\rangle_{\Gamma_{I_1}} +$$
$$+\langle -A_1A_2\left(1-k_1\frac{h}{2}\right)\left(1-k_2\frac{h}{2}\right)\sigma_{n\tau_1}(\varphi),u_{\tau_1}\rangle_{\Gamma_{I_1}} +$$
$$+\langle -A_1A_2\left(1-k_1\frac{h}{2}\right)\left(1-k_2\frac{h}{2}\right)\sigma_{n\tau_2}(\varphi),u_{\tau_2}\rangle_{\Gamma_{I_1}} +$$
$$+\langle -A_1A_2\left(1+k_1\frac{h}{2}\right)\left(1+k_2\frac{h}{2}\right)\sigma_{nn}(\varphi),u_n\rangle_{\Gamma_{I_4}} +$$
$$+\langle -A_1A_2\left(1+k_1\frac{h}{2}\right)\left(1+k_2\frac{h}{2}\right)\sigma_{n\tau_1}(\varphi),u_{\tau_1}\rangle_{\Gamma_{I_4}} +$$
$$+\langle -A_1A_2\left(1+k_1\frac{h}{2}\right)\left(1+k_2\frac{h}{2}\right)\sigma_{n\tau_2}(\varphi),u_{\tau_2}\rangle_{\Gamma_{I_4}} +$$
$$+\langle -\frac{1}{h}\int_{-\frac{h}{2}}^{\frac{h}{2}}\sigma_{nn}(\varphi)d\xi_3,u_n\rangle_{\Gamma_{I_2}} +$$
$$+\langle\frac{1}{h}\int_{-\frac{h}{2}}^{\frac{h}{2}}\sigma_{n\tau_2}(\varphi)d\xi_3,u_{\tau_2}\rangle_{\Gamma_{I_2}} +$$

DOI 10.1515/ama-2015-0006

$$+\langle -\frac{1}{h}\int_{-\frac{h}{2}}^{\frac{h}{2}}\sigma_{n\tau_1}(\varphi)d\xi_3\,,u_{\tau_1}\rangle_{\Gamma_{I_2}}+$$
$$+\langle -\frac{1}{h}\int_{-\frac{h}{2}}^{\frac{h}{2}}\sigma_{nn}(\varphi)d\xi_3\,,u_{n}\rangle_{\Gamma_{I_3}}+$$
$$+\langle -\frac{1}{h}\int_{-\frac{h}{2}}^{\frac{h}{2}}\sigma_{n\tau_2}(\varphi)d\xi_3\,,u_{\tau_2}\rangle_{\Gamma_{I_3}}+$$
$$+\langle \frac{1}{h}\int_{-\frac{h}{2}}^{\frac{h}{2}}\sigma_{n\tau_1}(\varphi)d\xi_3\,,u_{\tau_1}\rangle_{\Gamma_{I_3}}.$$

Since the Steklov−Poincare operator for the problem of linear elasticity theory is linear, continuous and coercive on $\left(H^{\frac{1}{2}}(\Gamma_I)\right)^3$ (Hsiao and Wendland, 2008), and using the continuous and compact embedding $H^1(D)\subset\subset H^{\frac{1}{2}}(D)$ for a strong Lipschitz domain D (Hsiao and Wendland, 2008), we get that the operator S_1 is linear, continuous and positive on Λ (assuming that the corresponding tensions are prescribed as boundary conditions on each part of the interface Γ_I).

It is obvious that the Steklov-Poincare operator S is therefore linear, continuous and coercive.

As a result, the preconditioner operators Q, Q_1 and Q_2 are also linear and continuous, and the operators Q and Q_2 are coercive. Moreover, operator Q_2 is symmetric.

By Lax-Milgram lemma, the corresponding Steklov-Poincare equation has unique solution.

Let us state the theorem about the convergence of domain decomposition algorithm (Niemi et al., 2010).

Theorem: (the convergence of domain decomposition algorithm).

Let:

- operator Q_2 be continuous and coercive on a Hilbert space X;
- operator Q_1 be continuous on X;
- operator Q_2 be symmetric and operator Q be coercive on X.

Then for arbitrary $\lambda^0\in X$ iterations:

$$\lambda^{k+1}=\lambda^{k}+\theta\mathrm{Q}_2^{-1}\left(\mathrm{G}-\mathrm{Q}\lambda^{k}\right)$$

converge in X to the solution of the equation:

$$\mathrm{Q}\lambda=\mathrm{G}$$

for arbitrary θ satisfying $0<\theta<\theta_{max}$.

Therefore, we have formulated and proven the following

Theorem: Let:

- the Steklov-Poincare operator corresponding to the problem of linear elasticity (1) with corresponding boundary conditions be continuous, symmetric and coercive on the corresponding trace spaces defined in Hsiao and Wendland (2008);
- the assumptions of Lemma hold;
- $A_1, A_2, k_1, k_2\in L^2(\Omega_2^*)$.
- Then the iterative Dirichlet-Neumann scheme for the problem (1)-(4), (6)-(9) with the Dirichlet boundary conditions imposed on the outer edge of the thin part is convergent for some relaxation parameter θ where $0<\theta<\theta_{max}$.

Proof: Follows from the theorem about the convergence of domain decomposition algorithms (Dirichlet-Neumann scheme) (Quarteroni and Valli, 1999).

4. CONCLUSIONS

We propose a domain decomposition algorithm for the computation of the stress-strain state of the body with thin inclusion. Based on the fact, that the corresponding problems in both parts can be solved separately, one can efficiently solve them preserving the structure and properties of the resulting matrices in both parts. Since the inclusion is modeled using Timoshenko shell theory, the dimension of the problem in the thin part is decreased.

We prove that the corresponding Steklov-Poncare interface equation is well-posed and that the proposed algorithm converges for the appropriately chosen relaxation parameter, which gives the theoretical background for implementation of the proposed algorithm.

REFERENCES

1. **Dyyak I., Savula Ya., Styahar A.** (2012), Numerical investigation of a plain strain state for a body with thin cover using domain decomposition, *Journal of Numerical and Applied Mathematics*, 3 (109), 23–33.
2. **Dyyak I., Savula Ya.** (1997), D-Adaptive mathematical model of solid body with thin coating, *Mathematical Studies*, 7 (1), 103–109.
3. **Hsiao G.C., Wendland W.L.** (2008), *Boundary integral equations*, Springer.
4. **Nazarov S.** (2005), Asymptotic analysis and modeling of a jointing of a massive body with thin rods, *Journal of Mathematical Sciences*, 127 (5), 2192-2262.
5. **Niemi A.H., Babuska I., Pitkaranta J., Demkowicz L.** (2010), Finite element analysis of the Girkmann problem using the modern hp-version and the classical h-version, *ICES Report*, 10-47.
6. **Pelekh B.** (1978), Generalized shell theory, Lviv (in Russian).
7. **Quarteroni A., Valli. A.** (1999), Domain decomposition methods for partial differential equations, Oxford.
8. **Savula Ya., Mang H., Dyyak I., Pauk N.** (2000), Coupled boundary and finite element analysis of a special class of two-dimensional problems of the theory of elasticity, *Computers and Structures*, 75 (2), 157-165.
9. **Sulym H.** (2007), Bases of mathematical theory of thermoelastic eqiulibrium of deformable solids with thin inclusions, *Research and Publishing Center of Shevchenko Scientific Society*, Lviv (in Ukrainian).
10. **Vynnytska L., Savula Ya.** (2008), The stress-strain state of elastic body with thin inclusion, *Ph.-Math. Modeling and Information Techonogies*, 7, 21-29 (in Ukrainian).
11. **Vynnytska L., Savula Ya.** (2012), Mathematical modeling and numerical analysis of elastic body with thin inclusion, *Computational Mechanics*, 50 (5), 533-542.

SOLVING NONLINEAR THERMAL PROBLEMS OF FRICTION BY USING METHOD OF LINES

Ewa OCH*

*Faculty of Mechanical Engineering, Bialystok University of Technology, 45C Wiejska Street, Bialystok, 15-351, Poland

e.och@doktoranci.pb.edu.pl

Abstract: One-dimensional heat conduction problem of friction for two bodies (half spaces) made of thermosensitive materials was considered. Solution to the nonlinear boundary-value heat conduction problem was obtained in three stages. At the first stage a partial linearization of the problem was performed by using Kirchhoff transform. Next, the obtained boundary-values problem by using the method of lines was brought to a system of nonlinear ordinary differential equations, relatively to Kirchhoff's function values in the nodes of the grid on the spatial variable, where time is an independent variable. At the third stage, by using the Adams's method from DIFSUB package, a numerical solution was found to the above-mentioned differential equations. A comparative analysis was conducted (Och, 2014) using the results obtained with the proposed method and the method of successive approximations.

Key words: Method Of Lines, Thermal Problems Of Friction, Thermosensitive Materials

1. INTRODUCTION

Almost all elements of machine that work together are accompanied by the friction processes. Influenced by the friction forces, on the contact surfaces of the body, the heat is generated, which - as the heat fluxes – penetrates the elements of the system and heats them up. The temperature increase may lead to changes in physical and chemical properties of friction materials, friction coefficients and termomechanical wear, etc. (Chichinadze et al., 1979; Rhee et al., 1991; Kalin, 2004).

One of the methods to estimate the distribution of transient temperature fields in elements of heavily loaded nodes of friction is the use of analytical models, where the real friction elements (pad, disk) are replaced by half-limited (half space) or limited (layer) bodies (Nosko et al., 2009; Kuciej, 2012; Yevtushenko and Kuciej, 2012). Most of the models were developed basing on the solution to linear boundary-values problems of heat conduction, where changes in sliding velocity and pressure with time; inhomogeneity of friction materials; or different types of boundary conditions on the friction surface and on the free surfaces of elements were all taken into account (Sazonov, 2008; Belyakov and Nosko, 2010; Yevtushenko et al., 2013). But at the same time, the above solutions do not take into account the changes (caused by the increase of temperature) in coefficients of friction and wear, and thermal properties of materials.

Dependency of coefficients of friction and wear on the temperature were considered when the one-dimensional nonlinear frictional heating models were developed in articles (Olesiak et al., 1997; Evtushenko and Pir'ev, 1999) and monographs (Pyr'yev, 2004; Awrejcewicz and Pyr'yev, 2009).

Models that take into account the change of the thermal-physical properties of friction materials along with increasing temperature were proposed for the materials with a so-called simple thermal nonlinearity in articles (Och, 2013, Yevtushenko et al., 2014a, b), and for the materials with an arbitrary nonlinearity - in articles (Och, 2014; Yevtushenko et al., 2014c, 2015). Solutions to the respective thermal problems of friction were obtained by using the iterative methods (Kushnir, Popowych, 2011).

The main purpose of this paper is to show the effectiveness of the methods of lines in solving nonlinear boundary-value problems of heat conduction, with the heat generation due to friction taken into account.

2. STATEMENT OF THE PROBLEM

Let two thermally sensitive half spaces be pressed at infinity by constant pressure p_0 along the axis z (Fig. 1). At the time $l = 0$, taken as the initial, bodies begin to slide relatively to each other at a constant speed V_0 in the direction of the y axis in accordance with a Cartesian coordinate system $Oxyz$. The initial temperature of the bodies is the same and equal to T_0. On the contact surface, under the influence of friction forces, the heat is generated, which in the form of heat fluxes penetrates each bodies in such a way that their sum is equal to the specific power of friction $q_0 = fV_0p_0$ (Yevtushenko and Kuciej, 2012). Thermal contact of considered bodies is imperfect, i.e. through the friction surface the heat flow takes place at a constant value of the thermal conductivity of contact coefficient. We assume the Podstrigach's condition of imperfect thermal contact, which take into account the thermal resistance of a thin layer between bodies at friction (Podstrigach, 1963). Reviews of researches into imperfect frictional thermal contact are given in the papers (Nosko et al., 2009, Belyakov and Nosko, 2010; Kuciej, 2012).

Further, all values referring to the upper and lower half spaces will respectively have subscripts 1 and 2.

We assume that the coefficients of thermal conductivity K_l and heat capacity c_l of the bodies material depend on the temperature K_l, $l = 1,2$:

$$K_l(T_l) = K_{l,0}\, K_l^*(T_l),\ \ K_{l,0} \equiv K_l(T_0),$$
$$c_l(T_l) = c_{l,0}\, c_l^*(T), c_{l,0} \equiv c_l(T_0), \tag{1}$$

and their density ρ_l, $l = 1, 2$ is constant.

DOI 10.1515/ama-2015-0007

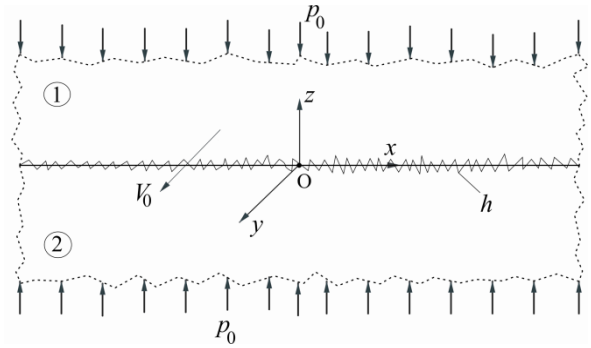

Fig. 1. The scheme of frictional heating

Taking into account the above-mentioned assumptions, in order to find the temperature of the sliding bodies, we have the following nonlinear boundary-values heat conduction problem (Och, 2014):

$$\frac{\partial^2 T_1^*}{\partial \zeta^2} = \frac{1}{k_0^* k_1^*(T_1^*)} \frac{\partial T_1^*}{\partial \tau}, \ \zeta > 0, \ \tau > 0 \tag{2}$$

$$\frac{\partial^2 T_2^*}{\partial \zeta^2} = \frac{1}{k_2^*(T_2^*)} \frac{\partial T_2^*}{\partial \tau}, \ \zeta < 0, \ \tau > 0 \tag{3}$$

$$K_2^*(T_2^*) \frac{\partial T_2^*}{\partial \zeta}\bigg|_{\zeta=0^-} - K_0^* \ K_1^*(T_1^*) \frac{\partial T_1^*}{\partial \zeta}\bigg|_{\zeta=0^+} = 1, \ \tau > 0 \tag{4}$$

$$K_2^*(T_2^*) \frac{\partial T_2^*}{\partial \zeta}\bigg|_{\zeta=0^-} + K_0^* \ K_1^*(T_1^*) \frac{\partial T_1^*}{\partial \zeta}\bigg|_{\zeta=0^+} = Bi \ [T_1^*(0^+, \tau) - T_2^*(0^-, \tau)], \ \tau > 0 \tag{5}$$

$$T_l^*(\zeta, \tau) \to T_0^*, \ |\zeta| \to \infty, \ l = 1,2 \tag{6}$$

$$T_l(\zeta, 0) = T_0^*, \ |\zeta| < \infty, \ l = 1,2 \tag{7}$$

where:

$$\zeta = \frac{z}{a}, \ \tau = \frac{k_{2,0} t}{a^2}, \ K_0^* = \frac{K_{1,0}}{K_{2,0}}, \ k_0^* = K_0^* \frac{\rho_2 c_{2,0}}{\rho_1 c_{1,0}} \tag{8}$$

$$Bi = \frac{h\, a}{K_{2,0}}, T_a = \frac{q_0 a}{K_{2,0}}, T_0^* = \frac{T_0}{T_a}, T_l^* = \frac{T_l}{T_a} \tag{9}$$

$$k_l^*(T_l^*) = \frac{K_l^*(T_l^*)}{c_l^*(T_l^*)}, l = 1,2 \tag{10}$$

where: α – is the effective depth of the heat penetration (Chichinadze et al., 1979).

3. KIRCHHOFF TRANSFORMATION

We introduce the Kirchhoff's functions $\Theta_l(\zeta, \tau)$ (Kirchhoff, 1894):

$$\Theta_l(\zeta, \tau) = \int_{T_0^*}^{T^*} K_l^*(T_l^*) \, dT_l^*, \ l = 1,2 \tag{11}$$

As a result, we obtained a partially linearized boundary-value problems in relation to the functions $\Theta_l \ (\zeta, \tau)$:

$$\frac{\partial^2 \Theta_1}{\partial \zeta^2} = \frac{1}{k_0^* \, k_1^*(T_1^*)} \frac{\partial \Theta_1}{\partial \tau}, \zeta > 0, \ \tau > 0 \tag{12}$$

$$\frac{\partial^2 \Theta_2}{\partial \zeta^2} = \frac{1}{k_2^*(T_2^*)} \frac{\partial \Theta_2}{\partial \tau}, \zeta < 0, \ \tau > 0 \tag{13}$$

$$\frac{\partial \Theta_2}{\partial \zeta}\bigg|_{\zeta=0} - K_0^* \frac{\partial \Theta_1}{\partial \zeta}\bigg|_{\zeta=0} = 1, \tau > 0 \tag{14}$$

$$\frac{\partial \Theta_2}{\partial \zeta}\bigg|_{\zeta=0} + K_0^* \frac{\partial \Theta_1}{\partial \zeta}\bigg|_{\zeta=0} = \ Bi \ [T_1^*(0, \tau) - T_2^*(0, \tau)], \tau > 0 \tag{15}$$

$$\Theta_l^{(i)}(\zeta, \tau) \to 0, \ |\zeta| \to \infty, \ \tau \geq 0, \ l = 1,2 \tag{16}$$

$$\Theta_l^{(i)}(\zeta, 0) = 0, \ |\zeta| < \infty, \ l = 1,2 \tag{17}$$

where:

$$k_l^*(T^*) = K_l^*(T^*)/c_l^*(T^*), l = 1,2 \tag{18}$$

Solution to partially linearized boundary-values problem (12)–(17) we obtain by using the methods of lines (Hall, Watt, 1976).

4. METHOD OF LINES

We choose layer in each half spaces $0 \leq |\zeta| \leq \delta_l$, $l = 1,2$ in such a way that $|\zeta| = \delta_l$ boundary condition can be fulfilled (16). Let us divide compartments $[0, \delta_l]$, $l = 1,2$ into $n_l \in N$ parts with the points:

$$\zeta_{l,j} = (-1)^{l+1} j \Delta\zeta_l, \Delta\zeta_l = \delta_l / n_l, j = 0,1, \ldots, n_l, l = 1,2 \tag{19}$$

On the grid (19) we introduce central finite-difference approximations of partial derivatives (Ozisik, 2000):

$$\frac{\partial \theta_l(\zeta,\tau)}{\partial \zeta} \approx \frac{\theta_{l,j+1}(\tau) - \theta_{l,j-1}(\tau)}{2\Delta\zeta_l} \tag{20}$$

$$\frac{\partial^2 \theta_l(\zeta,\tau)}{\partial \zeta^2} \approx \frac{\theta_{l,j+1}(\tau) - 2\theta_{l,j}(\tau) + \theta_{l,j-1}(\tau)}{(\Delta\zeta_l)^2} \tag{21}$$

where: $\Theta_{l,j}(\tau) \equiv \Theta_{l,j}(\zeta_{l,j}\tau), \tau \geq 0, j = 0,1, \ldots, n_l, l = 1,2.$

Taking into account the formulas (19)–(21), the boundary-value problem (12)–(17) can be written in the form:

$$\frac{\theta_{1,j+1}(\tau) - 2\theta_{1,j}(\tau) + \theta_{1,j-1}(\tau)}{(\Delta\zeta_1)^2} = \frac{1}{k_0^* \, k_{1,j}^*(\tau)} \frac{d\theta_{1,j}(\tau)}{d\tau}, \quad j = 0,1, \ldots, n_1, \tag{22}$$

$$\frac{\theta_{2,j+1}(\tau) - 2\theta_{2,j}(\tau) + \theta_{2,j-1}(\tau)}{(\Delta\zeta_2)^2} = \frac{1}{k_{2,j}^*(\tau)} \frac{d\theta_{2,j}(\tau)}{d\tau}, \quad j = 0,1, \ldots, n_2, \tag{23}$$

$$\frac{\theta_{2,1}(\tau) - \theta_{2,-1}(\tau)}{2\Delta\zeta_2} - K_0^* \frac{\theta_{1,1}(\tau) - \theta_{1,-1}(\tau)}{2\Delta\zeta_1} = 1 \tag{24}$$

$$\frac{\Theta_{2,1}(\tau) - \Theta_{2,-1}(\tau)}{2\Delta\zeta_2} + K_0^* \frac{\Theta_{1,1}(\tau) - \Theta_{1,-1}(\tau)}{2\Delta\zeta_1} = Bi \ [T_{1,0}^*(\tau) - T_{2,0}^*(\tau)] \tag{25}$$

$$\theta_{l,n_l+1}(\tau) - \theta_{l,n_l-1}(\tau) = 0, l = 1,2 \tag{26}$$

$$\theta_{l,j}(0) = 0, j = 0,1, \ldots, n_l, \ l = 1,2 \tag{27}$$

where:

$$T_{l,j}^*(\tau) \equiv T^*(\zeta_{l,j}, \tau), \ k_{l,j}^*(\tau) \equiv k_l^*[T_{l,j}^*(\tau)]$$

$$\tau > 0, j = 0,1, \ldots, n_l \tag{28}$$

From the boundary conditions (24) and (25) on the contact surface $\zeta = 0$ we find:

$$\Theta_{l,-1}(\tau) = \Theta_{l,1}(\tau) + (-1)^{l-1} g_l(\tau),\ \tau \geq 0,\ l = 1,2 \quad (29)$$

$$g_1(\tau) = \{1 - Bi[T^*_{1,0}(\tau) - T^*_{2,0}(\tau)]\}\Delta\zeta_1/K^*_0 \quad (30)$$

$$g_2(\tau) = \{1 + Bi[T^*_{1,0}(\tau) - T^*_{2,0}(\tau)]\}\Delta\zeta_2 \quad (31)$$

By introducing functions:

$$A_{1,j}(\tau) = \frac{k^*_0 k^*_{1,j}(\tau)}{(\Delta\zeta_1)^2},\ A_{2,j}(\tau) = \frac{k^*_{2,j}(\tau)}{(\Delta\zeta_2)^2} \quad (32)$$

and taking into account the relations (26), (29)–(31), Cauchy problem for a system of ordinary differential equations (22)–(27) we write in the form:

$$\frac{d\Theta_{l,0}(\tau)}{d\tau} = A_{l,0}(\tau)[2\Theta_{1,1}(\tau) - 2\Theta_{1,0}(\tau) + (-1)^{l-1} g_l(\tau)]$$
$$\tau > 0 \quad (33)$$

$$\frac{d\Theta_{l,j}(\tau)}{d\tau} = A_{l,j}(\tau)[\Theta_{l,j+1}(\tau) - 2\Theta_{l,j}(\tau) + \Theta_{l,j-1}(\tau)] \quad (34)$$
$$\tau > 0,\ j = 1,2,\ldots,n_l - 1$$

$$\frac{d\Theta_{l,n_l}(\tau)}{d\tau} = A_{l,n_l}(\tau)[2\Theta_{l,n_l-1}(\tau) - 2\Theta_{l,n_l}(\tau)],\ \tau > 0 \quad (35)$$

$$\Theta_{l,j}(0) = 0, j = 0,1,\ldots,n = n_1 + n_2 + 2,\ l = 1,2 \quad (36)$$

Integration of the problem (33)–(36) is carried out by using the Adams's method. The method was carried out in DIFSUB procedure written in FORTRAN (Gear, 1971). This procedure is used to perform one step of the independent variable τ, and therefore the numerical integration of the initial value problem (33)–(36) at a predetermined time interval requires a multiple "call" of this procedure. The detailed information about the package DIFSUB are contained in the monograph (Krupowicz, 1986).

As a result of solving the initial problem (33)–(36), the values $\Theta_{l,j}(\tau)$ of Kirchhoff's function (11) were found in the nodes of the grid (19) at a specific point of dimensionless time τ. In order to make the transition from Kirchhoff;s function to respective values $T^*_{l,j}(\tau)$ of dimensionless temperature, we must define the functions $K^*_l(T^*_l)$ and $c^*_l(T^*_l)$, $l = 1,2$ in the formulas (1). We assume they have the polynomial form:

$$K^*_l(T^*_l) = \sum_{n=0}^{N_l} a_{l,n}(T^*_l)^n,\ c^*_l(T^*) = \sum_{n=0}^{M_l} b_{l,n}(T^*_l)^n$$
$$l = 1,2 \quad (37)$$

with known coefficients $a_{l,n}$ and $b_{l,n}$ (Yune, Bryant 1989). Then, with regard to equations (11) and (37), the relationship between the dimensionless temperature and the Kirchhoff's function will be also polynomial (Och, 2014):

$$T^*_{l,j}(\tau) = \sum_{n=0}^{N_l} c_{l,n}[\Theta_{l,j}(\tau)]^n,\ \tau \geq 0,\ j = 0,1,\ldots,n_l$$
$$l = 1,2. \quad (38)$$

We also note that at the constant thermal properties of the materials ($K^*_l(T^*)$=$c^*_l(T^*) = 1$) from the formula (11) it follows the linear relationship between temperature and the Kirchhoff function:

$$T^*_l(\zeta,\tau) = T^*_0 + \Theta^*_l(\zeta,\tau),\ |\zeta| < \infty,\ l = 1,2 \quad (39)$$

5. NUMERICAL ANALYSIS

Calculations have been performed for the same materials of the friction pair (aluminium AL MMC – metal-cermic FMC-845) and at the same input parameters as in article (Och, 2014), in which analytical-numerical solution of boundary-values problem (2)–(7) was found by method of successive approximations. Thermophysical properties of materials at initial temperature $T_0 = 20°C$ are given in Tab. 1, and the values of the coefficients ($a_{l,n}, b_{l,n}, c_{l,n}$) in the formulas (37)–(39) – in Tab. 2, in the above-mentioned paper. Dimensionless thickness of the layers were the same and equal $\delta_1 = \delta_2 = \delta_0 = 5$, the numbers of compartments breakdown of each layer were the same, too: $n_1 = n_2 = n_0$. Thus, the initial problem (33)–(36) with a number of equations $n = 2n_0 + 2$ was solved by the procedure DIFSUB.

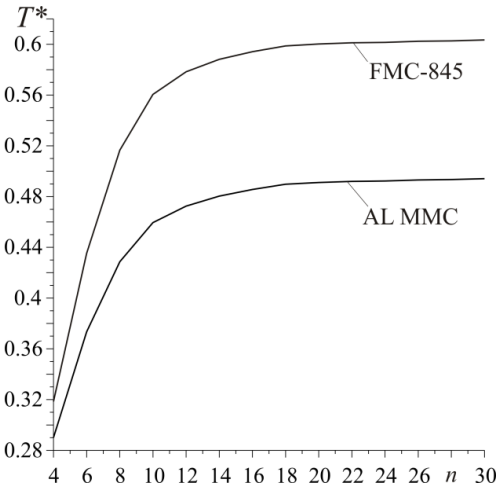

Fig. 2. Dependence of dimensionless temperature T^*_l, $l = 1,2$ on the contact surface $\zeta = 0$ on parameter n, at $\tau = 2$

The convergence of the calculation process of dimensionless temperature on the friction surface depending on the parameter n inversely related to the dimensionless length of the step grid $\Delta\zeta_1 = \Delta\zeta_2 = \delta_0/n_0$, is shown in Fig. 2. For a given relative accuracy of the calculations $\mathrm{EPS} = 10^{-6}$, the temperatures of both materials are almost unchanged at $n \geq 20$. The thermal conductivity of metal-ceramic FMC-845 is less than the conductivity of the aluminum matrix composite AL MMC (Och, 2014). As the result, the temperature of the friction surface of the metal-ceramics is higher than the temperature on the surface of the composite.

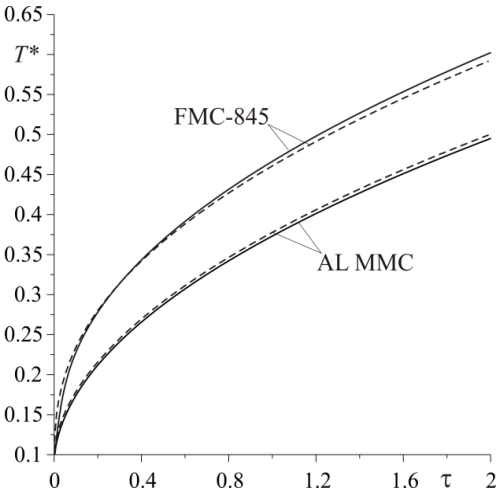

Fig. 3. Evolutions of dimensionless temperature T^*_l, $l = 1,2$ on the contact surface $\zeta = 0$, obtained by using the method of lines (solid lines), and by using the method of successive approximations (Och, 2014, dashed lines).

DOI 10.1515/ama-2015-0007

Evolutions of dimensionless temperature on the contact surface during sliding at a constant speed for the considered friction pair, are presented in Fig. 3. In this figure solid lines shows the results of calculations obtained by method of lines, using the procedure DIFFSUB, while the dashed lines presents the results of calculations obtained by successive approximations and presented in the article (Och, 2014). We may see that the dimensionless temperature curves calculated for aluminum matrix composite AL MMC by using both methods are practically the same. For metal-ceramic FMC-845 from about half of the heating time the slight difference between the respective curves is noticeable.

Isotherm of friction elements AL MMC and FMC-845 in the coordinate system $\zeta\tau$ are presented in Fig. 4. With the beginning of sliding temperature in any cross-section relative to the ζ increases. Maximum temperatures are reached at the surfaces of the friction elements at $\zeta = 0$ and the temperature of both bodies decreases with increasing distance from this surface. High thermal conductivity of AL MMC and substantially smaller of FMC-845 causes that the effective depth of heat penetration of aluminium composite is two times greater than the metal-ceramic.

When using iterative methods to solve nonlinear thermal problems of friction at the initial "zero" step, we must have a solution (preferably the analytical one) to the corresponding linear problems (Yevtushenko et al., 2015). The methodology proposed in this paper proves to be effective when it is difficult or even impossible to obtain such analytical solutions of linear problems. For example there is a change of the specific power of friction in time in the form $q(\tau) = q_0 q^*(\tau)$, when $q^*(\tau) = 1 + sin(\omega\tau), \tau \geq 0$, where for $\omega = 0$ we obtain the problem considered above. Change with time of friction elements temperature at constant ($\omega = 0$) and oscillating ($\omega = 50$) (Kuciej, 2011) specific power of friction is presented in Fig. 5.

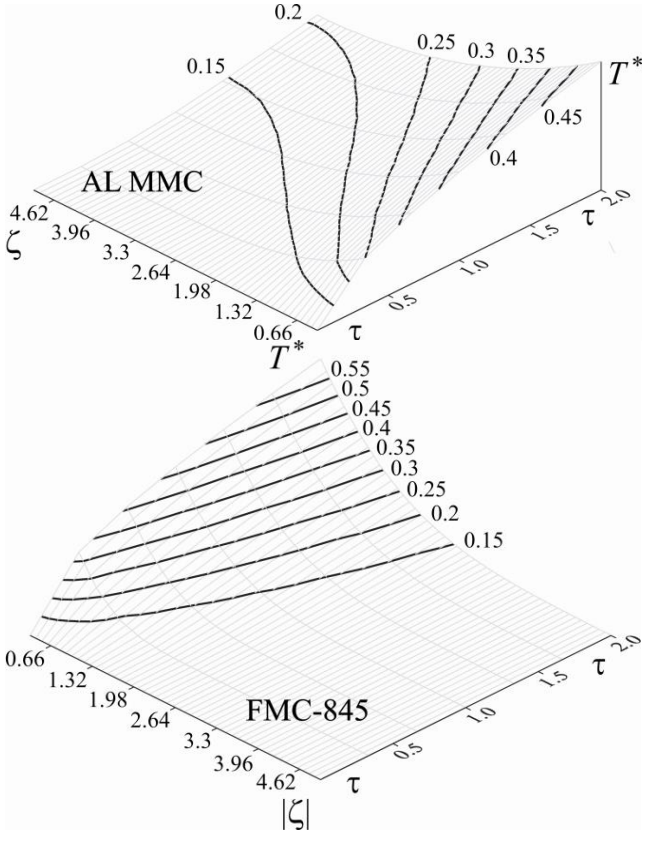

Fig. 4. Spatial and temporal distribution of dimensionless temperature

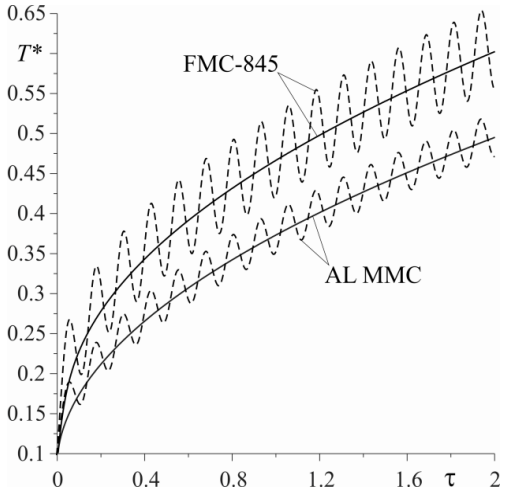

Fig. 5. Evolution of dimensionless temperature $T_l^*, l = 1{,}2$ on the contact surface $\zeta = 0$ at $\omega = 0$ (solid lines) and $\omega = 50$ (dashed lines)

When using iterative methods to solve nonlinear thermal problems of friction at the initial "zero" step, we must have a solution (preferably the analytical one) to the corresponding linear problems (Yevtushenko et al., 2015). The methodology proposed in this paper proves to be effective when it is difficult or even impossible to obtain such analytical solutions of linear problems. For example there is a change of the specific power of friction in time in the form $q(\tau) = q_0 q^*(\tau)$, when $q^*(\tau) = 1 + sin(\omega\tau), \tau \geq 0$, where for $\omega = 0$ we obtain the problem considered above. Change with time of friction elements temperature at constant ($\omega = 0$) and oscillating ($\omega = 50$) (Kuciej, 2011) specific power of friction is presented in Fig. 5.

6. CONCLUSIONS

The solution to one-dimensional nonlinear heat conduction problem of friction for two thermosensitive was obtained by method of lines.

The calculations were conducted for the friction pair (aluminium AL MMC – metal-cermic FMC-845), whose materials are arbitrary nonlinear. Comparison of the results obtained by the method of lines with the results calculated by the method of successive approximations (Och, 2014) was carried out.

Application of the numerical method presented in the article, preceded by the preparation of an appropriate analytical problem (partial linearization), gives perspective to obtain new analytical-numerical solutions to nonlinear heat conduction problems of friction, which cannot be solved by using analytical methods.

Nomenclature: a – characteristic dimension; b_i – Biot number; c – specific heat; c_0 – specific heat at an initial temperature; f – friction coefficient; h – coefficient of thermal conductivity of contact; K – coefficient of thermal conductivity; K_0 – coefficient of thermal conductivity at an initial temperature; k – coefficient of thermal diffusivity; p_0 – pressure; q_0 – specific power of friction; T – temperature; T_0 – initial temperature; T^* – dimensionless temperature; t – time; V – sliding speed; z – spatial coordinate; Θ – Kirchhoff's function; ρ – specific density; τ – Fourier number; ζ – dimensionless spatial coordinate.

REFERENCES

1. **Awrejcewicz J., Pyr'yev Yu.** (2009), *Nonsmooth dynamics of contacting thermoelastic bodies*, Springer-Verlag, New York.
2. **Barber J. R.** (1970), The conduction of heat from sliding solids, *Int. J. Heat. Mass Tran.*, Vol. 13, 857–869.
3. **Belyakov N. S., Nosko A. P.** (2010), *Nonperfect thermal contact of friction bodies*, *KD LIBROCOM*, Moscow, (in Russian).
4. **Chichinadze A. V., Braun E. D., Ginsburg A. G., Ignat'eva Z. V.** (1979), *Calculation, Test and Selection of Frictional Couples*, Nauka, Moscow (in Russian).
5. **Evtushenko O, Kuciej M., Och E**. (2014 a), Influence of the thermal sensivity of materials on the temperature at friction, *Mat. Sci.*, Vol. 50, No 1, 117–122.
6. **Evtushenko O., Kuciej M., Och E.** (2014 b), Modeling of temperature conditions for a braking system with regard for the heat sensitivity of materials, *Mat. Sci.*, Vol. 50, No 3, 397–405.
7. **Evtushenko O.O., Pir'ev Yu.O.** (1999), Computation of the contact temperature and wear during braking, *J. Math. Sci.*, Vol. 96, 2892–2896.
8. **Gear C. W.** (1971), *Numerical initial value problems in ordinary differential equations*, Prentice-Hall, Englewood Cliffs.
9. **Hall G., Watt J. M.** (1973), *Modern numerical methods for ordinary differential equations,* Clarendon Press, Oxford.
10. **Kalin M.** (2004), Influence of flash temperatures on the tribological behaviour in low-speed sliding: a review, *Materials Science and Engineering A*, Vol. 374, 390–397.
11. **Kirchhoff G. R.** (1894), *Heat theory lectures*, B.G. Teubner, Leipzig (in Germany).
12. **Krupowicz A.** (1986), *Numerical Methods of Initial Value Problems of Ordinary Differential Equations* (in Polish), *PWN*, Warsaw.
13. **Kuciej M.** (2011), Accounting changes of pressure in time in one-dimensional modeling the process of friction heating of disc brake, *Int. J. Heat Mass Trans.*, Vol. 54, 468-474.
14. **Kuciej M.** (2012), *Analytical models sof transient frictional heating*, Publisher of Technical University of Bialystok, Bialystok.
15. **Kushnir R. M., Popovych V. S.** (2011), Heat conduction problems of thermosensitive solids under complex heat exchange. In: Heat conduction – Basic Research, V. Vikhrenko Ed., *In Tech*, Croatia, 131–154.
16. **Nosko A.L., Belyakov N.S., Nosko A.P.** (2009), Application of the generalized boundary condition to solving thermal friction problems, *J. Frict. Wear*, Vol. 30, 615–625.
17. **Och E.** (2013), Frictional Heating During Sliding of Two Semi-Spaces with Simple Thermal Nonlinearities, *Acta Mech. et Autom.*, Vol. 7, No 4, 236–240.
18. **Och E.** (2014), Frictional Heating during Sliding of Two Semi-Spaces with Arbitrary Thermal Nonlinearity, *Acta Mech. et Autom.*, Vol. 8, No 4, 204–208.
19. **Olesiak Z., Pyryev Yu., Yevtushenko A.** (1997), Determination of temperature and wear during braking, *Wear,* Vol. 210, 120–126.
20. **Ozisik M. N.** (2000), *Finite difference methods in heat transfer*, Second Ed., CRC Press, Florida, USA.
21. **Podstrigach Ya. S.** (1963), The temperature field in a system of rigid bodies coupled by thin interface, *Inzh.-Fiz. Zh.*, Vol. 6, No 10, 129–136, (in Russian).
22. **Pyr'yev Yu.** (2004), *Dynamics of contact systems with respect to heat, friction and wear*, Publisher of Technical University of Lodz, Lodz.
23. **Rhee S. K., Jacko M. G., Tsang P. H. S.** (1991), The role of friction film in friction, wear and noise of automotive brakes, *Wear*, Vol. 146, No 1, 89–97.
24. **Sazonov V. S.** (2008), Nonideal contact problem of nonstationary heat conduction for two half-spaces, *J. Eng. Phys. Thermophys.*, Vol. 81, 397–408.
25. **Yevtushenko A., Kuciej M., Och E.** (2014a), Effect of Thermal Sensitivity of Materials of Tribojoint on Friction Temperature, *J. Frict. Wear*, Vol. 35, 77–83.
26. **Yevtushenko A., Kuciej M., Och E.** (2014b), Influence of thermal sensitivity of the pad and disk materials on the temperature during braking, *Int. Comm. Heat Mass Transf.*, Vol. 55, 84–92.
27. **Yevtushenko A., Kuciej M., Och E.** (2014 c), Temperature in thermally nonlinear pad-disk brake system, I*nt. Comm. Heat Mass Transf.*, Vol. 57, 274–281.
28. **Yevtushenko A., Kuciej M., Och E.** (2015), Some methods for calculating temperature during the friction of thermosensitive materials, *Numer. Heat Transf. P. A.*, V. 67, N 6 (2015), 696–718.
29. **Yevtushenko A.A., Kuciej M.** (2012), One-dimensional thermal problem of friction during braking: The history of development and actual state, *Int. J. Heat Mass Tran.*, Vol. 55, 4118–4153.
30. **Yevtushenko A.A., Kuciej M., Yevtushenko O.** (2013), The boundary conditions on the sliding surface in one-dimensional transient heat problem of friction, *Int. J. Heat Mass Trans.*, Vol. 59, No 1, 1-8.
31. **Yune Y.G., Bryant M.D.** (1989), Thermal evolution of hot spots in thermally nonlinear carbon graphite sliders, *Trans. ASME. J. Tribology*, Vol. 111, 591–596.

Acknowledgement. The present paper is financially supported by the National Science Centre of Poland (project No 2011/01/B/ST8/07446).

DOI 10.1515/ama-2015-0008

AUTOMATIZATION OF CONTACT PRESSURE MEASUREMENT BETWEEN TRUNK ORTHOSIS AND PATIENT'S BODY USING A MATRIX TACTILE SENSOR

Radovan HUDÁK*, Viktória RAJŤÚKOVÁ*, Jozef ŽIVČÁK*

*Faculty of Mechanical Engineering, Department of Biomedical Engineering and Measurement,
Technical University of Košice, Letná 9, 042 00 Košice, Slovakia

radovan.hudak@tuke.sk; viktoria.rajtukova@tuke.sk; jozef.zivcak@tuke.sk

Abstract: Trunk orthosis affects trunk by a corrective-pressure mode with an objective to correct deformities (e.g. scoliosis). The effectiveness of this function depends on various factors, i.e. correct orthosis manufacture, correct application to patients and regular pressure corrective effect control. All these factors can be monitored by a system for measurement and evaluation of the contact pressure between the instrument and trunk in a real time and also by a so called "off line" system data recording. Presented article describes the application of made-to-measure sensor system TACTILUS (Sensor Products, USA) in different regimes (ambulance – A, home – H, combined – HA and multi-sensory ambulance – MA regime), testing of chosen static and dynamic matrix tactile sensor (MTS) parameters and results of the testing application between orthosis and patients' trunks.

Key words: Matrix Tactile Sensor (MTS), Contact Pressure, Trunk Orthosis, Scoliosis

1. INTRODUCTION

The current state in the field of pressure measurement between orthosis and patient's trunk at spine deformities is presented by several studies that solve the issue only partialy.

Clin J. et al. (2010) in their study found out that compressive pressures do not exceed the value of 1 MPa at the application of Charleston trunk orthosisThe same author, in his further study observed, while studying TLSO orthosis, that there is a frontal bending reduction by corset application with power of 60 N in 20% (Živčák et al., 2007). Wong M.S. et al. (2000) set the average pressure functioning by the means of force pad to body with values 7.09 +/- 1.77 kPa (53.2 +/- 13.3 mmHg) while the fixation belts pass was 26.8 +/- 5,2 N (Penhaker et al., 2012). Pèriè et al. (2004) found out that sagittal reaction forces moved up to 47N with the corset (Krištof and Hudák, 2010).

In 2006, Romano et al. (2006) measured contact pressure when applying corset within patients with idiopathic scoliosis. They applied a sensor with dimensions 7.62 x 20.32, thickness of 0.1016 mm. While measuring the pressure in different positions of patient, they observed average pressure values moving from 264.3 g/cm² at sitting up to 431 g/cm² at exercising. Maximum values moved from the range of 367 g/cm² to 958 g/cm².

Based on the analysis of the studies carried out up to now, own sensor system was designed, following required dimensions, pressure range and the way of placing the tactile elements.

Suggested system for continuous contact pressure measurement between trunk orthosis and patient's body in a real time is a specific way of matrix tactile sensor (MTS) application in various trunk orthosis phases (manufacture, finalizing, application). Based on the four mentioned phases, four system regimes for dynamic pressure measurement were designed, i.e. ambulance (A), home regime (H), home – ambulance regime (HA) and multi-sensory ambulance regime (MA).

The scheme of sensory system for contact pressure continuous measurement between force pad (trunk orthosis) and patient's trunk in a real time is described in Fig.1. Sensor fixation for dynamic measurement in a real time must be firm enough, however removable for the needs of the system application into a different force pad. Sensor thickness (0.7 mm) is considered within the trunk orthosis construction, mainly from the point of view of biomechanical force pad´s function on the patient's body.

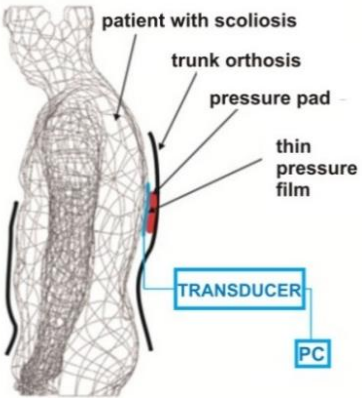

Fig. 1. Scheme of sensory system for continuous measurement in a real time

Real time measuring system, in the process of trunk orthosis manufacture can be applied at the control of shape and dimensions of the orthosis and way of placing the force pads. It can also be applied when trying the corset, before its finalizing, when the corset is applied directly on the patient with a possibility of further shape and biomechanical modifications based on the measurement outputs. The measurements will take place at the department of prosthetics and orthotics, both in phases of corset manu-

facture and its testing, therefore it is an ambulance sensory system, i.e. A – regime (Fig. 2).

Measuring system is used also during the corset application phase. In this phase, biomechanical effect of the instrument is used from a long term point of view (patient wears corset in home environment). Biomechanical control was missing in this phase.

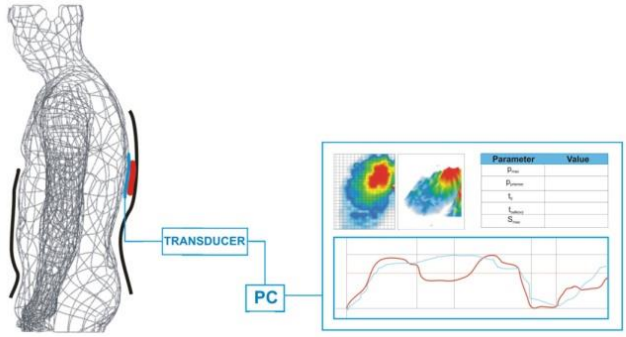

Fig. 2. Ambulance measure regime (real-time)

Therapeutical effect of the corset was monitored on the basis of regular scanning considering the invasiveness of RTG or CT diagnostics.

The measuring system was named as home (off-line) or so called H - regime (Fig. 3), where the pressure effectiveness scanning is carried out in home environment, but the analysis and evaluation is done in the orthopedic ambulance after the data is downloaded. The data transfer in home regime is possible by a cable (Fig. 3-1) or by wireless transfer (Fig. 3-2).

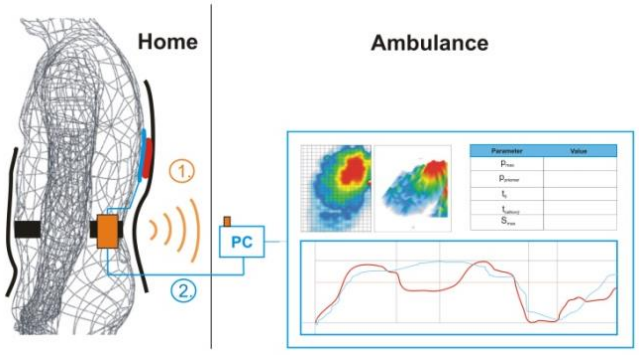

Fig. 3. Home regime (off-line), so called H – regime of pressure scanning

In the corset application phase, so called HA regime can also be used – it means home and ambulance regime (Fig. 4), where the data can be transferred in a real time. Thus, orthopedist can monitor the situation and effect of trunk orthosis application in any place and intervene if necessary. Home – ambulance regime measurement can have different ways of data transfer (Fig. 4. PC – H – home computer, PC – A – computer in ambulance).

In the Fig. 5 there is a multi-sensory pressure scanning system between trunk and various force pads at the same time in a real time. This system enables to analyze pressure modes between more force pads and thus, draw a complex biomechanical trunk orthosis effects on patient. Mentioned system requires a solution of multichannel sensory system with a specific data collection point and own software application in order to synchronize pressure outputs from the individual force pads.

Outputs, analyzed using software application are evaluated qualitatively (2D and 3D colour maps), and also quantitatively, where the situation is evaluated using particular pressure and time data and statistically processed values. For the purposes of MTS system made-to-measure testing, an ambulance measurement regime (A-regime) was chosen, used for testing the orthosis manufacture effectiveness.

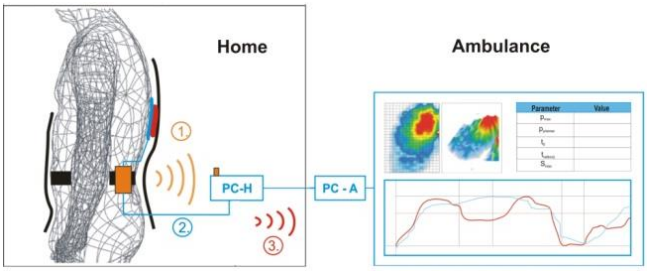

Fig. 4. HA – Home (off-line) – ambulance (real - time) regime measurement

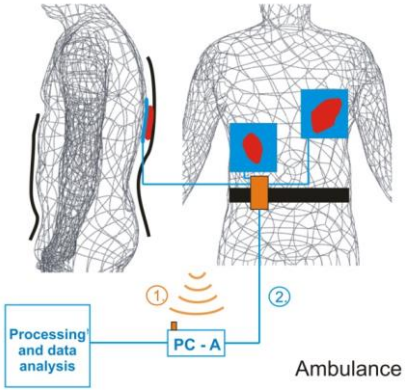

Fig. 5. MA – Multi-sensory ambulance regime measurement

2. AMBULANCE MEASUREMENT SYSTEM (A-REGIME) – MATERIAL AND METHODS

Ambulance measurement system in a real time consists of measurement pressure mat application between force pad and patient's trunk in ambulance, considering that the process requires continuous professional assistance at the time of measurement. The objective of the ambulance system is to verify the corset construction (shape, dimensions) before delivering it to a patient. At the same time, at regular visits in ambulance, it is possible to control the effect of force pad from the biomechanical point of view and thus verify any need of corset or force pad modification in order to optimize the pressure effect.

System function verification was carried out from so called A – regime of scanning, in the phase of corset manufacture. In this phase, it is possible to measure and analyze the shape and dimensions of corset construction and verify the way of placing of force pads based on their pressure effect. On the basis of studies, a sensor system was designed and manufactured in order to measure contact pressure between trunk and orthosis force plate in a real time. The sensor system consists of a sensory mat (20 x 20 cm), signal converter and connecting cables. The pressure range MTS was set from 0 to 724 PSI (from 0 to 729 mmHg). In order to ensure free movement of the patient with

DOI 10.1515/ama-2015-0008

applied pressure mat, suggested length of the connecting cable was 10 meters. Wide cables with 40 veins represent signals from the individual sensors which create matrix of 400 scan points. After the system hardware modules were set up, work with the software application TACTILUS (Sensor Products, USA) started. This application serves not only for processing and evaluation the measured data, but also for operating the whole sensor system. After the final record editing, the software is able to generate a text file (.txt) which contains all recorded images. The output file contains information about pressure values, maximal, minimal, average pressure and final force out of the matrix. In order to verify the system and process the methodology of measurement for ambulance system, testing measurements were carried out to find chosen static and dynamic MTS parameters and measurement in 10 subjects. The aim of the measurement was to find the entry parameters for MTS applications to the place of scanning, find the MTS time response and other metrological parameters and also to design optimal measurement methodology in ambulance regime. The aim was also to find pressure ratios and define referential graphs of pressure-time (p-t) and surface – time (S-t) dependences for the exercises defined above.

It was needed to carry out the testing of the chosen parameters in order to verify the set entry measurement methodology of biomechanical effect of force pad to trunk of the measured subject. The measurements were not aimed to test the measurement accuracy, but to find stability of measurement and of chosen static and dynamic parameters. Testing was implemented by 2 kg weights placed to the centre of the pressure mat.

Considering the fact that the aim of the measurement was measurement system verification for the purposes of processing the measurement methodology of the contact pressures between force pad and trunk, where relative changes are important, there was no temperature influence to measurement process analyzed, neither influence of the mat to output data was analyzed. It was identified by testing that hardness; shape and material of the mat have a significant influence on the measured data accuracy.

Methodology processing requires considering more factors, parameters and secondary measurements which will be considered at processing and evaluating the results. At measuring, it is necessary to consider parameters of the subjects (S01 : S10), environmental parameters (temperature, humidity) and their changes in the course of measurement, corset shape, force pad placing and pressure mat fixation. Other important facts are the hardware set up, choice and correct application of defined exercises, software application and input parameters set up, data processing, numerical and graphical presentation of the results, evaluation of the results and their interpretation to the engineering and clinical practice.

The measurement took place in a special laboratory with dimensions of 6.2 x 3.5 m. The temperatures shifted during all measurements between 21.5 – 24.4 °C and relative humidity between 32.1 – 49.5%. Mentioned conditions met the requirements of measurements from the point of view of measuring system and thermal satisfaction of the measured objects.

Two types of corsets were applied to the measured subjects (S01 : S10) in a way that pressure between force pad and subject's body was created. Compression force between the force pad and mat was satisfactory for fixing the mat on the required place without moving, that is the reason why the pressure mat was not fixed.

From the point of view of placing of force pads, physical parameters of the objects and required pressure effects, there were 3 force pads (P1, P2, P3) used on the first corset (K1) and 2 force pads (P1, P2) on the second corset (K2).

After the correct pressure mat application, set procedures and exercises followed and were supported by biomechanical purpose or the disease itself (scoliosis).

Exercises and movements were set on the basis of available studies in the field of biomechanical analysis of corset influence to patient's trunk. The movements were applied to a control group of subjects with the aim of finding out the pressure ratios at individual exercises and set exemplary pressure procedures and size of surface in time. For all the force pads, movements like standing, forward bend, kyphotisation, kyphotisation on knees, backing out and raise arms. Using force pads, placed on the back or on the side of the corset, exercises like sitting, sitting and leaning, outstretching, lying on the back were preformed.

The setting of the exercises is followed by setting of the software application for contact pressure measurement in corsets and processing of the measured data.

It is crucial to set the parameters in the software application before scanning the pressure placement in order to obtain feedback about the correct pressure mat application, starting the measurement and satisfactory signal for a successful recording.

In order to visualize the placing of force pad's shape it was necessary to use interpolation functions. TACTILUS software offers some of the types, such as interpolations for pressure map editing, inverse distance weighting method (IDW), spline abilinear interpolation. However, in order to ensure correct result evaluation, it was necessary to use other types of interpolations, too.

After the correct entry data set up, recording of the measurement followed. With every subject (S01 : S10), every movement or exercise and every force pad, a video record of surface pressure placing was made in contact areas between force pad and pressure mat or trunk orthosis and pressure mat (Fig. 6).

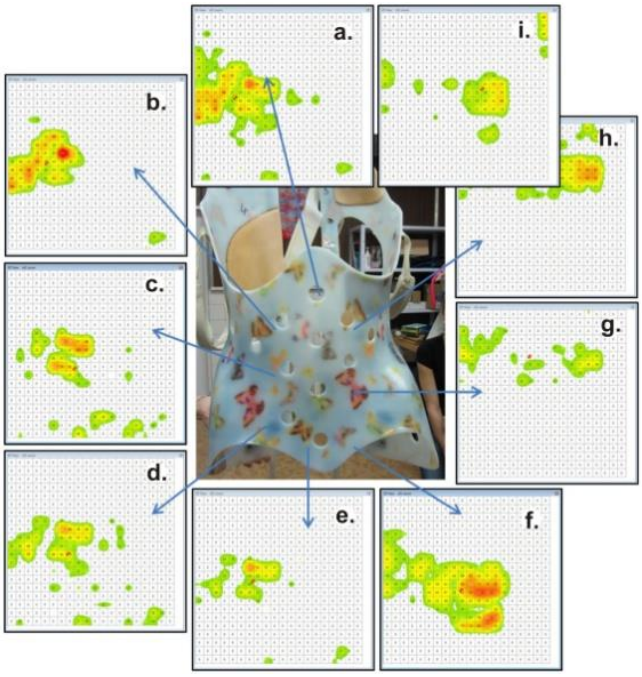

Fig. 6. 2D image with a maximum pressure value at various exercises and movements: a) kyphotisation, b) kyphotisation on knees, c) standing, d) backing out, e) raise arms, f) forward bend, g) sitting, h) sitting and leaning

The software application enables to export the files in a text format (.txt) as well as export the whole pressure data matrix. Except numerical data, it is possible to export graphs of pressure and surface processes in time. The software also covers functions for generating force "F" dependence on time t (F-t) which uses average pressure (p_{avg}) for the calculation (Fig. 7).

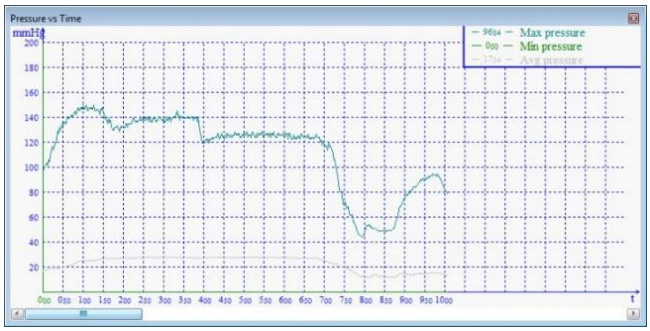

Fig. 7. Functionality graph: pressure-time ($p-t$) dependence for maximal p_{max}, average p_{avg} and minimal p_{min} recorded values

3. RESULTS OF SENSOR SYSTEM TESTING AND INTRODUCTORY MEASUREMENTS IN AMBULANCE

Before measuring the pressure between force pads and trunk of the tested subjects, it was necessary to carry out testing measurements in order to verify pressure mat and the whole sensor system functionality which enabled to set the methodology directly on the objects of measurement more effectively.

3.1. Testing results of chosen parameters of the pressure mat

There were short testing measurements effectuated on the pressure mat in order to obtain basic static, dynamic and noise properties. Series of repeated pressure measurements were taken caused by weights placed in the centre of the grid, where there is supposed area for placing force pads. These simple measurements enabled to find the response for step pressure change, estimate standard repeated measurement uncertainty and consider the short-term noise parameters of the device.

The first measurement series were aimed to determine the measuring system response, while its sensory system is under step pressure change. It is possible to characterize manually the typical response process from the zero to the second stable position (placing the weights on a sensory grid) or to characterize the transfer to a stable position determined by the size of weight and effective contact surface.

By these characteristics, the introductory contact pressure measurement phase is monitored, between force pad and trunk, where the pressure mat is placed and demonstrates the beginning of the scanning process where there is step pressure change due to the application of weights.

Based on the analysis of the mentioned processes it is clear that dynamic properties of the scanned sensory matrix are well approximated for the contact area evaluation by the following formula:

$$S = S_{max}\left(1 - e^{-t/\tau}\right) \quad \tau \approx 0{,}8s \tag{1}$$

where the time constant of transfer from the second stable status is approximately 0,8 seconds. The overall contact surface is calculated on the basis of sensory grid pressure signals integration, thus it will correspond to the dynamics of the grid sensors.

Repeated measurement series were carried out with weights of 1 and 2kg in 30 second time intervals at sampling frequency 49 Hz considering that the position of the weight was changed at every measurement. The aim was to qualify the repeated pressure measurement accuracy that depends on electrical, material, geometrical and constructional parameters of piezoelectric sensors' network.

For every series, there were basic statistic surface properties calculated (arithmetic mean and median) and width (diffusion and standard deviation) of the data division and set type A uncertainty. The following relations were used:

$$\overline{p} = \frac{1}{n}\sum_{i=1}^{n} p_i \quad s^2(p) = \frac{1}{n}\sum_{i=1}^{n}\left(p_i - \overline{p}\right)^2 \tag{2}$$

Standard uncertainty of every measurement series was subsequently calculated based on the relation:

$$u_A(\overline{p}) = s(\overline{p}) = \frac{s(p)}{\sqrt{n}} = \sqrt{\frac{1}{n(n-1)}\sum_{i=1}^{n}\left(p_i - \overline{p}\right)^2} \tag{3}$$

Based on the calculated statistical properties, it is possible to state that the overall arithmetic pressure mean out of all series carried out by repetitive measurement is $\bar{p} = 43.25mmHg$ a standard deviation $s(p) = 0.92\ \mathrm{mmHg}$ and the standard uncertainty type A $uA(p) = 0.07\ \mathrm{mmHg}$.

For the B type standard uncertainty, producer data were used. The error 10% of the measuring system represents value of $4.32\ \mathrm{mmHg}$ out of all the repeated measurements series. As we suppose equal division of the error probability of the measuring system, the B uncertainty can be expressed as follows:

$$u_B(p) = \frac{4{,}325}{\sqrt{3}} \approx 2.50\ \mathrm{mmHg} \tag{4}$$

Overall measuring system uncertainty:

$$u_C(p) = \sqrt{u_A(p)^2 + u_B(p)^2} \tag{5}$$

After substitution, the overall measuring uncertainty is $u_c(p) = 2.50\ \mathrm{mmHg}$ and the determining factor is the measuring system accuracy.

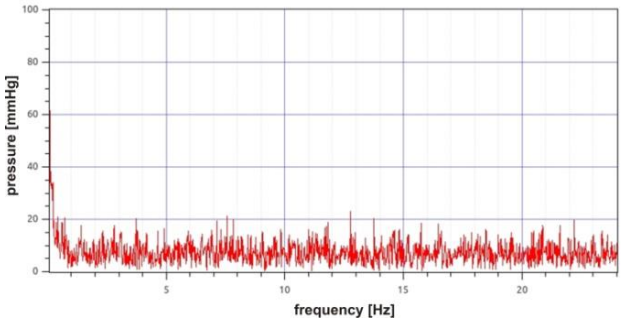

Fig. 8. Functionality graph: pressure-time ($p-t$) dependence for maximal p_{max}, average p_{avg} and minimal p_{min} recorded values

From the point of view of sensitivity and differentiating ability of the measuring system, knowledge of noise properties is crucial. It is important to consider the noise also when the interference

DOI 10.1515/ama-2015-0008

can influence the information in noise or when the information itself is "drowned" in the noise and it necessary to acquire and reconstruct it.

Spectral noise properties are relatively constant in time and it is possible to derive noise capacity out of them that is concentrated in a particular frequency zone. In Fig. 8 there is an amplitude frequency spectrum of typical noise signal and it is clear that it does not contain any significant spectrum of line, it is flat and it responds to thermal noise spectrum.

Statistical properties are constant and noise values "very distant" from zero are little probable. Based on these facts it is possible to state that the noise in the signal does not influence the amount of the measured constant.

3.2. Results of the introductory measurements using TACTILUS system in ambulance A-regime

The results of introductory measurements were processed to charts and graphs for every movement and exercise. Values of the average contact pressure p_{avg} and contact surface S_{avg} and also maximal contact pressure p_{max}, and contact surface S_{max}, were obtained.

Kyphotisation is presented by maximal contact pressure (Fig. 9) in the range from 0 to 40 mmHg.

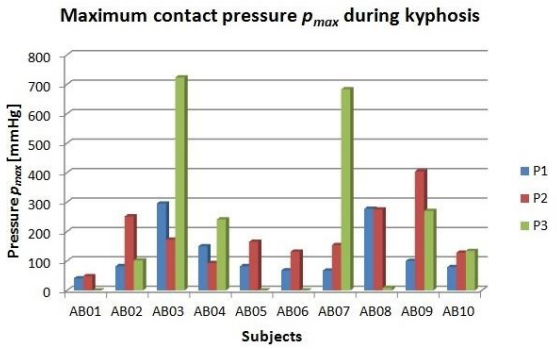

Fig. 9. Maximal contact pressure at kyphotisation within individual objects of measurement

Based on the graphic data presentation (Fig. 10) it is clear that the largest contact surface is at the force pad P2 and the values range from 0 to 100 cm². The lowest values are at the force pad P3 and they range from 0 to 40 cm².

Based on the analysis, it was stated that force pad P3 show higher average and maximal contact pressures, so do force pads P1 and P2, the majority of average contact pressure values range from 0 up to 200 mmHg (0 – 26,6645 kPa).

The lowest values of average and maximal contact pressure are to be found at raise arms. On the other hand, it is not possible to clearly define during which exercise there are the highest values of average and maximal contact pressure; on the whole, the values are higher at kyphotisation and kyphotisation on knees. Within the average and maximal contact surface it is not clearly defined which exercise represents the highest or the lowest values.

Graphs in Fig. 11 and 12 show maximal pressure p_{max} and maximal surface S_{max} at individual movements on force pad P2.

At the force pad P2, specific movements and exercises were carried out and they influence of force pad placed at the back part of the trunk orthosis. The highest pressure at force pad P2 was monitored while lying on the back, the lowest while outstreching.

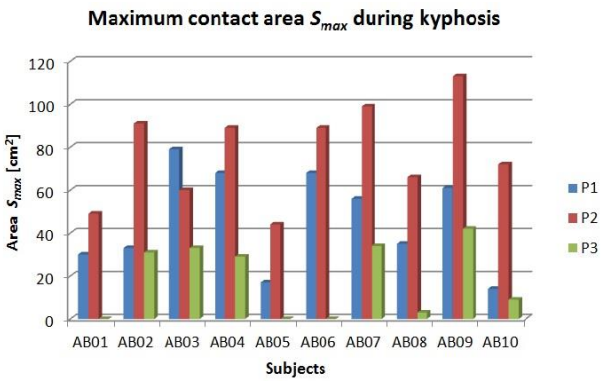

Fig. 10. Maximal contact surfaces at kyphotisation within individual objects of measurement

Pressure variations directing upwards or downwards within the individual objects of measurement describe various physiological proportions of the objects of measurement (various BMI index).

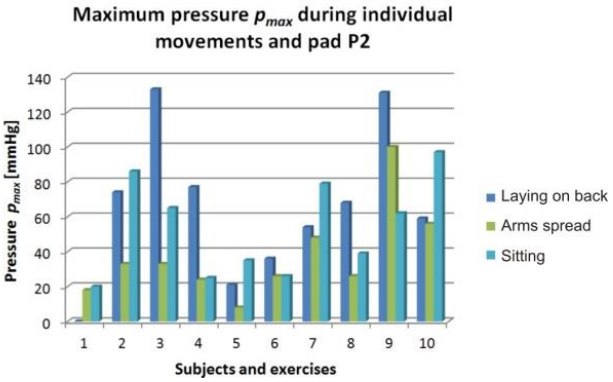

Fig. 11. Maximal contact pressure within the individual force pad (P2)

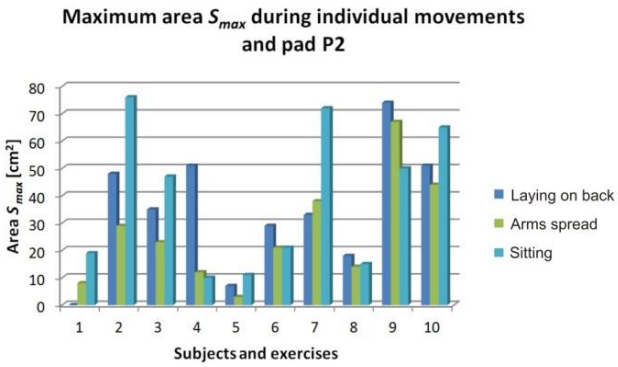

Fig. 12. Maximal contact surface within the individual movements (force pad P2)

If we eliminate extreme values out of the analysis, average pressures at three exercises on force pad P2 moved from approximately 0 to 80 mmHg (0 – 10.6658 kPa). The average surfaces were also the largest while lying on the back, which is related to pressure at this position (movement). Maximal surfaces were higher also while sitting and leaning against a chair.

Following the same method, outputs for standing position were obtained (Fig. 13). While standing without any other movement, sinusoid curves are visible and they represent increase and decrease in pressure at breathing. Within other movements, the output curves were so variable that it was not possible to evaluate them and clearly define reference process of neither pressures nor contact surfaces.

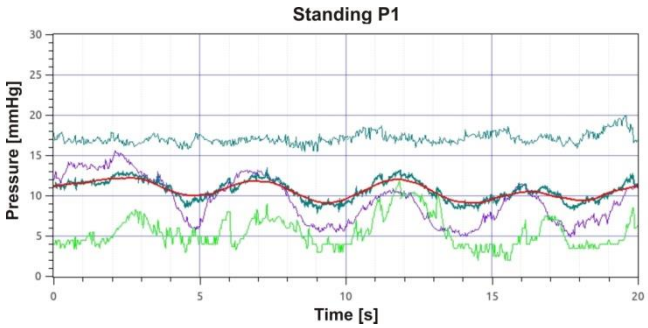

Fig. 13. Average pressures processes in time of standing position within all objects of measurement

4. CONCLUSION

Based on the analysis of the custom TACTILUS system, it was determined that the system from the point of view of range and sensitivity is correctly dimensioned. Chosen static and dynamic parameters were also tested. The overall measuring system uncertainty was obtained by the calculation from uncertainty A and uncertainty type B, where the value $u_c(p) = 2.50\ \mathrm{mmHg}$ was calculated.

Amplitude frequency noise spectrum does not contain any significant spectrum of line, it is flat and it responds to the thermal noise spectrum.

From the point of view of dynamic mat parameters, the calculations show that the time constant of transition to the second stable status is approximately 0.8 seconds. It means a relatively quick response to the weight change. This data will be verified based on the further measurements.

The aim of the analysis was also to create reference processes for all analyzed parameters and all implemented movements or exercises. In this case, reference curves were set up for kyphotisation and standing position. Regarding the other curves, it is necessary to carry out further large measurements and on their basis a database of reference curves of the most frequent movements or deliberately defined movements will be created. According to this database, clinical staff will be able to analyze pressures at measurements in ambulance regime (orthosis testing), but also in home regime where it will be clear which movements were done by the patient, if he applied the trunk orthosis correctly and which time period was the trunk orthosis used for.

REFERENCES

1. **Bergeron Ch., Cheriet F., Ronsky J., Zernicke R., Labelle H.** (2005), Prediction of anterior scoliotic spinal curve from trunk surface using support vector regression, *Engineering Applications of Artificial Intelligence*, 18, 973–983.
2. **Berryman F., Pynsent P., Fairbank J., Disney S.** (2008), A new system for measuring three-dimensional back shape in scoliosis, *Eur Spine J.*, 17, 663 – 672.
3. **Clin J., Aubin C. E., Parent S., Labelle H.** (2010), A biomechanical study of the Charleston brace for the treatment of scoliosis, *Spine*, 1, 35(19), 940-7.
4. **Gál, P., Toporcer, T., Vidinský, B., Hudák, R., Živčák, J., Sabo, J.** (2009), Simple interrupted percutaneous suture versus intradermal running suture for wound tensile strength measurement in rats: A technical note *, European Surgical Research*., Vol. 43, No. 1, 61-65.
5. **Hermus J., Hulsbosch M., Guldemond N., Rhijn L. V.** (2009), Developing a new brace with pressure measurements, *6th International Conference on Conservative Management of Spinal Deformities*, Lyon, France, 1-1.
6. **Hermus J., Monteban P., Guldemond N., Rhijn L. V.** (2008), Pressure measurements in a new TLSO with a dynamic thoracic brace pad for idiopathic scoliosis, *5th International Conference on Conservative Management of Spinal Deformities*, Athens, Greece, 1-1.
7. **Krištof M., Hudák R., Takáčová A., Živčák J., Fialka L., Takáč R.** (2010), Contact pressure measurement in trunk orthoses, *IEEE International Joint Conferences on Computational Cybernetics and Technical Informatics*, Timişoara, Romania, 175-179.
8. **Kulesza E., Dąbrowski J. R., Sidun, J., Neyman A., Mizera J.** (2012), Fretting wear of materials–Methodological aspects of research, *Acta Mechanica et Automatica*, 6(3), 58-61.
9. **Penhaker M., Stankus M., Prauzek M., Adamec O., Peterek T., cerny M., Kasik V.** (2012), Advanced Experimental Medical Diagnostic System Design and Realization, *Electronics and Electrical Engineering*, 117.1, 89-94.
10. **Périé D., Aubin C. E., Lacroix M., Lafon Y. and Labelle H.** (2004), Biomechanical modelling of orthotic treatment of the scoliotic spine including a detailed representation of the brace-torso interface, *Medical and Biological Engineering and Computing*, 42, 3, 339-344.
11. **Praslicka D., Blažek J., Šmelko M., Hudák J., Čverha A., Mikita I., Varga R., Zhukov A.** (2013), Possibilities of measuring stress and health monitoring in materials using contact-less sensor based on magnetic microwires, *Magnetics*, *IEEE Transactions*, 49.1, 128-131.
12. **Skelly, A.** (2007), The smart brace: Hi-tech scoliosis brace monitors pressure levels, patient compliance, *Medical Post.* [online], 43/25; 29.
13. **Wong M. S., Mak A. F., Luk K. D., Evans J. H., Brown B.** (2000), Effectiveness and biomechanics of spinal orthoses in the treatment of adolescent idiopathic scoliosis (AIS), *Prosthet Orthot Int.*, 24(2):148-6.
14. **Zach L., Horak L., Ruzicka P., Konvickova S.** (2008), *Knee Joint Edoprosthesis - Verification of Contact Pressures by Pressure Sensitive Films* [online]., Sensor Products Inc.
15. **Živčák J., Hudák R., Krištof M., Bednarčíková L.** (2010), Surface pressure analysis in prosthetics and orthotics, *Advances in Human Factors, Ergonomics, and Safety in Manufacturing and Service Industries*, London, 845-854.
16. **Živčák J., Krištof M., Hudák R.** (2010), Pressure measurement in spinal brace - human body interaction area, *Lékař a technika*, 40/2, 20-24.

The work has been accomplished under the research project ITMS: 26220220185 MediPark Medical university science park in Kosice and the project ITMS No. 26220120060, Centre for research of control of technical, environmental and human risks for permanent development of production and products in mechanical engineering supported by the Research & Development Operational Programme funded by the ERDF.

DOI 10.1515/ama-2015-0009

THE STRUCTURE OF THE STRENGTH OF RIVETED JOINTS DETERMINED IN THE LAP JOINT TENSILE SHEAR TEST

Jacek MUCHA*, Waldemar WITKOWSKI*

*Faculty of Mechanical Engineering and Aeronautics, Rzeszow University of Technology,
al. Powstancow Warszawy 8, 35-959 Rzeszów, Poland

j_mucha@prz.edu.pl, wwitkowski@prz.edu.pl

Abstract: The article presents the analysis of the structure of the load capacity of riveted joints. For the four joining systems the lap joint specimens were made and tested in the shearing test. The joints were prepared for the three combinations of the DC01 steel and EN AW-5754 aluminium alloy sheets with the thickness of 2mm. On the basis of the obtained load-elongation diagram tensile shear test curves, the basic parameters defined in the ISO/DIS 12996 standard were determined. In the case of the conventional riveted joints the maximum load capacity of the joint is determined by the strength of the fastener. For the joints with aluminium-steel blind rivet , the load capacity of the joint was on the strength limit of the rivet tubular part and on the strength limit of the sheet material. The strength of the SSPR joint is determined by the mechanical properties of the material of the joined sheets. From all sheets and rivet specimens arrangements the highest load capacity of the joint was obtained for the DC01 sheet material joints, and the lowest load capacity of the joint was obtained for the EN AW-5754 sheet material joints.

Key words: Riveted Joints, Mechanical Joining, Sheets Joining, Shearing Test, Joint Strength

1. INTRODUCTION

The branches of industry which generate new product solutions very fast are construction, aerospace and automotive industry. Steel elements are increasingly substituted by fiber-reinforced plastic parts or by light metal alloys parts such as aluminium or magnesium alloys. New material generates the need of developing the new joining technologies or modifying standard technologies. The use of new material in the production processes resulted in the use of the alternative joining technologies at the expense of the traditional technologies. That is why the experimental studies related to the formation and strength of new joining systems are required. The new joining solutions not always can ensure an adequate strength of a joint. In some cases the joint formation for the new materials is very difficult. Thus, the riveted joint technologies with blind rivets or with blind rivets for closing up are still used and will certainly continue to be used in the future. A very large group of the riveted joints includes self-piercing rivet joints "SPR" (Gao and Budde, 1994; Voelkner et. al., 2002; Nong et. al., 2003; Neugebauer et. al., 2008; He et. al., 2008; Todtermuschke, 2009). The self-piercing riveting technology has several varieties of formation with high values of forming force. One of them is solid self-piercing riveting (SSPR), the technology offered by the Kerb-Konus-Vertriebs GmbH company (2013). The SSPR technology ensures the joint flat surface from the rivet side (Neugebauer et al., 2010; Mucha, 2013; Mucha, 2014). This joining technology also allows to effectively join materials with significant difference in mechanical properties, eg. soft with tough materials (Meschut, 2014). During the joint formation by sheet pressing, e.g. clinching (CL), self-piercing riveting with tubular rivet (SPR) or clinch riveting (CR,) the material can crack (Kaščák et al., 2013). Moreover, these type of joints are characterized by the flash, which is the result of the joint formation technology. In Poland, these types of joints are not under any adequate standard.

The classification of joints formed by pressing is presented in DIN standard (DIN 8593-0:2003, 2003a; DIN 8593-5:2003, 2003b). Other international standards define the specimens dimension, testing conditions and the failure of the lap joints of various types (DIN EN ISO 14272, 2002; EN1993-1-8, 2005; ISO/DIS 12996, 2013). The main types of separation of the lap joint were included in the previously mentioned standards and their descriptions can be found in many scientific works. There are not many works about the structure analysis of the strength of joints, especially based on the criteria included in the ISO standard (2013), related to the comparison of the strength of joints formed by various joining technologies (Fig. 1). In their recent work Mucha and Witkowski (2014) presented the comprehensive analysis of the strength of clinching joints.

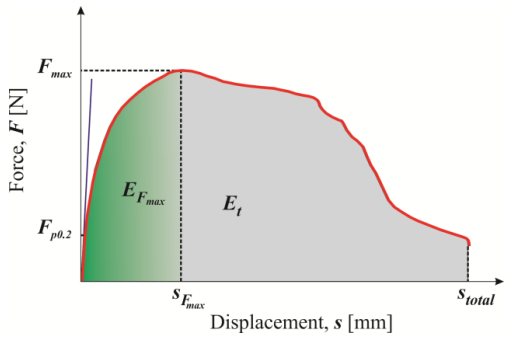

Fig. 1. Characteristic values of a load-elongation diagram for the tensile shear testing (ISO, 2013)

The performance of joints is characterized by the following properties which are of decisive importance for the mechanical

behaviour of components:

- stiffness c,
- technical yield or elastic load limit $F_{p_{0.2}}$,
- slippage load F_s,
- dissipated energy W and to a lesser extent by the maximum tensile shear load F_{max}.

The stiffness of a joint corresponds to Youngs modulus of metals or the shear modulus of an adhesive, and is a measure for the rigidity of a design or component. The slippage load F_s or the technical elastic load limit $F_{p_{0.2}}$ indicate the load a component (or joint) can withstand without suffering permanent setting or plastic deformation.

This paper presents the analysis of the structure of the joint load capacity, for riveted joints formed by various joining technologies. For the four joining systems, the specimens were prepared and tested in the tensile shear test. The influence of the sheet material on the strength of the joint during the tensile shear testing, was experimentally studied for the classic riveted lap joints and for joint with solid self-piercing rivet (SSPR).

2. EXPERIMENTAL PROCEDURE

Experimental studies were conducted to present the influence of the arrangement of the joined sheets on the load-elongation diagram for the tensile shear testing, and on the structure of the joint load capacity for joints formed by various joining technologies. The mechanism of the joint failure during the test on the strength limit was also observed. For this analysis, four types of riveted joints were used: aluminium-steel blind rivet (BR), aluminium-steel blind hermetic rivet (BHR), aluminium alloy rivet for closing up (COUR) and solid self-piercing steel rivet (SSPR) – Fig. 2 and Tab. 1. The rivets had the same diameter of the cylindrical part ($d_r = 4$ mm), while the remaining geometry was selected for the total thickness of joined sheets ($d_{tot} = 4$ mm). In the case of the rivet for closing up the appropriate chamfer was performed in the holes. The DC01 steel sheets (material number 1.0330) and the EN AW-5754 aluminium alloy sheets (material number 3.3535) in the O/H111 state were used to prepare the lap joint specimens. The yield strength of these materials are respectively 160 MPa and 85 MPa, and the ultimate tensile strength 290 MPa and 220MPa. The sheet thickness (2 mm) was the same in all joints cases. The specimens (Fig. 2) were prepared with dimensions included in ISO standard (2013). The arrangements of sheet material of the lap joints were presented in Tab. 1.

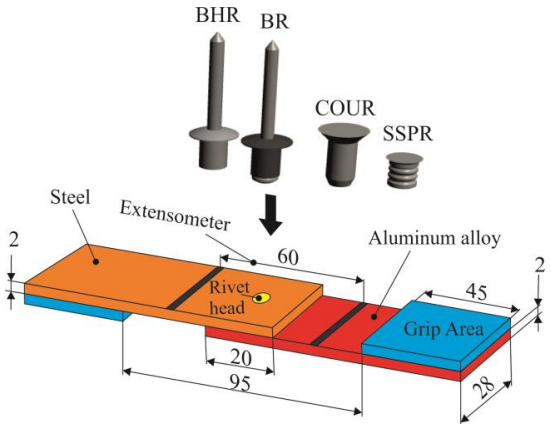

Fig. 2. Specimen dimensions and rivets denotation

In the case of the arrangements of hybrid material the primary rivet head was placed in the steel sheet (Fig. 2). The secondary rivet head was formed on the aluminium alloy sheet side. For this specimens a static tensile shear tests, with registration of the force-displacement diagrams, were performed on the Instron 3382 machine (Fig. 3). The traversing speed (the machine traverse speed) was 10 mm/min. There were seven samples prepared for each arrangement of sheets and types of rivets.

Tab. 1. The fasteners and the sheet material combinations used in riveted joints

Sheet material	Fastener			
	Blind hermetic rivet[1] (BHR)	Blind rivet[2] (BR)	Rivet for closing up[3] (COUR)	Solid self-piercing rivet[4] (SSPR)
DC01/DC01	1-1	1-2	1-3	1-4
DC01/5754	2-1	2-2	2-3	2-4
5754/5754	3-1	3-2	3-3	3-4

[1] ISO 15974:2003; [2] ISO 15978:2003; [3] ISO 1051:1999; [4] catalog number 492 000 007.900 (www.kerbkonus.com)

Fig. 3. The lap joints in the tensile shear testing

3. RESULTS

During the force loading of the lap joint the stress concentrations appear on the contact surface of the rivet and the hole (Fig. 4 a,b). The range and level of stress concentration depends on several parameters, including the clearance between the rivet and the hole. Rivet length, rivet diameter, hole diameter, and squeeze force are major parameters that affect the quality of formed rivets (Cheraghi, 2008; Szymczyk and Godzimirski, 2012). For the riveted joints, for example with blind rivet, the hole diameter is larger than the rivet diameter. The clearance between the rivet and the hole caused the rivet to tilt in the hole during the tensile shear testing (Fig. 4a). When the force load of the joint was increasing the contact surface was expanding. On the cylindrical surface of the rivet, at the hole edge, the sheet material was upset. At the same time there was a hole ovalization (Fig. 4 c). When the sheets bended the stress level decreased. The mechanism of the stress concentration was presented in Fig. 4 b. The second factor causing the stress concentration at the hole surface is the secondary bending which is a result of a different shape of the primary and secondary rivet heads. Non-uniform contact stress of the rivet is the result of the sheet deflection. During the

DOI 10.1515/ama-2015-0009

tensile shear testing of the blind rivet joints and rivet for closing up joints in EN AW-5754 aluminium alloy the hole surface was deforming. The hole surface was deforming until the maximum rivet load capacity in the transverse cross-section was reached. Then the rivet material was fractured. For the aluminium alloy sheets the greatest hole distortions were observed (Fig. 4 c).

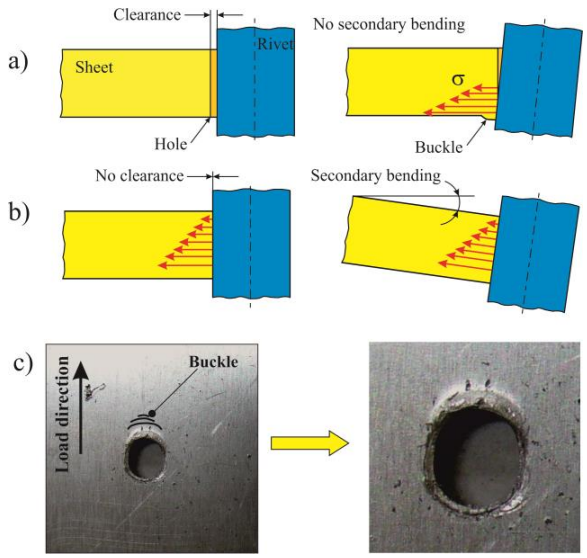

Fig. 4. The influence of the rivet on the hole surface: a) without clearance, b) with clearance, c) deformed hole in the aluminium alloy sheet after the lap separation

In the case of SSPR joint there is no clearance between the rivet and the hole made by this rivet. The rivet head is only on one side of the rivet. Hence, there is a significant rivet rotation and sheet bending to allow the rivet to pull out from the joint. Thus, after the separation of the sheets of the lap joint the rivets are rotated and the rivet holes are significantly deformed (Fig. 5 and Fig. 6). For all arrangements of sheet material similar mechanisms of destruction of riveted joints with blind rivet were observed. The tubular part of the rivet was cut in the plane of the sheet contact. For the arrangement of joints of steel sheet and aluminium alloy sheet there was no difference in the deformation around the rivet hole (Fig. 7). The deformation of the sheet material (aluminium alloy sheets) around the rivet hole was observed in the tensile shear test of the riveted joint with blind hermetic rivet (BHR) – Fig. 4c. The closed part of the tubular rivet caused different sheet pressure on one side of the joint. In the tensile shear test the rivet was slightly rotated which caused the rivet hole deformation.

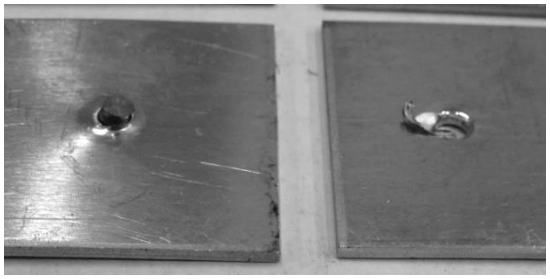

Fig. 5. SSPR joints of the aluminium alloys sheets after the laps separation

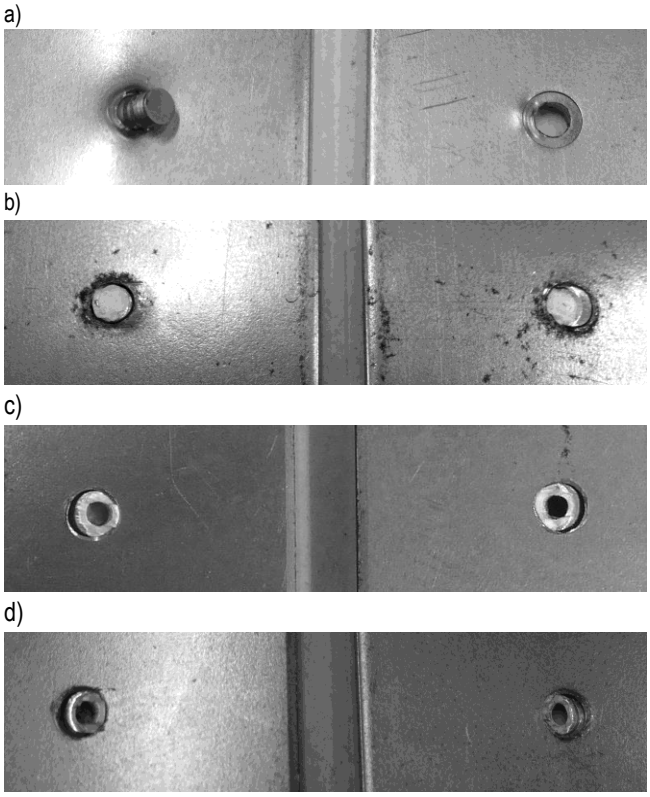

Fig. 6. Sheet metal surfaces after the tensile shear testing. Lap joints (DC01 sheet material) with: a) solid self-piercing steel rivet, b) aluminium alloy rivet for closing up, c) aluminium-steel blind hermetic rivet, d) aluminium-steel blind rivet

Fig. 7. COUR joints in the steel and aluminium alloy sheets after the laps separation

For a particular type of the rivet and for the three different arrangements of sheet material the similar values of the maximum load force were obtained (Fig. 8 a and Fig. 8 b). The different load-elongation diagrams were observed (Fig. 8 a-d). The highest values of the dissipated energy (area under the load-elongation diagram) were obtained for the EN AW-5754 aluminium alloy sheet, and the lowest values for the DC01 steel sheets (Fig. 8 a and Fig. 8 b), in the case of blind rivet joints. For the lap joints with rivet for closing up similar forms of the load-elongation diagrams were obtained. Thus the value of the dissipated energy was on the similar level for each arrangement of the sheet material. The fastener had such low strength in comparison to the joined sheets that during the tensile shear testing its strengthened material was fracturing in the same way. In the design processes of the riveted joints the condition that the sheet surface load capacity is higher than the rivet load capacity is assumed. This relation allows to predict the strength of the joint which is based on the rivet

strength condition, with respect to certain proportions between the sheet thickness and the hole diameter – the condition takes form do≤3,2t (t – the sheet thickness). If the relation is satisfied, the maximum joint load capacity can be calculated from the tensile shear condition. Designers of the thin-walled structures often have dilemmas what type of the rivet to use to maintain the appropriate joint load capacity. Sometimes they use the types of rivet which are already available in a company, without paying attention to the rivet diameter and sheet thickness. The failure mechanism presented above do not include the fourth type of riveted joints – with solid self-piercing rivet (SSPR). As the rivet punches a hole in the sheets, it needs to have considerable hardness – about 58 HRC. For this type of joints the rivet is rotated and pulled out from the bottom sheet (there is no rivet shearing) (Fig. 5 and Fig. 6 a). In the case of aluminium alloy sheets the lowest values of the shearing force were obtained (Fig. 8 d). The joint load capacity for this joints does not depends on the rivet material but on the mechanical properties of joined sheet material.

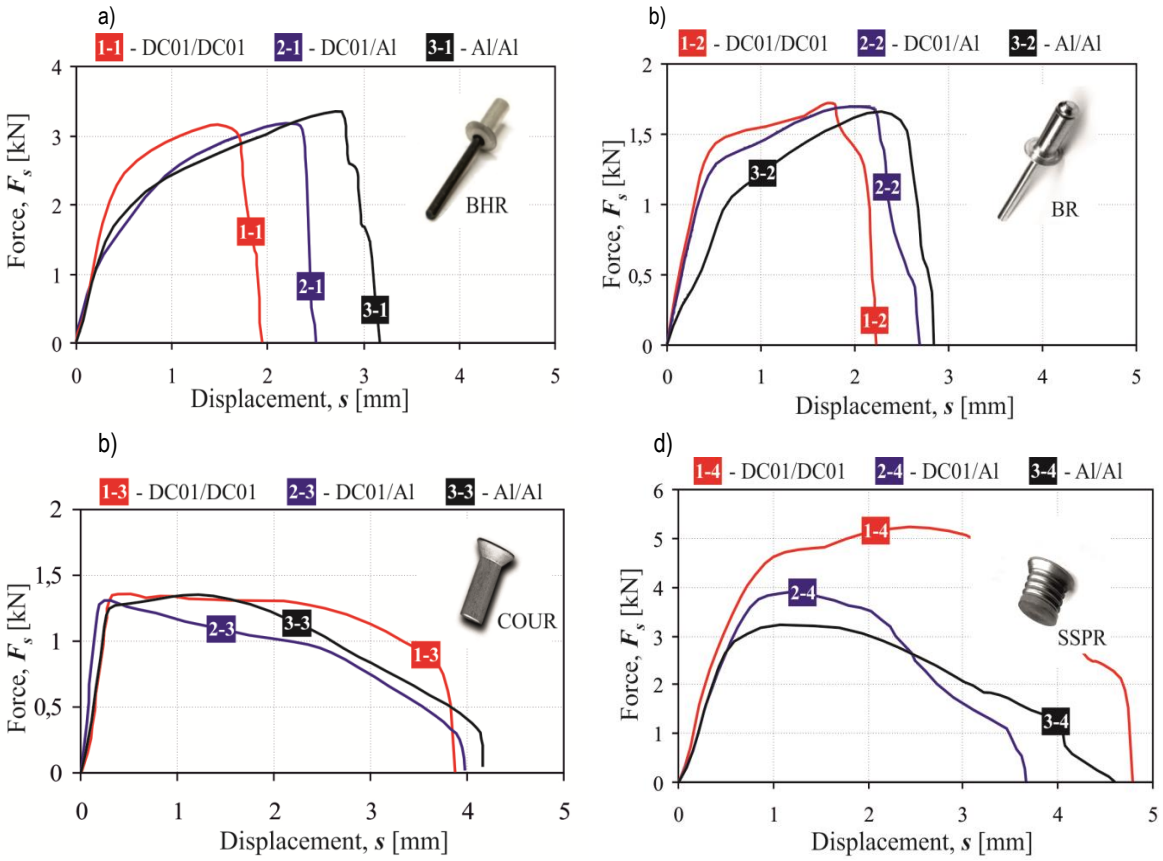

Fig. 8. Load-elongation diagrams from the lap joints tensile shear testing (BHR - blind hermetic rivet, BR - blind rivet, COUR - rivet for closing up, SSPR - solid self-piercing steel rivet)

The ability of transferring the shearing force was illustrated for the steel sheet joint specimens (Fig. 9 a). The highest value of the shearing force was obtained for the SSPR joints, and the lowest value for the aluminium alloy rivet for closing up. The joint with solid self-piercing rivet had a greater strength during the tensile shear testing than the joints with blind rivet and rivet for closing up. For the SSPR joints the differences in the shearing force were obtained for different arrangements of the sheet material (Fig. 9 b). The average value of the shearing force for the DC01 sheet material was 5.26 kN, and for the EN AW 5754 aluminium alloy sheet material was 3.42 kN. The change of the shearing force in this case was 35 %. For other joints (with blind rivet and with rivet for closing up) there were no significant differences in the strength of joints for all arrangements of sheet material (Fig. 10). To analyze the structure of the joint load capacity the selected indicators of the strength of the lap joint from the ISO standard (2013) were presented. The highest value of dissipated energy for the SSPR joint was obtained for the steel sheets material, and the lowest value for the arrangement of the hybrid sheet material (Fig. 8 d). The change of the bottom sheet material from steel to aluminium alloy resulted in the reduction of dissipated energy by 58 %.

When the arrangements of the sheet material were changed the biggest differences of strength of the joints were obtained for the SSPR joints (Fig. 10 a). For the BHR joints the values of the shearing force were similar but the dissipated energy, the displacement measured at the maximum shear load and the total displacement had different values (Fig. 10 c). In the case of joints with rivet for closing up the small differences in the values of the shearing force were obtained. Larger differences were obtained for the dissipated energy and dissipated energy of maximum shear load (Fig. 10 d).

Factor determining the use of the SSPR joints may be the economic aspects. By using of this type of the rivet joints, in the joining process, the additional preparing and finishing operations (as in the case of joining process with use of the conventional rivets) are eliminated. The SSPR joints strength is lower than strength of other joints. To increase this joints strength the joint forming force should be increased.

DOI 10.1515/ama-2015-0009

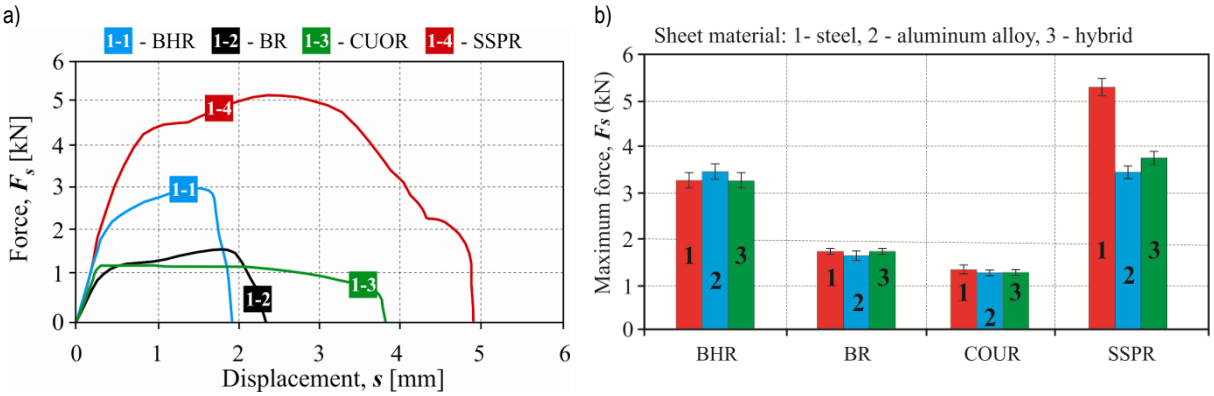

Fig. 9. Load-elongation diagrams from the steel (DC01/DC01) lap joints tensile shear testing – (a), and the mean values of the maximum shearing force – (b)

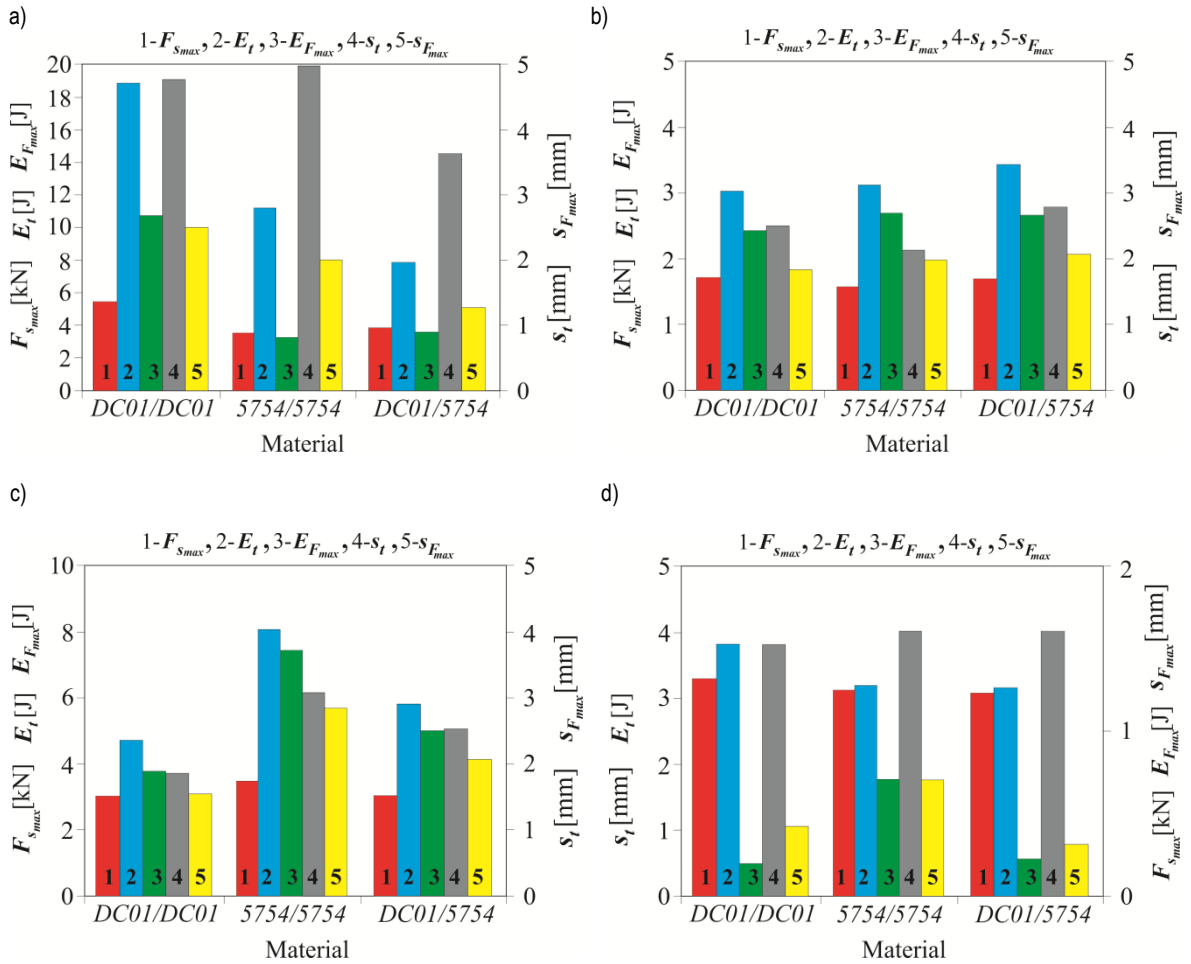

Fig. 10. The structure of the strength of the lap joint in the tensile shear test: a) SSPR, b) BR, c) BHR, d) COUR. $F_{S_{max}}$ – maximum tensile shear load; E_t – dissipated energy; $E_{F_{max}}$ – dissipated energy up to maximum shear load; S_t – total displacement; $S_{F_{max}}$ – displacement at the maximum shear load

4. SUMMARY

The joint load capacity should not be analyzed by taking into account only maximum joint force load, but by analyzing other parameters of the load-elongation diagram for the tensile shear testing. In the ISO/DIS 12996 standard the dissipated energy, for certain specific values of the load force, is proposed as a one of the joints parameter. For the three joints systems (with blind rivet, with blind hermetic rivet and with rivet for closing up) there is some dependence with similar joints strength and different dissipated energy. In the case of conventional joints (BR, BHR, COUR) the joint ability to transfer the load is depended on the fastener strength. The main factor that determines the maximum joint strength is the sheet material.

REFERENCES

1. **Cheraghi S.** (2008), Effect of variations in the riveting process on the quality of riveted joints, *International Journal of Advanced Manufacturing Technology*, 39, 1144–1155.
2. **DIN 8593-0:2003,** (2003a), *Manufacturing processes joining*, Part 0, General: classification,subdivision, terms and definitions.
3. **DIN 8593-5:2003,** (2003b), *Manufacturing processes joining*, Part 5, Joining by forming pro-cesses: classification, subdivision, terms and definitions.
4. **DIN EN ISO 14272,** (2002), *Specimen dimensions and procedure for cross tensiontesting resistance spot and embossed projection welds*.
5. **EN1993-1-8,** (2005), Eurocode 3, *Design of steel structures*, Part1–8: Design of joints.
6. **Gao S., Budde L.** (1994), Mechanism of mechanical press joining, *International Journal of Machine Tools and Manufacture*, 5, 641–657.
7. **He X., Pearson I., Young K.** (2008), Self-pierce riveting for sheet materials: state of the art, *Journal of Materials Processing Technology*, 199, 27–36.
8. **ISO/DIS 12996,** (2013), *Mechanical joining - Destructive testing of joints – Specimen dimensions and test procedure for tensile shear testing of single joints*.
9. **Kaščák L., Spišák E., Mucha J.** (2013), Clinchrivet as an alternative method to resistance spot welding, *Acta Mechanica et Automatica*, 7, 79-82.
10. **Meschut G., Janzen V., Olfermann T.** (2014), Innovative and highly productive joining technologies for multi-material lightweight car body structures, *Journal of Materials Engineering and Performance*, 23, 1515–1523.
11. **Mucha J.** (2013), The effect of material properties and joining process parameters on behavior of self-pierce riveting joints made with the solid rivet, *Materials and Design*, 52, 932–946.
12. **Mucha J.** (2014), The numerical analysis of the effect of the joining process parameters on self-piercing riveting using the solid rivet, *Archives of Civil and Mechanical Engineering*, 14, 444–454.
13. **Mucha J., Witkowski W.** (2014), The clinching joints strength analysis in the aspects of changes in the forming technology and load conditions, *Thin-Walled Structures*, 82, 55-66.
14. **Neugebauer R., Jesche F., Israel M.** (2010), Enlargement of the application range of solid punch riveting by two-piece dies, *International Journal of Material Forming*, 3, 999–1002.
15. **Neugebauer R., Todtermuschke M., Mauermann R., Riedel F.** (2008), Overview on the state of development and the application potential of dieless mechanical joining processes, *Archives of Civil and Mechanical Engineering*, 4, 51–60.
16. **Nong N., Keju O., Yu Z., Zhiyuan Q., Changcheng T., Feipeng L.** (2003), Research on press joining technology for automotive metallic sheets, *Journal of Materials Processing Technology*,1-3, 159–163.
17. **Szymczyk E., Godzimirski J.** (2012), The influence of riveting process on sheets fatigue life – the stress state analysis, *Acta Mechanica et Automatica*, 6, 74-81.
18. **Todtermuschke M.** in: **Grote K–H., Antonsson EK** (2009), Springer Handbook of Mechanical Engineering, Springer-Verlag Berlin Heidelberg, p 686–697.
19. **Voelkner W., Jesche F., Lachmann L.** (2002), Joining by forming: Newer developments, *Journal for Technology of Plasticity*, 1-2, 5–17.
20. www.kerbkonus.com (01.01.2013).

Acknowledgements: This work was prepared in the cooperation of the Department of Mechanical Engineering, Rzeszow University of Technology with AGRMAR S.A. company headquartered in Mielec. The authors thank the company employees for the assistance in the laboratory research. They also thank prof. Sieniawski (head of The Research and Development Laboratory for Aerospace Materials - LabMatPL) for making the test machine available for our tests.

DOI 10.1515/ama-2015-0010

COMPUTATIONALY SIMPLE OBSTACLE AVOIDANCE CONTROL LAW FOR SMALL UNMANNED AERIAL VEHICLES

Jakub CIEŚLUK*, Zdzisław GOSIEWSKI*, Leszek AMBROZIAK*, Sławomir ROMANIUK*

*Faculty of Mechanical Engineering, Automatic Control and Robotics Department, Bialystok University of Technology, ul. Wiejska 45C, 15-351 Białystok, Poland

jakub_ciesluk@wp.pl, z.gosiewski@pb.edu.pl, l.ambroziak@pb.edu.pl, s.romaniuk@doktoranci.pb.edu.pl

Abstract: The investigations of the system which allow to avoid obstacles by the unmanned aerial vehicles (UAV) are presented in the paper. The system is designed to enable the full autonomous UAV flight in an unknown environment. As an information source about obstacles digital camera was used. Developed algorithm uses the existing relations between the imaging system and the parameters read from the UAV autopilot. Synthesis of the proposed obstacle avoidance control law was oriented for computational simplicity. Presented algorithm was checked during simulation studies and in-flight tests.

Key words: Unmanned Aerial Vehicle, Quadrotor Control, Obstacle Avoidance, Vision Systems

1. INTRODUCTION

Unmanned Aerial Vehicles (UAVs) have wide range of applications - military and civil. Although they are able to perform a part or even the whole mission automatically, do not have the full autonomy. Autonomy level can be increased in substantial way by means of obstacle avoidance systems.

In the past, graph methods (Shojaeopour, 2010) and potential fields (Khatib, 1985) approach were utilized to the path planning in autonomous navigation. Nowadays UAVs obstacle avoidance problems are mainly resolved by the usage of fuzzy logic (Cieśluk and Gosiewski, 2012, 2013; Guzel and Bicker, 2011) and methods of predictive control (Wang, 2001). Devices used as the obstacle detection sensors are ultrasonic range finders (Modi et al., 2001), laser scanners (Kownacki, 2013), lidars (Sabatini et al., 2014) and vision sensors (ccd cameras (Meier et al., 2012), optical flow sensors (Herrise et al., 2008)). Despite first three of mentioned sensors have fairly good range measurements quality, their mass is relatively large and they have low output frequency (Modi et al., 2001).

The following paper presents the obstacle avoidance control law based on the fuzzy logic controller. Input to the fuzzy logic controller is the information acquired from the cameras. Obtained information from vision system can be easily adopted to fuzzy logic rules. Proposed algorithm is based on a small number of input parameters, what results in low requirements of computational power. Main goal of the presented studies was simulation tests. During this tests preliminary process of the control surface selection was performed. Moreover presented control algorithm was checked during in-flight tests.

2. RESEARCH OBJECT

2.1. Quadrotor

As control object we have chosen quadrotor - vertical take-off and landing (VTOL) object with very specific dynamics. Quadrotors are often used as a platform for formation flying control framework, surveillance and reconnaissance purposes, aerial surveys for agriculture, traffic monitoring etc. They can hover above the desired waypoint and in place can change the motion direction. It is simple to separate navigation from orientation in quadrotor motion. Simplified dynamics model of this objects is described in the next subsection.

2.2. Mathematical model

Methods described in the work of authors (Cieśluk and Gosiewski, 2013; Soumare et al., 2002) allow obstacle detection in the robot's surroundings. However, in order to avoid an obstacle, location itself is insufficient. The adequate control procedure is required, which take into account data read from the obstacle localization sensor. Thus, in order to present the idea of control algorithm used in the obstacle avoidance flight mode, mathematical model employed in the quadrotor research is used.

Determination of the dynamic model of the quadrotor required linking together of the two coordinate systems. First coordinate system is associated with the object – x_B, y_B, z_B while the other one is associated with the Earth – x, y, z (Fig. 1). Quadrotor center of gravity is the origin of coordinate system x_B, y_B, z_B.

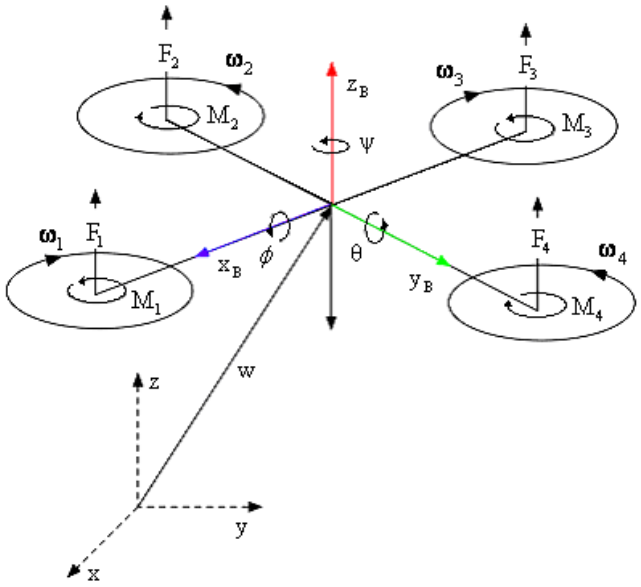

Fig. 1. Quadrotor coordinates frame

Description of the variables containing position and orientation data of the quadrotor in 3D space is described underneath:

$$\begin{bmatrix} x \\ y \\ z \end{bmatrix} = \begin{bmatrix} longitude \\ latitude \\ altitude \end{bmatrix}, \begin{bmatrix} \phi \\ \theta \\ \psi \end{bmatrix} = \begin{bmatrix} roll\ \ angle \\ pitch\ \ angle \\ yaw\ \ angle \end{bmatrix} \tag{1}$$

Vector containing data of linear and angular quadrotor position related to Earth coordinate system $x, y,$ is specified as follows:

$$q = [x\ y\ z\ \phi\ \theta\varphi]^T \tag{2}$$

Vector comprising linear velocities and angular rates components of quadrotor in the x_B, y_B, z_B system is defined below:

$$\dot{q_B} = [u\ v\ z\ p\ q\ r]^T \tag{3}$$

Relations between two corresponding coordinate systems can be written in the following way based on Mellinger et al. (2012) and Hoffmann et al., (2011):

$$\begin{bmatrix} \dot{x} \\ \dot{y} \\ \dot{z} \end{bmatrix} = R_B \begin{bmatrix} u \\ v \\ n \end{bmatrix} \triangleq \begin{bmatrix} c_\psi c_\theta & -s_\psi c_\phi + c_\phi s_\theta s_\phi & s_\psi s_\phi + c_\psi s_\theta c_\phi \\ s_\psi c_\theta & c_\psi c_\phi + s_\phi s_\theta s_\psi & -c_\psi s_\phi + s_\psi s_\theta c_\phi \\ -s_\theta & c_\theta s_\phi & c_\theta c_\phi \end{bmatrix} \begin{bmatrix} u \\ v \\ n \end{bmatrix},$$
$$\begin{bmatrix} \dot{\phi} \\ \dot{\theta} \\ \dot{\psi} \end{bmatrix} = T_B \begin{bmatrix} p \\ q \\ r \end{bmatrix} \triangleq \begin{bmatrix} 1 & s_\phi t_\theta & c_\phi t_\theta \\ 0 & c_\phi & -s_\phi \\ 0 & s_\phi / c_\theta & c_\phi / c_\theta \end{bmatrix} \begin{bmatrix} p \\ q \\ r \end{bmatrix} \tag{4}$$

$$\dot{q} = \begin{bmatrix} R_B & 0_{3\times3} \\ 0_{3\times3} & T_B \end{bmatrix} \dot{q}_B,$$

where: c_θ, s_θ, t_θ are shortened notation of $\cos(\theta), \sin(\theta), \tan(\theta)$, similarly for the remaining angles ϕ and ψ. Vector w in Fig. 1 describes the position of mass center in the global coordinate system. The gravitation force in the $-z$direction and the motors thrust F_i in the z_b direction are the forces acting on the quadrotor. Equation presenting the acceleration of the mass center is described as follows:

$$m\ddot{w} = \begin{bmatrix} 0 \\ 0 \\ -mg \end{bmatrix} + R_B \begin{bmatrix} 0 \\ 0 \\ \sum F_i \end{bmatrix} \tag{5}$$

Every motor generates torque M_i, that is parallel to the propellers rotation plane. Rotor 1 and 3 have clockwise direction of rotation while 2 and 4 have counterclockwise direction. Motor torques have directions opposing to the propellers rotation one. Thus, $M_1$and M_3 have $-z_b$ direction while M_2,M_4, z_b direction. The length of each of the quadrotor arms is l. Moment of inertia matrix related to the mass center along the $x_B y_B\ z_B$ axis is I. Angular acceleration described by Euler equation is following:

$$I \begin{bmatrix} \dot{p} \\ \dot{q} \\ \dot{r} \end{bmatrix} = \begin{bmatrix} l(F_4 - F_2) \\ l(F_3 - F_1) \\ -M_1 + M_2 - M_3 + M_4 \end{bmatrix} - \begin{bmatrix} p \\ q \\ r \end{bmatrix} \times I \begin{bmatrix} p \\ q \\ r \end{bmatrix} \tag{6}$$

Having regard to the (5) and (6) quadrotor dynamic system equations are received:

$$\begin{cases} \ddot{x} = \left(s_\psi s_\phi + c_\psi s_\theta c_\phi\right) \frac{u_1}{m} \\ \ddot{y} = \left(-c_\psi s_\phi + s_\psi s_\theta c_\phi\right) \frac{u_1}{m} \\ \ddot{z} = -g + \left(c_\theta c_\phi\right) \frac{u_1}{m} \\ \dot{p} = \frac{I_{yy} - I_{zz}}{I_{xx}} qr + \frac{u_2}{I_{xx}} \\ \dot{q} = \frac{I_{zz} - I_{xx}}{I_{yy}} pr + \frac{u_3}{I_{yy}} \\ \dot{r} = \frac{I_{xx} - I_{yy}}{I_{zz}} pq + \frac{u_4}{I_{zz}} \end{cases} \tag{7}$$

The description of system input variables u_i will be presented in the next section.

2.3. Orientation control

Linearization of the quadrotor equations of motion can be made in the properly chosen equilibrium point. Selected equilibrium point parameters are:

$$w = w_0, \theta = \phi = 0,\ \psi = \psi_0\ ,\ \dot{w} = 0, \dot{\phi} = \dot{\theta} = 0\ \dot{\psi} = 0.$$

Taking assumption that roll and pitch angles of the system are very small we can write that:

$$cos\phi \approx 1,\ cos\theta \approx 1,\ sin\phi \approx \phi,\ sin\theta \approx \theta.$$

Nominal force generated by motor-propeller systems in a given state is defined as follows:

$$F_{i,0} = \frac{mg}{4} \tag{8}$$

Presented model of the quadrotor is symmetrical, therefore $I_{xx} \approx I_{yy}$, so according to equation (6) we can write:

$$\begin{aligned} I_{xx}\dot{p} &= u_2 - qr(I_{zz} - I_{yy}) \\ I_{yy}\dot{q} &= u_3 - pr(I_{xx} - I_{zz}) \\ I_{zz}\dot{r} &= u_4 \end{aligned} \tag{9}$$

Resultant torque values are determined by simple, proportional-differentiating control laws, presented below:

DOI 10.1515/ama-2015-0010

$$u_{2,des} = k_{p,\phi}(\phi_{des} - \phi) + k_{d,\phi}(p_{des} - p)$$
$$u_{3,des} = k_{p,\theta}(\theta_{des} - \theta) + k_{d,\theta}(q_{des} - q) \quad (10)$$
$$u_{4,des} = k_{p,\psi}(\psi_{des} - \psi) + k_{d,\psi}(r_{des} - r)$$

Each of the rotors during operation has a fixed angular velocity ω_i and a vertical force is generated in accordance with the following formula:

$$F_i = b\omega_i^2 \quad (11)$$

while torque is determined by term:

$$M_i = d\omega_i^2 \quad (12)$$

Important aerodynamic parameters describing the behavior of rotating propellers in the air are taken into account during the calculations. Those parameters are: $b\ [\mathrm{N/rpm^2}]$ which is an aerodynamic longitudinal coefficient (thrust) and $d\ [\mathrm{Nm/rpm^2}]$ describing air resistance coefficient of the rotating body. Designation of these aerodynamic parameters is done by combining the momentum theory and the theory of the propeller thoroughly described in Bresciani (2008) according to the relations:

$$b = \frac{T_{BET}}{\omega_i^2} \quad (13)$$

$$d = \frac{Q_{BET}}{\omega_i^2} \quad (14)$$

where: longitudinal force $T_{BET}\ [\mathrm{N}]$ is found by the integration of the vertical forces acting on all sections of the blade elements. Furthermore, the torque of the propeller $Q_{BET}\ [\mathrm{Nm}]$ is found by integrating the horizontal forces multiplied by the moment arm on all sections of the blade components.

Setpoint value of the motor angular speed is limited to the range from 1200rpm to 8000rpm. Preset speeds of the individual motors $\omega_{i,des}^2$, can be find from the set resultant force value's data $u_{1,des}$ and moments ($u_{2,des}$, $u_{3,des}$, $u_{4,des}$) by transforming following equation:

$$\begin{bmatrix} u_{1,des} \\ u_{2,des} \\ u_{3,des} \\ u_{4,des} \end{bmatrix} = \begin{bmatrix} b & b & b & b \\ 0 & -bl & 0 & bl \\ -bl & 0 & bl & 0 \\ -d & d & -d & d \end{bmatrix} \begin{bmatrix} \omega_{1,des}^2 \\ \omega_{2,des}^2 \\ \omega_{3,des}^2 \\ \omega_{4,des}^2 \end{bmatrix} \quad (15)$$

2.4. Position control

To present the idea of the UAV position control, some simplifications were adopted. They result from taking into account the motion (lifting) of the quadrotor to (x, y, z_B) position. It is possible, consequently to assume that tracked yaw angle is $\psi_T(t) = \psi_0$.

The linearization of equation (5) allows us to establish the relation between specified linear acceleration, roll and pitch angles as follows:

$$\ddot{w}_{1,des} = (\phi_{des}\sin\psi_T + \theta_{des}\cos\psi_T)g$$
$$\ddot{w}_{2,des} = (-\phi_{des}\cos\psi_T + \theta_{des}\sin\psi_T)g \quad (16)$$
$$\ddot{w}_{3,des} = \frac{u_{1,des}}{m}$$

Utilization of the presented above dependencies allows to provide the setpoints of the pitch and roll angles for the needs of the quadrotor orientation control (10) (15). The value of force setpoint $u_{1,des}$ is determined in the following way:

$$\phi_{des} = (\ddot{w}_{1,des}\sin\psi_T - \ddot{w}_{2,des}\cos\psi_T)/g$$
$$\theta_{des} = (\ddot{w}_{1,des}\cos\psi_T + \ddot{w}_{2,des}\sin\psi_T)/g \quad (17)$$
$$u_{1,des} = m\ddot{w}_{3,des}$$

To determine the flight path in the 3D space, a method from involving determination of the nearest point of the trajectory w_T for the current position w is utilized. Position and velocity errors are defined respectively:

$$e_p = w_T - w$$
$$e_v = \dot{w}_T - \dot{w} \quad (18)$$

The calculation of the desired acceleration $\ddot{w}_{i,des}$ is carried out in the PD controller feedback loop in following way:

$$\ddot{w}_{i,zad} = k_{p,i}e_{i,p} + k_{d,i}e_{i,v} \quad (19)$$

Ultimately, using equation (19) it is possible to determine desired values of roll and pitch angles and $u_{1,des}$ according to equation (17).

2.5. Obstacle avoidance controller

Quadrotor control system has two independent feedback control loops (Fig. 2). The inner control loop is responsible for quadrotor stabilization, while the outer loop is associated with the UAV position control. The inner loop uses the data read from the three axis accelerometer and gyroscope for the control of the roll, pitch and yaw angles (ϕ, θ, ψ). This loop works with 200 Hz frequency. On the other hand the outer loop, utilizes the quadrotor GPS position and GPS velocity data to control the flight.

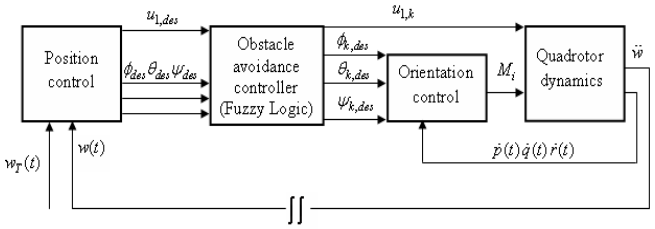

Fig. 2. A block diagram of the quadrotor control system

The obstacle avoidance system includes an additional block (fuzzy logic controller) in the inner loop. This block is responsible for producing the corrections k_φ, k_θ to the desired values of navigational angles (φ_{des}, θ_{des}). These adjustments are described in the following way:

$\Phi_{k,des} = \Phi_{des} \pm k_\Phi$ – correction of the desired rolling angle,
$\theta_{k,des} = \theta_{des} \pm k_\theta$ – correction of the desired pitching angle.

Corrections k_T to the throttle signal are calculated with following simplified formula:

$$k_T = 30\% \cdot u_{1,des} \quad (20)$$

$$u_{1,k} = u_{1,des} + k_T \quad (21)$$

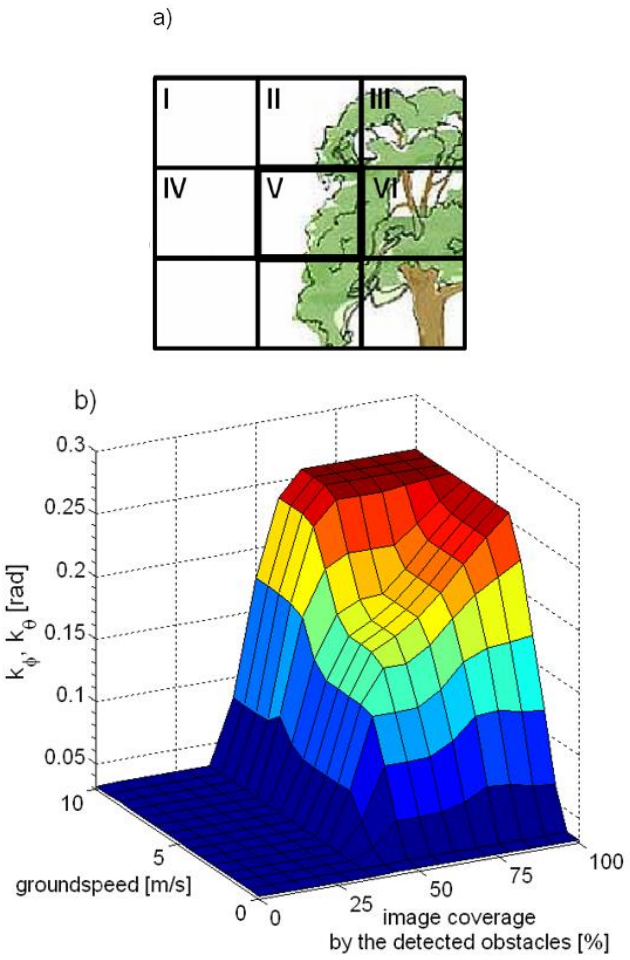

Fig. 3. Obstacle detection a) Image sections definition, b) sample fuzzy logic control surface

Signal of desired throttle is calculated as follows:

Image obtained by the vision system can be shown schematically in Fig. 3a. Whole image is divided to 6 main sections. Camera is oriented always in flight direction of the quadrotor. Vision algorithm analyze only the center of the image (section V on the Fig.3a). Fig.3b represents surface whereby corrections k_φ, k_θ are calculated. Control signal is produced basing on vehicle ground speed and coverage of the section V (center of the analyzed image) by the detected obstacle.

Detection of obstacle in the section V of the image, starts collision avoidance procedure and next, sequent image sections are analyzed and processed. The correction values k_φ, k_θ, k_T are determined based on information from analyzed sequent image sections. In the situation when the obstacle free space is detected in the IV and VI sections (Fig. 3a), the correction k_ϕ with the sign appropriate to the maneuver direction is produced according to modeled control surface (Fig. 3b). For image sections I and III, k_T is determined with (20) and also appropriately signed k_Φ is produced with control surface from Fig. 3b also. In the case of section II the correction k_T is overwritten only. The last possibility is when in the whole image is no obstacle free space. In this case, correction k_T is obtained with equation (20) and k_θ is calculated in following manner:

$$\theta_{des} \pm k_\theta \approx 0 \quad (22)$$

what causes a vertical ascent of the UAV. The vertical ascent is continuing until the obstacle free space is localized in the image. Above procedures and control rules have good performance in the open space and during outdoor flights. In the case of indoor flights it is needed to use additional correction to yaw angle desired value ψ_{des}.

3. SIMULATION RESULTS

Basing on equations (7) the simulation model of the quadrotor was build in Matlab/Simulink software with the usage of specialized toolboxes like Control System, Flight Dynamics and Control, Aerospace and Fuzzy Logic. The aim of the simulation research was a preliminary selection of the parameters that are used in the autonomous mission control system of the unmanned aerial vehicle. Dynamically changing simulation environment has been programmed as the model of the virtual reality written in VRML (Virtual Reality Modelling Language). Virtual simulation world reproduces the area in which the in-flight tests were to be conducted. This will allow the comparison of the results obtained from the simulation with the measurements taken directly from the conducted experiment. The simplified model of image processing methods was approved in the simulation tests. Brightness control system described in Cieśluk and Gosiewski (2013, 2014), that is essential during in-flight tests, wasn't used during simulation studies. Whereas the law of UAV position control, autopilot operating modes and the area describing the obstacles were modeled. Image used by the obstacle avoidance algorithm is continuously extracted from a moving quadrotor in 3D space. During simulation tests image refresh rate is set at 10 fps. The flight simulation screen is presented in Fig. 4. The graphs show the currently generated flight path and the result of vision obstacle detection algorithm.

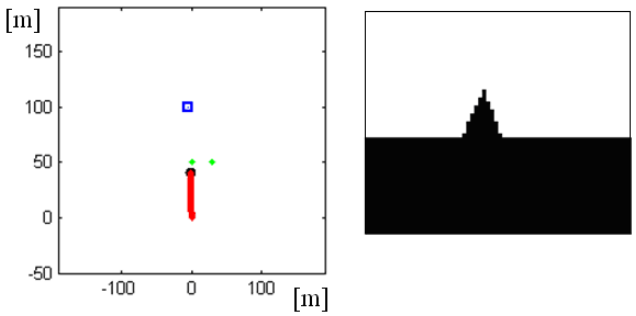

Fig. 4. Simulation studies application (UAV flight path - left side, output of the obstacle detection algorithm (processed image) - right side)

Simulation study was conducted for the model which reflects the area of out-door field tests. Fig. 5 presents the pictures taken during the proving ground studies.

DOI 10.1515/ama-2015-0010

Fig. 5. View of the airfield

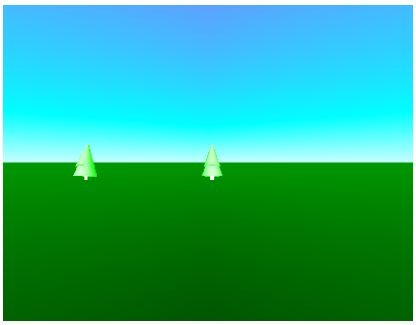

Fig. 6. Field area modeled in the VRML (Virtual Reality Modelling Language)

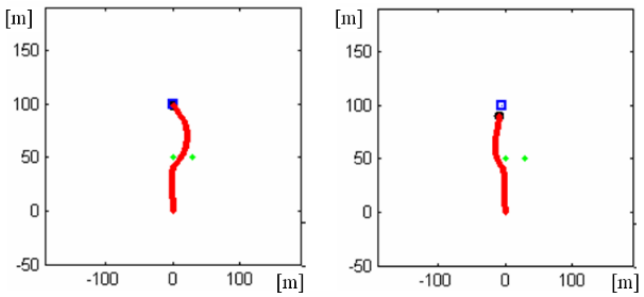

Fig. 7. Different quadrotor reactions depending on image search algorithm configuration

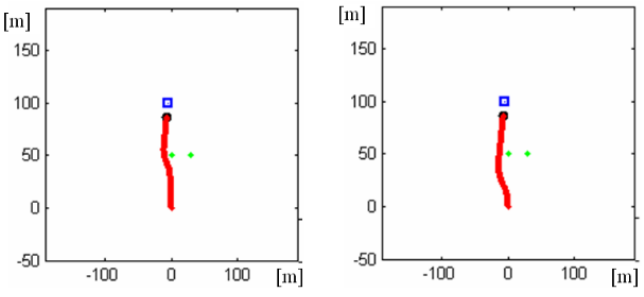

Fig. 8. Quadrotor flight paths for different control surfaces

The influence of changes in the sequence of the image controlled areas to the direction of the maneuver is presented in Fig. 7. Edges of the map show the position expressed in meters. Green points represents the obstacles, while the blue square is the quadrotor destination waypoint. Analogously the red thick line shows the travelled path. Example shows that the direction of the maneuver is highly dependent on the established criteria for image search of obstacle-free sections. During simulation tests, different forms of the control surface were tested. Results for different types of the control surfaces are presented in the Fig. 8. In simulation research the best possible shape of the control surface was chosen, taking into account quadrotor reaction aggressiveness.

4. IN-FLIGHT TESTS

The most important step in an obstacle avoidance controller synthesis is in-flight testing. At the same time, it is the most risky part of the research. The study has been carried out on the airfield. Own build quadrotor airframe with ArdupilotMega 2.0 was used as a testing object. ArdupilotMega 2.0 runs custom control application. The image processing algorithms are implemented on a small, smart camera with auto iris lens (Cieśluk and Gosiewski, 2014) and mass of 220g. Image processing algorithm was working with 42 Hz frequency.

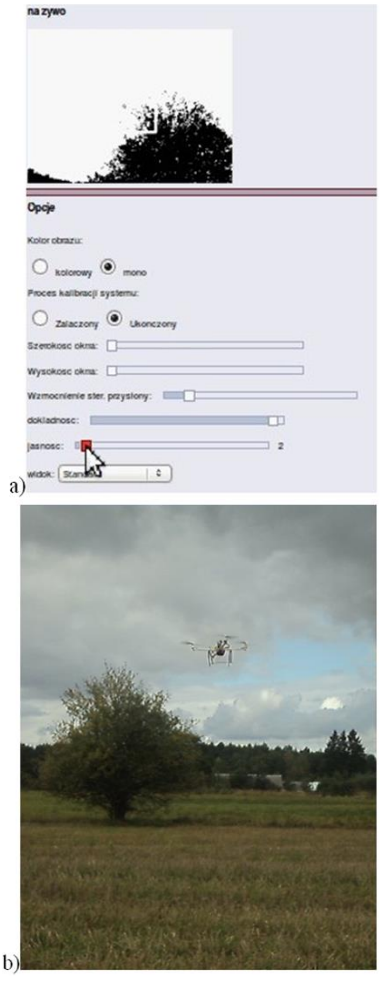

Fig. 9. Field experiments: a) picture from the webserver of vision system b) photo of the tree as an obstacle (made during the field test)

The quadrotor was also equipped with a wireless WiFi router (90g) and LiPo battery 4600mAh. Total mass of all components was less than 400g. Trajectory was planned to meet on its way at least one obstacle. Tests were carried out for short range missions to keep constant radio contact with the quadrotor. The Fig. 9 presents quadrotor during in-flight tests and the vision system webserver.

In the Fig.10 quadrotor flight paths obtained during in-flight tests are presented. Flight paths are marked with dark blue lines on the airfield satellite view from ground control station. Preselected flight paths should be straight, but in case of obstacle vision system acting, desired path was corrected to amount of obstacle appearance.

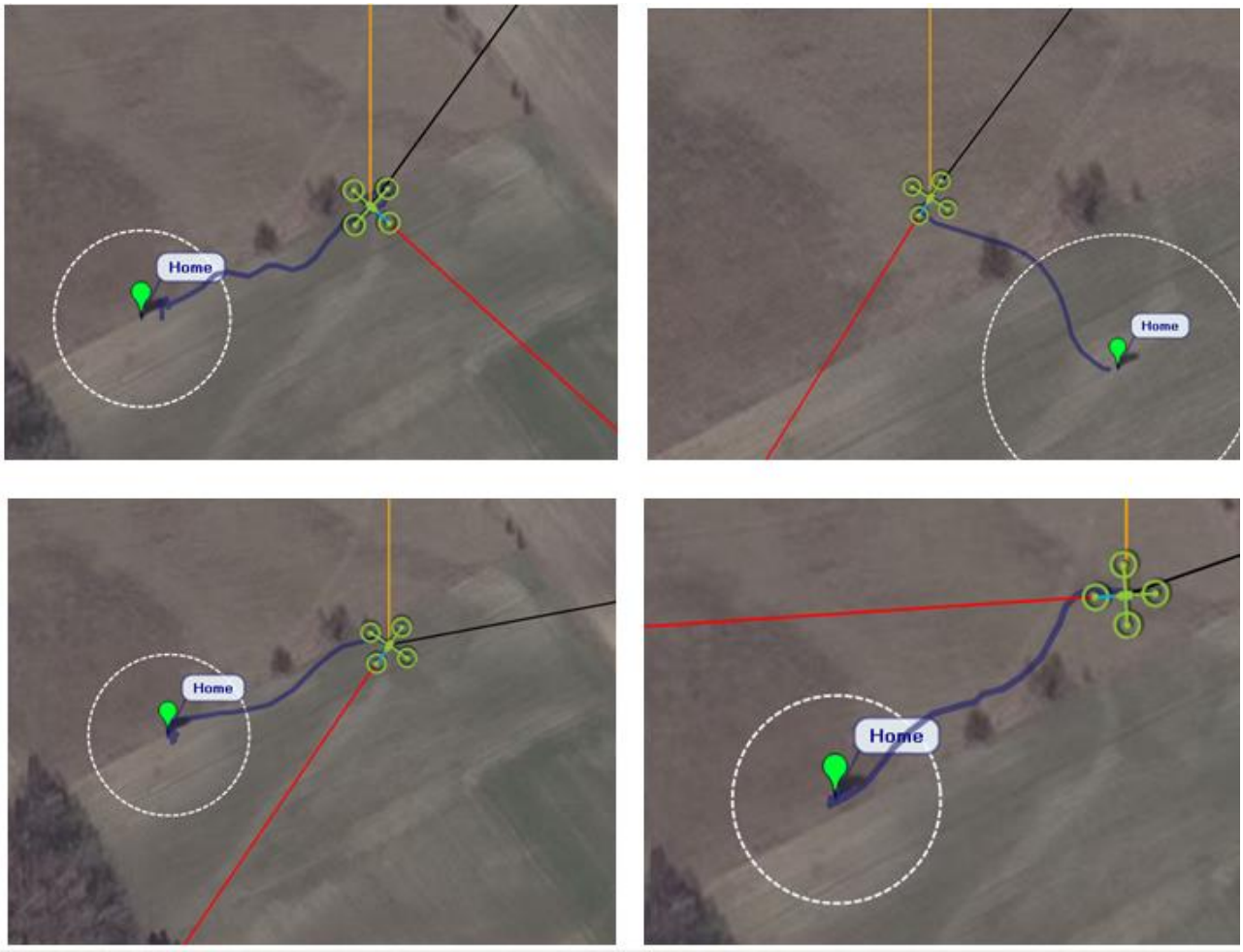

Fig. 10. Quadrotor flight paths during in-flight tests
(based on the satellite maps of the investigated area)

5. CONCLUSIONS AND FUTURE WORK

Proposed vision obstacle controller connected with fuzzy logic technique to control surface modeling is an effective method of controlling small UAVs autonomously. Obtained during simulation studies and in-flight tests results indicate that vision obstacle avoidance system can be used in the real applications but we have to take into account that experimental tests were properly arranged (straight path line with one, clear, explicit obstacle). It will be much more difficult to use this system and algorithm in the dynamic environment, bad weather conditions and to small obstacles. Several unsuccessful attempts were recorded, however taking them as the base it is hard to say, whether the obstacle detection system was guilty of the failure.

Further works will be strictly associated with the operation effectiveness improvement of the obstacle detection methods presented in the work. Consecutive tests will be conducted for more complex missions.

REFERENCES

1. **Bresciani T.** (2008), *Modelling, Identification and Control of a Quadrotor Helicopter*, Master's thesis, Lund University, Sweden.
2. **Cieśluk J., Gosiewski Z.** (2012), Vision sky detection system used to obstacle avoidance by unmanned aerial, Mechanics in Aviation XV, 2012, pp. 509-523.
3. **Cieśluk J., Gosiewski Z.** (2013), A Stereovision System for Real Time Obstacle Avoidance by Unmanned Aerial Vehicle, *Solid State Phenomena*, Vol 198, pp. 159-164.
4. **Cieśluk J., Gosiewski Z.** (2014), Image brightness control method used for obstacles avoidance by unmanned aerial vehicle, *Mechanics in Aviation*, 16, 2014, 279-290.

5. **Guzel M. S., Bicker R.** (2011), *Vision Based Obstacle Avoidance Techniques, Recent Advances in Mobile Robotics*, Dr. AndonTopalov (Ed.), InTech, UK, 83-101.
6. **Herisse B., Russotto, F.-X., Hamel, T., Mahony, R.** (2008), Hovering flight and vertical landing control of a VTOL Unmanned Aerial Vehicle using Optical Flow, *IEEE International Conference on Intelligent Robots and Systems*,pp. 801 – 806.
7. **Hoffmann G. M., Huang H., Waslander S. L, Tomlin C. J.** (2011), Precision flight control for a multi-vehicle quadrotor helicopter testbed, *Control Engineering Practice*, Vol. 19, 1023–1036.
8. **Khatib O.** (1985), The Potential Field Approach and Operational Space Formulation in Robot Control, *Proc. Fourth Yale Workshop on Applications of Adaptive Systems Theory*, Yale University, New Haven, Connecticut, 208-214.
9. **Kownacki C.** (2013), Successful Application of Miniature Laser Rangefinders in Obstacle Avoidance Method for Fixed Wing MAV, *International Journal of Robotics and Automation*, 10.2316/ Journal.206.2013.3.206-3936.
10. **Meier L., Tanskanen P., Heng L., Lee G. H., Fraundorfer F., Pollefeys M.** (2012), PIXHAWK: A micro aerial vehicle design for autonomous flight using onboard computer vision, *Autonomous Robots*, 33 (1-2), 21-39.
11. **Mellinger D., Michael N., Kumar K.** (2012), Trajectory generation and control for precise aggressive maneuvers with quadrotors, *The International Journal of Robotics Research*, Vol. 31, No. 5, 664-674.
12. **Modi S. B., Chandak P., Murty V. S., Hall E. L**. (2001), Comparison of three obstacle-avoidance methods for a mobile robot, *Proc. SPIE 4572, Intelligent Robots and Computer Vision XX: Algorithms, Techniques, and Active Vision*, pp. 290-297.
13. **Sabatini R., Gardi A., Richardson M. A.** (2014), LIDAR Obstacle Warning and Avoidance System for Unmanned Aircraft, *International Journal of Mechanical, Aerospace, Industrial and Mechatronics Engineering*, Vol. 8, No 4, 702-713.
14. **Shojaeipour S.** (2010), Webcam-based mobile robot path planning using Voronoi diagrams and image processing, *Proceedings of the 9th WSEAS international conference on Applications of electrical engineering*, World Scientific and Engineering Academy and Society (WSEAS), Penang, Malaysia, 151-156.
15. **Soumare S., Ohya A., Yuta S.** (2002), Real-Time Obstacle Avoidance by an Autonomous Mobile Robot using an Active Vision Sensor and a Vertically Emitted Laser Slit, *Intelligent Autonomous Systems*, 7, 301-308.
16. **Wang L.** (2001), Continuous time model predictive control design using orthonormal functions, *International Journal of Control*, Vol. 74(16), 1588-1600.

Co-authors Jakub Cieśluk, Leszek Ambroziak and Sławomir Romaniuk are a beneficiary of the project „Scholarships for PhD Students of Podlaskie Voivodeship". The project is co-financed by European Social Fund, Polish Government, and Podlaskie Voivodeship.

ABSTRACTS

Alireza Azimi, Mohammadreza Azimi, Amirhossein Javanfar
Application of HPM To Find Analytical Solution of Coette Flow with Variable Viscosity

In this paper, the couette flow of fluid with variable viscosity is studied analytically by using Homotopy Pertubation Method (HPM). At first the basic idea of Homotopy Pertubation Method (HPM) is presented. The mathematical formulation and application of HPM to nonlinear problem are presented in section three. In order to check the validity of solution the analytical results are compared with exact ones for various numerical cases. The good agreement between exact method and Homotopy Pertubation Method has been assures us about the solution accuracy.

Arkadiusz Trąbka
The Influence of Clearances in a Drive System on dynamics and Kinematics of a Telescopic Crane

The paper presents the results of numerical analyses that were carried out in order to evaluate how a change in a size of a clearance in a slewing motion drive system of a telescopic crane influences the movement of a load and the dynamic loads of a structure. A computational model was developed based on a real structure of an experimental crane by using the ADAMS soft-ware. The analyses showed that a circumferential clearance at the output of a reduction gear, which is less than $1°$, does not adversely affect the precision of the load movement. An excessive clearance leads to losing fluidity of a body slewing motion and to changes in the trajectory of the load.

Dariusz Szpica, Jarosław Czaban, Piotr Banaszuk, Emil Weresa
The Diesel and the Vegetable oil Properties Assessment in terms of Pumping Capability and Cooperation with Internal Combustion Engine Fuelling System

In the paper, the results of preliminary diesel and vegetable oil research were shown, the subject of which were directly intended to be the fuel for powering compression ignition engines. In the times of climate protection and more strict standards concerning combustion gas emissions, the fuel production and transportation process became an important aspect. Decentralization of this process and enabling fuel obtaining directly from cultivation (oleaginous plants) let limit the global CO2 emission. This is why the preliminary assessment of two fuel sorts properties was attempted, on one side, the basic one, which is the diesel, on the other side - vegetable oil. Prior to subjecting the compression ignition engine to the process of adaptation to vegetable fuelling, the properties of the fuel responsible for pumping should be assessed (mainly viscosity) and friction nodes cooperation (lubricity). The first of researched parameters is the base to elaborating the system of engine controlling algorithm or the range of changes in construction of powering system. The second one is the wear issue - object fitness and repairing overhauls.

Jerzy Tomaszewski, Jacek Rysinski
Diagnostics of Gears and Compressors by Means of Advanced Automatic System

In the present paper, the diagnostics problems of gears and air-compressors are discussed. The diagnostics has been performed by means of wireless system WiViD. This system is a unique design solution, in which several functions are divided and performer by two separate devices. The mentioned device functions are as follows: data handling, processing, their analysis and presentation. In the paper, own measurement procedures were created, checked and presented. The evaluation of technical conditions of some devices was done based upon the registered diagnostic symptoms, which were compared with the allowable limits.

Dmytro Fedorynenko, Sergiy Boyko, Serhii Sapon
The Search of the Spatial Functions of Pressure in Adjustable Hydrostatic Radial Bearing

The analysis of spatial functions of pressure considering the geometrical deviations and the elastic deformation of conjugate surace have been considered. The analysis of spatial functions of pressure is performed by the finite element method. The difference of the size of pressure in a tangential direction of a pocket of a support under various service conditions has been investigated. A recommendation for improving of operational characteristics in regulated hydrostatic radial bearing has been developed.

Andriy Styahar, Yarema Savula
On the Convergence of Domain Decomposition Algorithm for the Body with Thin Inclusion

We consider a coupled 3D model that involves computation of the stress-strain state for the body with thin inclusion. For the description of the stress-strain state of the main part, the linear elasticity theory is used. The inclusion is modelled using Timoshenko theory for shells. Therefore, the dimension of the problem inside the inclusion is decreased by one. For the numerical solution of this problem we propose an iterative domain decomposition algorithm (Dirichlet-Neumann scheme). This approach allows us to de-couple problems in both parts and preserve the structure of the corresponding matrices. We investigate the convergence of the aforementioned algorithm and prove that the problem is well-posed.

Ewa Och
Solving Nonlinear Thermal Problems of Friction By Using Method of Lines

One-dimensional heat conduction problem of friction for two bodies (half spaces) made of thermosensitive materials was considered. Solution to the nonlinear boundary-value heat conduction problem was obtained in three stages. At the first stage a partial linearization of the problem was performed by using Kirchhoff transform. Next, the obtained boundary-values problem by using the method of lines was brought to a system of nonlinear ordinary differential equations, relatively to Kirchhoff's function values in the nodes of the grid on the spatial variable, where time is an independent variable. At the third stage, by using the Adams's method from DIFSUB package, a numerical solution was found to the above-mentioned differential equations. A comparative analysis was conducted (Och, 2014) using the results obtained with the proposed method and the method of successive approximations.

Radovan Hudák, Viktória Rajťúková, Jozef Živčák
Automatization of Contact Pressure Measurement between Trunk Orthosis and Patient's Body Using a Matrix Tactile Sensor

Trunk orthosis affects trunk by a corrective-pressure mode with an objective to correct deformities (e.g. scoliosis). The effectiveness of this function depends on various factors, i.e. correct orthosis manufacture, correct application to patients and regular pressure corrective effect control. All these factors can be monitored by a system for measurement and evaluation of the contact pressure between the instrument and trunk in a real time and also by a so called "off line" system data recording. Presented article describes the application of made-to-measure sensor system TACTILUS (Sensor Products, USA) in different regimes (ambulance – A, home – H, combined – HA and multi-sensory ambulance – MA regime), testing of chosen static and dynamic matrix tactile sensor (MTS) parameters and results of the testing application between orthosis and patients' trunks.

Jacek Mucha, Waldemar Witkowski
The Structure of the Strength of Riveted Joints Determined in the Lap Joint Tensile Shear Test

The article presents the analysis of the structure of the load capacity of riveted joints. For the four joining systems the lap joint specimens were made and tested in the shearing test. The joints were prepared for the three combinations of the DC01 steel and EN AW-5754 aluminium alloy sheets with the thickness of 2mm. On the basis of the obtained load-elongation diagram tensile shear test curves, the basic parameters defined in the ISO/DIS 12996 standard were determined. In the case of the conventional riveted joints the maximum load capacity of the joint is determined by the strength of the fastener. For the joints with aluminium-steel blind rivet , the load capacity of the joint was on the strength limit of the rivet tubular part and on the strength limit of the sheet material. The strength of the SSPR joint is determined by the mechanical properties of the material of the joined sheets. From all sheets and rivet specimens arrangements the highest load capacity of the joint was obtained for the DC01 sheet material joints, and the lowest load capacity of the joint was obtained for the EN AW-5754 sheet material joints.

Jakub Cieśluk, Zdzisław Gosiewski, Leszek Ambroziak, Sławomir Romaniuk
Computationaly Simple Obstacle Avoidance Control Law for Small Unmanned Aerial Vehicles

The investigations of the system which allow to avoid obstacles by the unmanned aerial vehicles (UAV) are presented in the paper. The system is designed to enable the full autonomous UAV flight in an unknown environment. As an information source about obstacles digital camera was used. Developed algorithm uses the existing relations between the imaging system and the parameters read from the UAV autopilot. Synthesis of the proposed obstacle avoidance control law was oriented for computational simplicity. Presented algorithm was checked during simulation studies and in-flight tests.